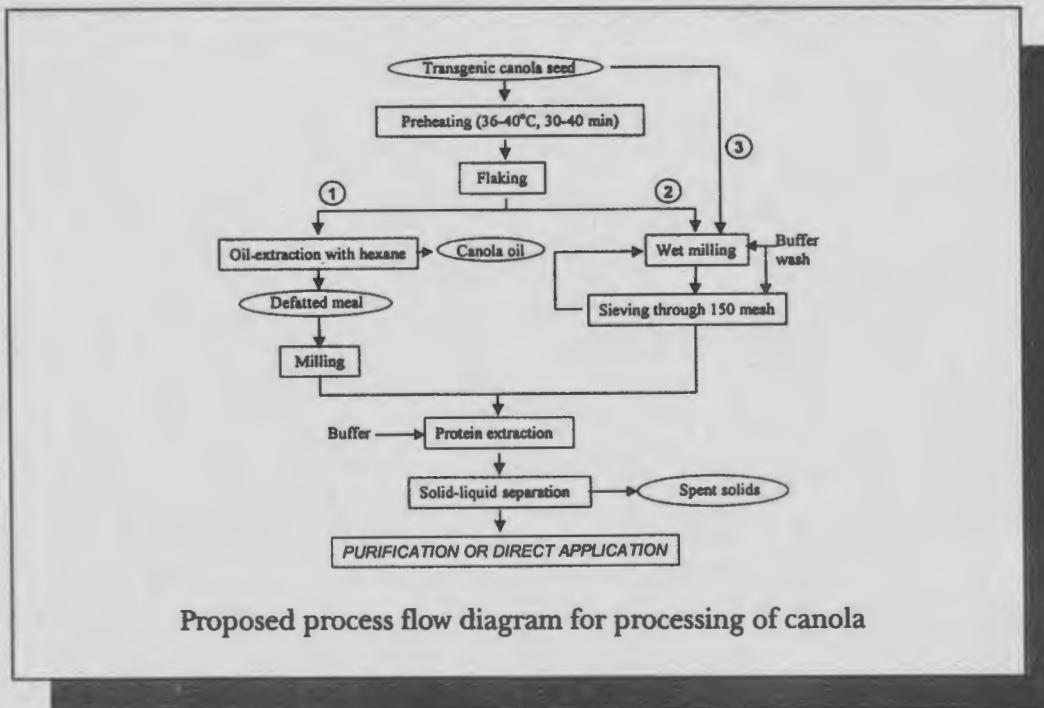


Annual Biochemical Engineering Symposium

October 2, 1999, Norman, Oklahoma



Roger G. Harrison
Editor

University of Oklahoma

School of Chemical Engineering and Materials Science

**Proceedings of the
Twenty-Ninth Annual
Biochemical Engineering Symposium**

October 2, 1999

**University of Oklahoma
Norman, Oklahoma**

**Roger G. Harrison
Editor**

LIBRARY

SEP 19 2000

**Iowa State University
of Science & Technology**

Preface

The 29th Annual Biochemical Engineering Symposium was held at the University of Oklahoma on October 2, 1999. The objectives of the symposium were to provide (1) an opportunity for students to present and publish their work, and (2) a forum for informal discussion of bioengineering research being carried out at the participating universities.

Sixteen papers presented at the symposium are included in these proceedings. Because final publication usually takes place in refereed journals, the articles here are typically brief and often cover work in progress.

Those who attended the symposium are the following:

University of Colorado: Paul Todd, Danielle Biggs, Shramik Sengupta

Colorado State University Rajiv Bhadra, Laurent Simon

Iowa State University: Peter Reilly, Jacqueline Shanks, Yun Bai, Zhiliang Fan, Ping-Hua Feng, Alain Laederach, Todd Menkhaus, Cheryl Miller, Mark Mowry, Chandrika Mulakala, Yutaka Okamoto, Xiaojing Pan, Bill Rockey, Ian Schneider, Ganesh Siriam, Murali Subramanian, David Wendt, Dongmei Zhai

Kansas State University: Larry Erickson, Sigifredo Castro Diaz, R. Karthikeyan, Jina Yang

University of Oklahoma: Roger Harrison, Sebastien Gauthier, Kent Leach, Laura Worthen

Oklahoma State University: Aditya Tyagi, Sridkar Venkataraman

Rice University: Erik Hughes

Financial support for this symposium from the College of Engineering and the School of Chemical Engineering and Materials Science at the University of Oklahoma is gratefully acknowledged.

Roger G. Harrison
Editor

Contents

Oral Presentations

Page Number	Time	
1	9:05	Control of Dissolved Oxygen in Fed-Batch Bioreactors Using Adaptive Generalized Predictive Control. Laurent Simon and M. Nazmul Karim (Colorado State University).
6	9:30	Phytoremediation of Corrosion Inhibitors in Aircraft Deicer Formulations. Sigifredo Castro Diaz, Lawrence C. Davis, Douglas Lupher, and Larry E. Erickson (Kansas State University).
16	9:55	Biodegradation of Jet Fuels (JP-8) in the Presence of Vegetation. R. Karthikeyan, L.C. Davis, K.R. Mankin, L.E. Erickson, and P. Kulakow (Kansas State University).
26	10:30	Bioprocessing Effect on the Stability of Recombinant β -Glucuronidase (rGUS) and its Extractability from Transgenic Canola, Yun Bai (Iowa State University) and Zivko L. Nikolov (Iowa State University and ProdiGene, Inc., College Station, TX).
34	11:00	Multistage Electrophoresis. Shramik Sengupta, Paul Todd, and K. S. M. S. Raghavarao (University of Colorado); and John Vellinger (SHOT Inc., Floyd Knob, Indiana).
40	2:15	Micropatterned Biodegradable Polymer Films for Peripheral Nerve Regeneration. Cheryl Miller, Surya K. Mallapragada and Carole A. Heath (Iowa State University).
44	2:40	Effects of Fluid-Induced Shear Stress and Simulated Aspects of Microgravity on Articular Cartilage Regeneration. David Wendt and Carole Heath (Iowa State University).
51	3:05	Thrombolysis in a Rabbit Stroke Model Using Liposomal-Encapsulated Streptokinase. Kent Leach and Edgar O'Rear (University of Oklahoma); Yiwei Miao and Art Johnson (Texas A&M University); Eugene Patterson (University of Oklahoma Health Sciences Center).
56	3:30	Shear Stress Modulates Platelet Aggregation at a Site of Vascular Injury. Elizabeth Nguyen, Laura Worthen, and Matthias U. Nollert (University of Oklahoma).

Poster Presentations

(1:00-2:15)

Page Number

- Effect of Poly (λ -Lactide) Microparticle Crystallinity on Alveolar Macrophage Inflammatory Response. D.L. Biggs and T.W. Randolph (University of Colorado); C.S. Lengsfeld (University of Denver); L.K. Ng and M.C. Manning (UC Health Sciences Center).
- 64 Characterization of Kinetics and Thermostability of *Acremonium strictum* Glucooligosaccharide Oxidase. Zhiliang Fan, Gbemeloluwa B. Oguntimein, and Peter J. Reilly (Iowa State University).
- 72 Automated Docking of α -(1 \rightarrow 4)- and α -(1 \rightarrow 6)-Linked Glucosyl Trisaccharides and Maltopentaose into the Soybean β -Amylase Active Site. William M. Rockey, Alain Laederach, and Peter J. Reilly (Iowa State University).
- 82 High-performance Anion-exchange Chromatography of Sugar and Glycerol Phosphates on Quaternary Ammonium Resins. Ian C. Schneider, Preston, J. Rhamy, Ruth J. Fink-Winter, and Peter J. Reilly (Iowa State University).
- 91 Effects of Salts on Subtilisin Crystallization. Xiaojing Pan and Charles E. Glatz (Iowa State University).
- 99 A Microcosm Study on Biodegradation of Methyl tert-butyl Ether (MTBE). Qizhi Zhang, Lawrence C. Davis, and Larry E. Erickson (Kansas State University).
- Toxic Effects of TCE on Soybean Seedlings. Jina Yang and Lawrence Davis (Kansas State University).
- 108 Transport of Organic Chemicals through Living Plant Tissues. L. C. Davis, D. Luper, Q. Zhang, J. Hu, and L. E. Erickson (Kansas State University).
- 114 Intracellular Calcium Response of Endothelial Cells Exposed to Flow in the Presence of Thrombin or Histamine. Laura M. Worthen and Matthias U. Nollert (University of Oklahoma).

Control of dissolved oxygen in fed-batch bioreactors using adaptive generalized predictive control

Laurent Simon and M. Nazmul Karim
Department of Chemical and Bioresource Engineering
Colorado State University
Fort Collins CO 80523

ABSTRACT

In order to maintain an optimum dissolved oxygen concentration (DO) in animal cell culture, it is necessary to develop enhanced control algorithms. In bacterial cell cultivations, the stirring rate or inlet gas flow rate is manipulated in order to improve the volumetric mass transfer coefficient ($k_L a$) of oxygen in the culture medium. This method usually gives satisfactory results since the mass transfer coefficient (k_L) is a function of agitation speed of the impeller. The gas-liquid interfacial area (a) varies with the gas flow rate. These methods however are not suitable for mammalian cells because of the delicate plasma membrane which provides inadequate protection against shear. In designing DO controllers for animal cell cultures, the partial pressure of oxygen is usually the manipulated variable while total gas flow rate and stirring rate are kept constant. These controllers perform relatively well since around atmospheric pressure, the solubility is proportional to the partial pressure of the gas. However, alteration in medium composition during bioreaction affects gas solubility and volumetric mass transfer coefficient. These changes are due to conversions of carbon and nitrogen sources into biomass and addition of acid, base, and feed in the bioreactor. The performance of DO controllers may deteriorate over time and may result in poor performance of bioprocesses.

An adaptive generalized predictive controller (GPC) was designed and simulated for fed-batch and batch fermentation processes. The extended least-squares algorithm was used for model identification. The controller parameters were calculated at each sample interval based on the updated plant model. The mass transfer coefficients for headspace aeration and bubble gas phase used in the simulation were obtained from experiments in serum free media at 37°C. The GPC was able to reject bias disturbance and track changes in DO reference concentrations. However, the performance of the controller depended largely on the tuning parameters, and these were varied adaptively in this control algorithm.

INTRODUCTION

It is important to develop control algorithm to facilitate adequate oxygen transfer in animal cell cultures. Oxygen is necessary for energy production and formation of cellular constituents such as tyrosine and cholesterol (Blanch and Clarck, 1996). The approach used for bacterial cells is to manipulate the agitation speed or the gas supply rate in order to optimize the volumetric mass transfer coefficient $k_L a$. These methods give satisfactory results since the mass transfer coefficient k_L is a function of the power

dissipation by impeller per unit volume (Lopes De Figueiredo and Calderbank, 1979). The gas liquid interfacial area a also varies with the gas flow rate (Miller, 1974). Since animal cells are more shear sensitive than bacterial cells, dissolved oxygen concentration is controlled by changing oxygen solubility, and keeping gas supply and stirring rate constant in the bioreactor (Oeggerli *et al.*, 1995.). This method has the advantage of minimizing cell damage since bursting bubbles are greatly reduced at the liquid surface. Adaptive methods have been used to improve DO control. However, they have been applied to batch cultivations (Heinzle *et al.*, 1990; Lee *et al.*, 1991; Oeggerli *et al.*, 1995; Sargantanis and Karim, 1999). Since in fed-batch fermentations, the viscosity of the medium and the salt concentrations are constantly varying, control algorithm needs to be adaptive to account for changes in k_La values.

MATERIALS AND METHODS

Apparatus

The experimental setup is shown in Figure 1 and consists of a 3-L (1.75 liquid volume). The temperature is controlled at 37 °C using a heating tape and a temperature controller (OMEGA, Stamford, CT). The dissolved oxygen readings are reported as percent saturation. One hundred percent saturation (DO = 100) is equivalent to the saturation of dissolved oxygen concentration with air at 37 °C in a low protein serum free medium. A stream of air set at 100 cc/min enters the top of the bioreactor. During experimental runs, the gas flow rate entering though the sparger is set at 191 cc/min. The DO voltage signals are sent to a data acquisition card (NATIONAL INSTRUMENT CORP., Austin, TX) and read by the computer. An internal algorithm written in CMEX S-function (MATHWORKS, Natick, MA) uses the information from the DO probe and sends appropriate control signals via a computer card (ADVANTECH, Sunnyvale, CA) to two mass flow controllers (COLE-PARMER, Vernon Hills, IL).

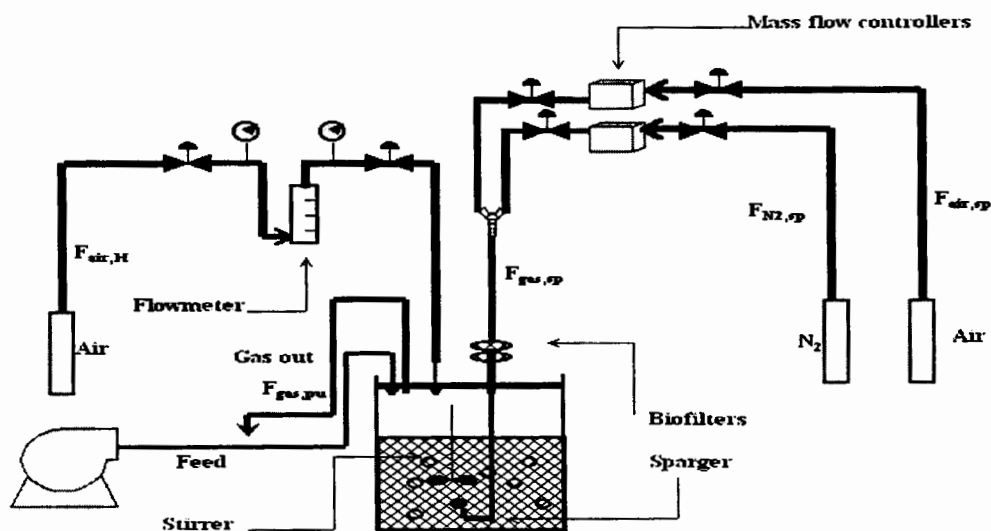


Figure 1. Experimental setup

Parameter estimation

Using a low protein serum free medium, the overall mass transfer coefficients were calculated for the head space (k_{LaH}) and the bubble gas phase (k_{LaB}). k_{LaB} is obtained by taking the slope of the time derivatives of DO versus DO with no air entering the top of the bioreactor ($F_{air,H}$). ($k_{LaH} + k_{LaB}$) is calculated in a similar way while keeping $F_{air,H}$ at 100 cc/min. The respective values of k_{LaB} and k_{LaH} are $7.49e-04$ (s^{-1}) and $5.57e-05$ (s^{-1}).

Generalized predictive controller

Generalized predictive control is based on a model of a process to evaluate how control strategies will impact the future behavior of the process. The control strategy of the MPC is to calculate a sequence of control signals [$\Delta u(k)$, $\Delta u(k+1)$, ..., $\Delta u(k+Nu-1)$] that will force the predicted outputs [$y(k+N_1|k)$, $y(k+N_1+1|k)$, ..., $y(k+N_2|k)$] to some desired reference vector [$r(k+N_1)$, $r(k+N_1+1)$, ..., $r(k+N_2)$] (Proll and Karim, 1994). The length of the predicted control sequence from 0 to Nu , determine the control horizon. N_1 to N_2 represents the output costing horizon or prediction horizon. Only the first move is implemented, and a new sequence of control inputs is calculated at the next sampling instance. It's customary to include a forgetting factor λ in building the model and a penalty γ on the control signals $\Delta u(k)$.

RESULTS

After solving the oxygen balances in the liquid phase and the head space, the open-loop system is simulated using Simulink (MATHEMATICS, Natick, MA). A specific oxygen uptake rate (OUR) is added as a noise to the system to account for the growth of cells in a real time process. The liquid volume (V) is allowed to change from 1.7 to 2.2 L. After implementing step changes in the composition of oxygen in the sparger ($y_{O_2,B}$), the dissolved oxygen concentration changes in the same direction as expected (results not shown). The simulation lasts about 25 min and samples are collected every second. As previously outlined, the flow rate through the sparger is kept constant.

Two simulations are run for the closed loop system. In the first simulation, the parameters of the GPC are $N_1=1$, $N_2=2$, $Nu=2$, $\gamma=0.995$, $\lambda=0.995$. The simulation and sampling times are 1 s and $\frac{1}{2}$ h. For a set point of 40% DO the system settles in 25 min, after an overshoot of 13 % and a rise time of 15 min. To test the effect of the prediction horizon on the performance of the controller, a second simulation is run. N_2 was set at 4 while all other tuning parameters remain constant. In this case the system exhibits approximately the same rise time. However, the overshoot is reduced to 3 % and the settling time is about 17 min. The improved controller is tested for step changes in the setpoint (40, 10 and 50%). The controller is able to track these changes satisfactorily (results not shown).

The controller used in simulation 1 is tested in real time using the low protein serum free medium and the conditions outlined in MATERIALS AND METHODS section. Water is added to the bioreactor and antifoam is used to reduce foaming. The agitator is set at 90 RPM. The results are shown in Fig. 2. The top graph represents the

dissolved oxygen response for a 1-h run. The flow rate of the nitrogen stream is shown in the bottom graph. The flow rate of the air stream is 191 cc/min minus the flow rate of the nitrogen stream. One can easily obtain the molar fraction of oxygen in the sparger.

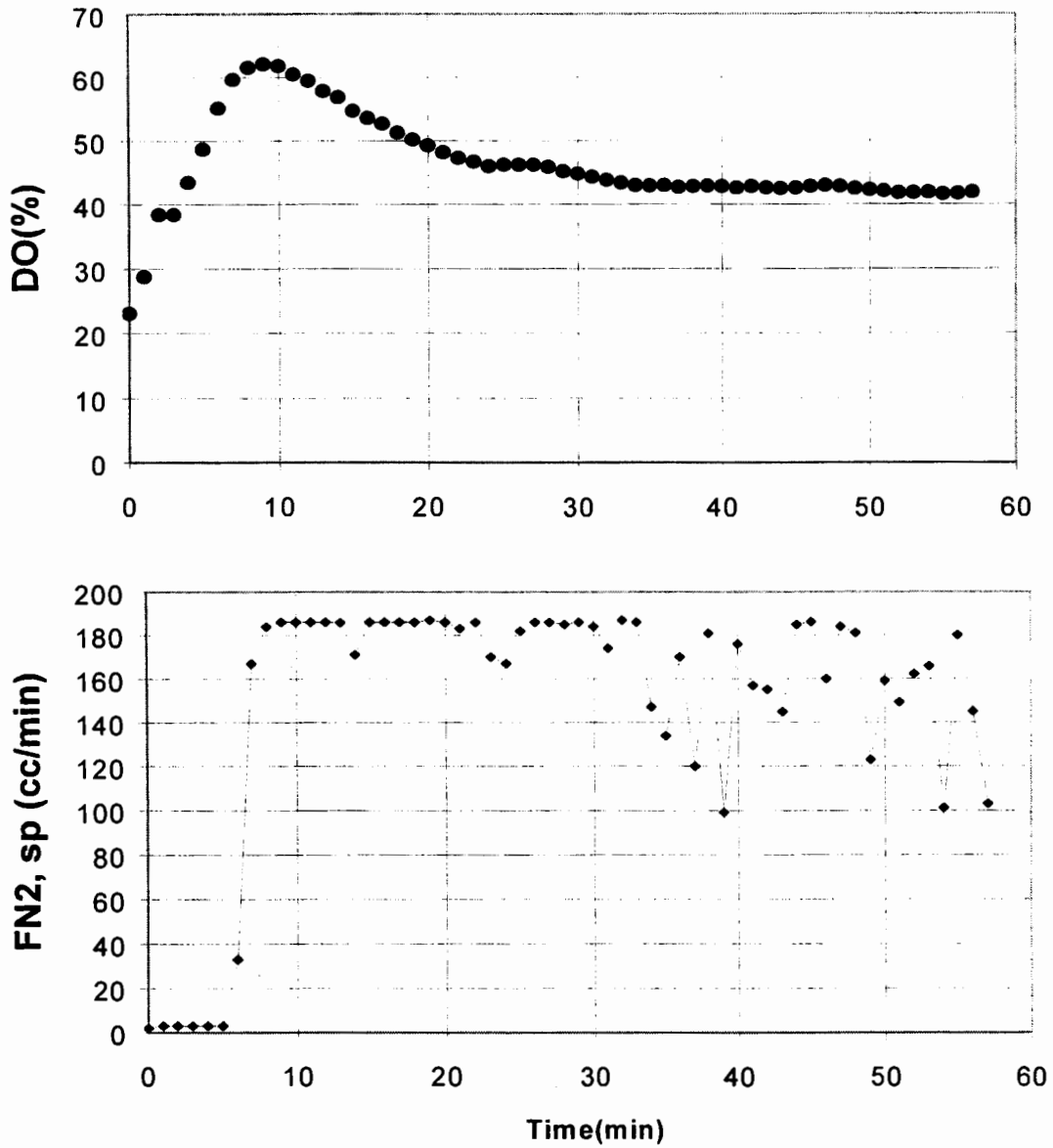


Figure 2. Experimental closed-loop results

CONCLUSIONS

An adaptive control algorithm based on recursive least-squares 5-parameter model was implemented to control dissolved oxygen concentration in a constant shear environment. The performance of the controller depends on the maximum prediction horizon N_2 . System overshoot was greatly decreased when N_2 varied from 2 to 4. When the less robust GPC ($N_2 = 2$) was tested in real-time, the DO response showed a 50% overshoot during the first ten minutes and a small offset after about an hour.

ACKNOWLEDGMENTS

The authors are grateful for the financial support from the National Science Foundation, UNCF.MERCK graduate science research dissertation fellowship, and the Colorado State University Experimental Station.

REFERENCES

- Blanch H.W. and D.S. Clarck (1996). Biochemical Engineering. Marcel Dekker, Inc., New York, NY.
- Heinzle E., A. Oeggerli and B. Dettwiler (1990). On-line fermentation gas analysis: error analysis and application of mass spectrometry. *Anal. Chim. Acta*, **238**, 101-115.
- Lee S.C., Y.B. Hwang, H.N. Chang and Y.K. Chang (1991). Adaptive control of dissolved oxygen concentration in a bioreactor. *Biotechnol. Bioeng.* **37**, 597-607.
- Lopes De Figueiredo, M.M. and P.H. Calderbank (1979). The scale-up of aerated mixing vessels for specified oxygen dissolution rates. *Chem. Eng. Sci.* **34**, 1333-1338.
- Miller, D.N. (1974). Scale-up of agitated vessels gas-liquid mass transfer. *AIChE J.*, **20**, 442-453.
- Oeggerli, A., K. Eyer and E. Heinzle (1995). On-line gas analysis in animal cell cultivation: I. Control of dissolved oxygen and pH. *Biotechnol. Bioeng.*, **45**, 42-53.
- Proll T. and M.N. Karim (1994). Model-predictive pH control using real-time NARX approach. *AIChE J.* **40**, 269-282.
- Sargantanis I.G. and M.N. Karim (1999). Variable structure NARX models: application to dissolved-oxygen bioprocess. *AIChE J.*, **45**, 2034-2045.

PHYTOREMEDIATION OF CORROSION INHIBITORS IN AIRCRAFT DEICER FORMULATIONS

SIGIFREDO CASTRO ⁽¹⁾, LAWRENCE C. DAVIS ⁽²⁾, DOUGLAS LUPHER ⁽¹⁾,
and LARRY E. ERICKSON ⁽¹⁾. KANSAS STATE UNIVERSITY

⁽¹⁾ Department of Chemical Engineering, KSU, Manhattan, KS 66506, Phone: 785-532-5584, Fax: 785-532-7372. ⁽²⁾ Department of Biochemistry, KSU, Manhattan, KS 66506, Phone: 785-532-6121, Fax: 785-535-7278.

Abstract – The benzotriazole methyl substitution isomers (tolyltriazole), which are produced in large quantities and used as corrosion inhibitors in antifreeze and aircraft deicer formulations, constitute a terrestrial and aquatic environmental risk. Although benzotriazoles are identified as possible carcinogens and inducers of toxic responses in model ecosystem receptors (fish, invertebrates, marine, and soil bacteria) even at low concentrations, there is not complete information to determine their breakdown products, (bio)degradation potential, and mode of toxicity. It is known that lignin peroxidase is an enzyme able to degrade the tolyltriazole. This enzyme is expressed by white-rot fungus, *Phanerochaete chrysosporium*, and it is also the catalyst in the lignification process in higher plants. Since the cultural conditions for the fungus are fairly specific, a plant based remediation process would be more desirable to economically detoxify Aircraft Deicer Fluid (ADF). The threshold for toxicity and general effects of benzotriazoles to common grass used at airports and on wild sunflower plants were investigated. Different methods to extract the benzotriazoles from the treated plants were explored and possible phenolic biodegradation products were analyzed as well. We will discuss a still unproved mechanism of bioremediation, which includes the incorporation of the benzotriazoles into sunflower lignin and the production of phenolic products.

INTRODUCTION

Aircraft deicing fluid (ADF) is an aqueous glycol-based mixture that is routinely used at many U.S. airports to control ice formation on aircraft before takeoff. During deicing operations, a significant portion of excess ADF runs off the aircraft where it may enter storm drains and nearby surface water and cause severe environmental damage (Bausmith et al., 1999). The discharge of untreated aircraft deicing fluid (ADF) wastes to surface water and storm water collection systems is of concern and many airports are searching for alternative methods for managing ADF wastes.

Some Waste Management Alternatives might be:

1. Discharging ADF waste to a publicly owned treatment works. Several problems have been reported and municipalities are often reluctant to accept untreated ADF waste.
2. On-site treatment system and/or recycling. These options are costly and generally only applicable to largest airports. However, there is always a certain amount of runoff and seepage to groundwater.
3. On-site land treatment. Most favorable approach because most airports embrace a significant area of land.

Studies demonstrated that land treatment of propylene glycol-based ADF under controlled conditions is an effective means of remediation for ADF solutions in soils for concentrations up to 20% by weight of propylene glycol (Bausmith et al., 1999). However, the toxicity of benzotriazoles may inhibit the bacterial decomposition of glycols. Although the solutions can be diluted to prevent this inhibition, the benzotriazoles might bypass the biodegradative stage and seep into the saturated groundwater systems.

In general, it can be said that the antifreeze and deicing solution mixtures are more toxic than the individual components. There might be different ADF formulations and the exact information about their composition is proprietary. In general, when diluted for use, the formulation may be approximately as shown in Table 1.

Component	wt%
Propylene Glycol	20 – 30
Tolyltriazole	0.1 – 1
Surfactants	1 – 4
Other Additives	1 – 5
Water	60 – 70

As a way to address the problem, we are investigating alternatives to handle the more toxic components present in the formulation individually as well as the complete formulation, focusing on the corrosion inhibitors (tolyltriazoles).

Tolyltriazoles

The chemical structure of 1-H-benzotriazole is shown in Figure 1. Methyl groups on the benzene ring yield the 4-methyl-1H-benzotriazole and 5-methyl-1H-benzotriazole (USEPA, 1977).

Aircraft deicer fluids contain a mixture of 4-methyl-1H-benzotriazole and 5-methyl-1H-benzotriazole, often referred as "tolyltriazole", which contains approximately equal amounts of the two isomers. Some of their physical properties are described in Table 2 (USEPA, 1977).

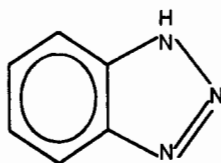


Figure 1: Chemical Structure of 1-H-benzotriazole

Characteristic	Benzotriazole	Tolyltriazole
Molecular weight	119.12	133.16
Specific gravity (25°C)	1.33	1.16
Melting point (°C)	98 – 99	96 – 100
Vapor pressure (atm)	5 E-05 (20°C)	4 E-05 (50°C)
Boiling Point (at 1 atm, °C)	350	160
Solubility in water	20 g / L (20°C)	
	200 g / L (90°C)	
Stability to UV	High	High

Benzotriazole and its derivatives are white to light yellow crystalline powders. They are stable to temperature and electromagnetic radiation, dissipating absorbed ultraviolet energy as heat. The spectra are characterized by broad absorbance below 400 nm, with a maximum around 275 nm.

The low vapor pressure of triazoles ensures little of these contaminants in the atmosphere; however, because of their appreciable water solubility, it may be expected that they will migrate through the soil and eventually make their way to ground water. A retardation factor of about 2 in soil with an organic matter content of 1% indicates that triazole is sorbed to soil (our unpublished observations). Their stability is the key concept in benzotriazole chemistry. In the proper condition it can undergo a variety of reactions (halogenation, oxidation, hydroxylation, condensation, etc.) but the integrity of the triazole ring is almost never compromised. These compounds react readily to form stable metal complexes, which are capable of protecting the metal (particularly copper) from further chemical attack. They absorb over a broad range in the ultraviolet region. Therefore they are capable of protecting less stable molecules from degradation on exposure to ultraviolet radiation. It is, then, the combination of chemical versatility, which allows modifying solubility, adsorption spectra, compatibility with plastics, etc., of benzotriazoles on the one hand, and the relative physical and

chemical stability of the benzotriazoles on the other, which chiefly characterize benzotriazole and its derivatives in their major applications. At the same time, their chemical structure and physical properties make these compounds stable and persistent substances under environment conditions. They do not oxidize or hydrolyze; they are not reactive under sunlight irradiation and there is not evidence of biodegradation of benzotriazoles by bacteria (Rollinson et al 1998). Benzotriazoles have not been extensively studied for biological activity. However, their structural similarity to naturally occurring substances (adenine, guanine, indole) suggests that they could inhibit the production of proteins, enzymes, and RNA in mammalian systems and affect the central nervous and endocrine systems as well (USEPA, 1977). Although the evidence is not strong, they have been identified as possible carcinogenic substances (NCI, 1978). They have been shown to induce toxic responses in model ecosystem receptors including fish, invertebrates, and marine and soil bacteria at relatively low concentrations (Hartwell et al 1995, Pillard 1996, Cancilla et al 1997). Little is known about the mode of toxicity of benzotriazoles in plants. They have some similarity to natural plant growth regulators. Damage to the root system seems to be the main effect. We have observed growth inhibition on pumpkin, horseradish, sunflower, and fescue at concentrations below 0.1 mg/mL.

Total production of benzotriazoles was estimated to be 56 million pounds per year in the United States (USEPA, 1977) with the majority going into anticorrosion applications. Typical applications include the protection of copper-containing parts by inclusion of benzotriazoles in automobile antifreeze solutions, in the formulation of aircraft deicer solutions, in recirculating water systems such as power plant and commercial air conditioning systems, and in coatings for the protection of copper alloys in architectural and decorative applications. Their use has markedly increased since 1977 as aircraft deicers have increased in use and more vehicles are on the road. They also are an important component to protect plastics from UV decomposition (plastic stabilizers). They can be used as photographic antifoggants and organic synthesis reagents. Recently the 1-hydroxy derivative is being considered as an alternative laccase mediator in biopulping for paper production, a process from which large amounts of a by-product, benzotriazole, might be discharged to the environment (Call et al 1997).

Phytoremediation of Tolyltriazole

We have investigated the fate of benzotriazoles in plant-based remediation for use in situ at airports. It is desirable to minimize the need for off-site processing. We have reported that triazole degradation may be achieved by the metabolic action of the enzyme lignin peroxidase. This enzyme can be naturally obtained from two sources: White rot fungus and higher plants. *Phanerochaete chrysosporium* is a filamentous, white, wood-rotting fungus, characterized by fast growth and easy reproductive cycles. It possesses the ability to degrade lignin, a complex natural polymer composed of phenyl-propane units that is resistant to decay by many microorganisms. The lignin-degrading

ability has been attributed to a complex mixture of enzymes secreted by the fungus to the extra cellular medium; the enzymes are peroxidases that utilize hydrogen peroxide from complementary enzyme systems to perform an initial oxidative conversion of lignin. Some of the more common substructures of lignin resemble the chemical structure of many persistent organic compounds (like the benzotriazoles), giving sufficient reasons to pursue the application of the fungus to the biodegradation of benzotriazoles. However, the fungus culture conditions are fairly specific. The fungus is very sensitive to factors such as absence of required nutrients, high pH conditions, excess of nitrate compounds, low temperatures, competing microorganisms, etc. (Aust et al, 1997). These characteristics make it difficult to develop a feasible on-site treatment with the fungus. On the other hand, higher plants strengthen their cell walls by lignification, which is the polymerization of methoxylated aromatic alcohols with laccase and lignin peroxidases as the catalysts (Ruhland et al, 1958). The similarity of triazoles with some substructures of lignin suggests that they may be incorporated into lignin (this in part explains the growth inhibition in plants).

MATERIALS AND METHODS

For tolyltriazoles, absorption of ultraviolet radiation (275 nm) allows detection and monitoring by using spectrophotometry. In our study, it was employed in Altex Gradient Liquid Chromatograph in conjunction with a Hamilton PRP-1 Column. A solution of methanol and water (40-60%) at a flow rate of 1.0 ml/min was the optimal condition to obtain a good peak resolution. Varying the methanol/water ratio in the mobile phase optimized the resolution of the peak and separation from other interfering substances. Phenolic exudates from plants have a short residence time and pronounced absorbance at 275 nm. Figure 2 shows the results of varying the methanol/water ratio; a) represents the methyl benzotriazole peak; b) and c) the solution with phenolic exudates at different methanol/water ratios.

The monitoring of propylene glycol was done indirectly measuring the depletion of sodium periodate by the oxidation reaction (Nordin, 1982). Periodate consumption was monitored by absorbance decrease at 260 nm. The adaptation for the flow injection analysis work included the reaction at 65°C and acid conditions to improve the sensitivity. The mobile phase for the assay was a solution of periodate ion 0.1 mM (from sodium p-periodate), in sodium hydroxide (0.05 M), boric acid (0.1 M), and acetic acid (10 ml/L). The pH range was between 4 and 5 and the absorbance was about 0.86.

The samples containing propylene glycol were injected and mixed with the mobile phase using a HPLC pump and loop injector. Reaction was on a high-density polyethylene tubing for 4 minutes at 65°C. Solutions of propylene glycol at concentrations of 2, 4, 6, and 8 mM were used as standards. The system allowed us to detect solutions below 1 mM (~0.1 mg/ml) very rapidly even for a large number of samples.

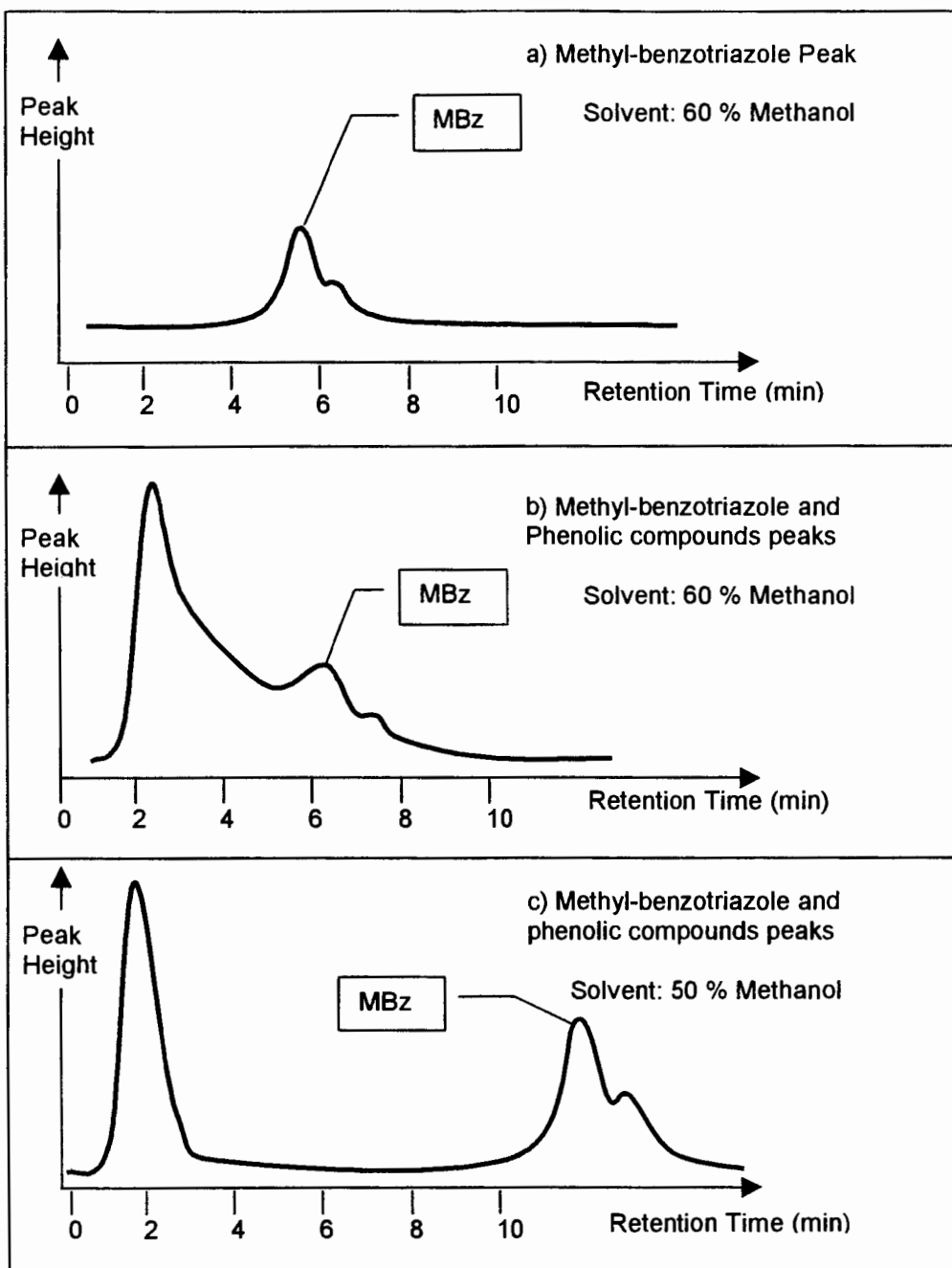


Figure 3: Effect of varying the methanol/water ratio in the mobile phase for improving the resolution of methyl-benzotriazole. Phenolic compounds are present in b) and c).

Plants selected for the preliminary studies were fescue grass and sunflowers. The grass, K-31 cultivar, is a very common grass used at airports and represents a perennial monocot with an extensive fibrous root system. The sunflowers are rapidly growing dicots that produce woody stems in a short season.

Grass was planted in vermiculite, and in a mixture of topsoil / vermiculite (volumetric ratio 1:2). Growing sunflowers were studied in aqueous solution and from seeds in topsoil / vermiculite mixture. In all cases the medium was enriched with Hoagland's solution ¼ strength, and the solutions of triazole, propylene glycol and ADF were prepared in that solution as well.

OBSERVATIONS

Fescue grass seedlings treated with methyl-benzotriazole and benzotriazole solutions at a concentration 0.05 mg/ml grew nearly normally while plants treated at 0.1 mg/ml were stunted. After 20 and 40 doses of 25 ml in mature fescue grass the biomass production (as percentage in weight of leaves produced with respect to a healthy untreated control) and the accumulation of triazole in the plant (measured as the loss of the compound with respect to the material introduced) were recorded. The results are shown in Table 3.

Compound	Concentration fed (mg/ml)	% Biomass produced relative to control		Triazole incorporated in plant (mg)
		After 20 doses	After 40 doses	
Methyl-Benzotriazole	0.05	35.8	17.3	23.65
	0.1	44.3	5.1	17.6
	0.15	43.8	1.45	3.21
Benzotriazole	0.05	46.2	26.4	39.15
	0.1	31.3	3.6	33.88
	0.15	27.7	0.6	33.51

The study revealed that a concentration greater than 0.05 mg/ml of either methyl-benzotriazole or benzotriazole was toxic, and it was lethal at a concentration of 0.15 mg/ml. For concentrations below 0.05 mg/ml the plants grow somewhat less vigorously. The accumulation of benzotriazole within the plant is greater for benzotriazole. This result is in accordance with the presence of the methyl- group in the methyl-benzotriazole, which might reduce its mobility throughout the plant. It is also shown that the benzotriazole is somehow less toxic than its derivative, because similar effects were observed but the accumulation was higher.

Several extraction methods were investigated for the recovery of the triazoles from the plants. Solvents such as water, methanol, ethanol, and acetone in different sequences, residence times, and temperatures (as high as 96°C) were unsuccessfully tried. Even with 1 M NaOH or 1 M HCl solutions at low and high temperatures there was no recovery. This leads us to think that the triazoles are being bonded and/or transformed within the plants resulting in a

non-extractable form of the compound, maybe as part of the plant structure. The effect of the ADF solution mixture on fescue grass is being studied.

In a 1 month treatment, sunflower seeds were able to grow in the soil / vermiculite mixture almost normally (as high as the controls) when watered with methyl benzotriazole solution at 0.025 mg/ml. The leaves, however, turned yellow and brown and were less vigorous than the controls, with the effect more pronounced in the bottom leaves. The top leaves were nearly normal and the plants flowered about 5 days before the controls did. These effects were more evident at 0.05 mg/ml, which also flowered sooner. At a concentration of 0.1 mg/ml the plants were 20% less tall than the controls and produced small precocious flowers. The leaves and roots, however, showed much more damage. For several months wild sunflowers were held in an aqueous solution containing different concentrations of triazoles maintaining enough volume according to their consumption (more solution was added when the level was noticeably reduced). In general, the rate of water consumption per gram of initial fresh plant material decreased with time. This effect was larger when the triazole concentration was greater than 0.1 mg/ml. It was possible to observe the gradual damage of the roots, which first turned brown, followed by size reduction. It is remarkable that the plants accumulated enormous amounts of triazole and transformation products within their structure (up to about 3.0 to 5.0 mg of triazole incorporated per gram of fresh initial plant material for a period of about 35 days). The accounting was done by measuring the concentration of the solution in the container at different times and comparing this with the amount expected in this solution based on the amount added. Similar extraction methods as those done for the fescue grass were also unsuccessfully tried, even at these high levels of accumulation.

A preliminary observation shows phenolic compound formation in the aqueous solution for plants treated with triazole as compared with no formation for untreated plants. This might be seen as a possible intermediate product in the decomposition pathway of the triazole by the root system.

Sunflowers at about 10 days age grown from seeds in soil/vermiculite mixture were treated with ADF solutions at concentrations of 1.0, 2.0, and 4.0 % of ADF, watering from the top a dose of about 50 ml depending on the excess of runoff observed. After only 10 days the leaves started to show severe damage in their periphery, an effect that occurred at the medium-top leaves. After 20 days of treatment, the effect "moved inward" destroying the medium and bottom leaves. The same phenomenon was observed for solutions of propylene glycol (PG) by itself at the same concentrations. The effect was drastic for the highest concentration, as shown in Table 4.

Analysis of the accumulation of the PG on the stems and leaves, shows that this effect might be attributed to the glycol present in the ADF formulation, which accumulates in the leaves and alters the osmotic equilibrium of the leaf.

On a dried weight basis, the plant material accumulated about 120 mg of PG per gram of dried plant material at the highest-level treatment (2% of Deicer), for a period of 30 days.

% (V/V) PG in input solution	Analyzed concentration (mM)			% of reduction in plant height
	Soil	Stems	Leaves	
0.22	0	18.3	16.26	15
0.44	1.5	3.1	16.18	50
0.88	3.81	8.65	25.52	60

By visual comparison of the ADF solution with the PG by itself after 30 days of treatment, the plants treated with ADF showed a more severe effect than the PG ones. This might be attributed either to the toxicity of triazoles to the bacteria degrading the propylene glycol, or to the presence of surfactants in the formulation that can have toxic effects for the plants as well, or a combination of both toxicities.

CONCLUDING REMARKS

From the described study, we propose that benzotriazoles are transformed by lignin peroxidases and laccase of plants to incorporate them into the lignin fraction, immobilizing the triazole. When added at a level beyond the ability of the plants to cope, the benzotriazoles result in root death and eventually plant death. Copper and borate requirements are under investigation in the search for the mechanism of toxicity of triazoles to plants. In situ soil biodegradation of propylene glycol is possible under controlled conditions. However, the toxic effect of the propylene glycol to plants (mainly the alteration of the leaves osmotic equilibrium) inhibits the triazole immobilization by plants. At the same time, the bacteria degrading the glycol might be inhibited by the presence of triazoles. It is still necessary to find the appropriate conditions, i.e., concentration of contaminants, extra supplementation of certain nutrients, soil pre-adaptation, location of the input, and so on, for which the degradation of both contaminants can be achieved.

ACKNOWLEDGMENTS

This research was partially supported by the U.S. E.P.A. under assistance agreement R-819653 to the Great Plains-Rocky Mountain Hazardous Substance Research Center for regions 7 and 8 under project 94-27. It has not been submitted to the EPA for peer review and, therefore, may not necessarily reflect views of the agency and no official endorsement should be inferred. The Center for Hazardous Substance Research also provided partial funding.

REFERENCES

Aust, S. J. (1997). Factors affecting biodegradation by white rot fungi. In *Situ and On-site Bioremediation. Papers from the 4th International in situ and on-site bioremediation symposium.* B.C. Alleman and A. Lesson, Eds. **2** 481-487.

Bausmith D., Neufeld, R. (1999). Soil biodegradation of propylene glycol based aircraft deicing fluids. *Water Environment Research.* **71** (4): 459-464.

Call, H.P., I. Mucke (1997) History, overview, and applications of mediated ligninolytic systems, especially laccase-mediator systems (lignozyme process). *Journal of Biotechnology* **53**:163-202

Cancilla, D.A., A. Holtkamp, L. Matassa and X. Fang (1997). Isolation and characterization of MicrotoxTM active components from aircraft deicing/anti-icing fluids *Environ. Toxicol. Chem.* **16**:430-434.

Hartwell, S.I., D.M. Jordahl, J.E. Evans and E.B. May (1995). Toxicity of aircraft deicer and anti-icing solutions to aquatic organisms. *Environ. Toxicol. Chem.* **14**:1375-1386.

N.C.I. (1978) Bioassay of benzotriazole for possible carcinogenicity, National Cancer Institute, Bethesda, MD, DHEW Pub No. NIH 78-1338.

Nordin, P. (1982). Monitoring of carbohydrates with periodate in effluents from high-pressure liquid chromatography columns. *Analytical Biochem.* **131**, 492-498.

Pillard, D.A. (1995). Comparative toxicity of formulated glycol deicers and pure ethylene and propylene glycol to *Ceriodaphnia dubia* and *Pimephales promelas*. *Environ. Toxicol. Chem.* **14**:311-315.

Ruhland, W. (1958) Metabolism of secondary plant products. *Encyclopedia of Plant Physiology.* W. Ruhland, founding editor. Springer-Verlag, Berlin. **10**:389-411.

USEPA (1977) Investigation of selected potential environmental contaminants: benzotriazoles. EPA 560/2-77-001

Biodegradation of Jet Fuel (JP-8) in the Presence of Vegetation

R. Karthikeyan¹, Larry C. Davis², Kyle R. Mankin¹, Larry E. Erickson³, and P. Kulakow⁴
¹Biological and Agricultural Engineering, ²Biochemistry, ³Chemical Engineering, and
⁴Agronomy, Kansas State University, Manhattan, KS 66506

1. Introduction

Jet fuels are supplied for turbine engines in grade JP-4 (low vapor pressure) and grade JP-5 (high flashpoint). Less volatile jet fuels such as grade JP-7, JP-8, and JP-T (thermally stable), are supplied for special aircraft. During the 1990's, many units of the US Air Force have changed their usage of fuel from JP-4, in use since the 1950's, to JP-8. JP-4 is a wide-cut petroleum distillate exhibiting compounds from the lighter naphtha fraction as well as the kerosene fraction of petroleum. JP-8 typically range in composition from 6-carbon hydrocarbons to 18-carbon hydrocarbons (Mayfield, 1996).

The Air Force is now in the process of changing operations at its installations within the Continental US to use JP-8 in place of JP-4. This changeover has required the alteration of many environmental impact estimates. There are few studies conducted on fate and environmental effects of JP-4 and JP-8. Results of experiments conducted in aquatic systems indicate that evaporation was the major loss for low molecular weight hydrocarbons in JP-4 and JP-8 (Spain and Somerville, 1985; Dean-Ross et al., 1992). An experimental study on the fate of JP-8 in soil showed that higher molecular weight hydrocarbons were removed significantly faster in soils with indigenous microbial populations than in sterile soil (Dean-Ross et al., 1992). A similar study on fate of JP-4 in soil concluded that biodegradation contributed to the removal of the higher molecular weight fraction of JP-4 from soil (Dean-Ross, 1993). The above two studies suggest that for the less volatile hydrocarbons, manipulation of conditions to enhance biodegradation may increase their rate of removal from the terrestrial environment. Results of a study on the biodegradation of JP-4 in a contaminated aquifer indicate that biodegradation was compound specific (Aelion and Bradley, 1991).

Evaporation is undoubtedly a major fate of jet fuels in the terrestrial environment; however, biodegradation has the potential to lessen the environmental impact of less volatile hydrocarbons. By manipulating the soil physical, chemical, and biological conditions, biodegradation of jet fuels can be enhanced. This may increase their rate of removal from the terrestrial environment. A study was undertaken to assess the biodegradation of jet fuels (JP-8) in soils and the toxic effects of JP-8 on vegetation. This paper presents the results of the experimental study.

2. Experimental Section

Two vegetated systems were used to study the fate of JP-8 in the presence of vegetation: two-channel system and four-column system.

2.1. Two-channel System

For the experimental study, a large chamber with slate walls, used in a previous biodegradation experiment was chosen. The chamber was 40 cm wide, 90 cm long, and 35 cm deep. The chamber was divided along the axial length into two equal halves, each with a width of 20 cm. Each half was further divided by a 78 cm long wall into two halves, each with a width of 10 cm. Thus, the chamber consisted of two U-shaped channels with dimensions 10 cm in width, 35 cm in depth, and 180 cm in axial length with inlet and outlet holes at 5 cm from the bottom. The chamber construction and schematic details can be found elsewhere (Narayanan, 1992).

The channels were filled with sandy soil collected from near a landfill in Riley County, Kansas. In previous experiments, the soil had been contaminated with toluene, phenol, and TCE. After a long period of drying down to volatilize TCE, gas and soil TCE measurements were made. The gas and soil monitoring indicated that 99% of TCE had disappeared by December, 1998. Alfalfa plants (9 plants in each row) were grown in the two-channel system.

Channel 1 was irrigated from an inlet located at the bottom. A graduated reservoir with a capacity of 5 L was used to supply water from the bottom. The water level in the reservoir was raised to allow natural flow of water through a nylon tube. The nylon tube was firmly fitted into the inlet of the channel and occasional plugging at the inlet was rectified when observed. Leachate, if any, was collected from the outlet. Channel 2 was irrigated by a subsurface drip system distributed at 4 locations. Each drip consists of two 50 mL syringes connected with a Y tube and tubing to a glass tube inserted into the soil 20 cm. Two more 50 mL syringes were connected one each at inlet and outlet ports of channel 2 to avoid drying out of soil.

2.2. Four-column System

Four glass cylinders of 40 cm deep and 15 cm in diameter were used in the study. The cylinders were filled with sandy soil collected from a landfill in Riley County, Kansas. The cylinders were previously supplied with TNT and then watered with toluene, and most recently had been exposed to the soluble constituents of jet fuel for several months. A graduated reservoir with a capacity of 5 L was used to supply water from the bottom to columns 1 and 2; columns 3 and 4 were watered from top. Column 1 and 4 were kept unvegetated and column 2 and 3 were planted with four horseradish plants in each.

2.3. One-column System

A 250 mL glass measuring cylinder was used to conduct a separate study on the fate of JP-8 in air dried soil. A known amount of JP-8 (10 mL) was kept at the bottom of the cylinder and the same soil as that used in two-channel and four-column systems was packed uniformly up to 200 mL point. The soil was air dried. This column was kept in the laboratory for about 18 months and the weight loss was recorded periodically.

2.4. Soil Contamination

The soil systems were contaminated with jet fuel (JP-8). The physical properties of JP-8 used in the study are presented in Table 1. For the two channel system, at 20 locations in each channel, 3 mL of JP-8 was added twice in a month interval. Approximate locations were near plants which were on 10 cm centers. The overall contaminant concentration in the two-channel system was about 1700 mg of jet fuel/kg of dry soil. Water was added according to the water consumption rate by alfalfa plants. Column 1 and 4 received approximately 10 mL of JP-8 twice in a month interval. Column 2 and 3 received about 20 mL of JP-8 once. The overall contamination concentration in each column was about 2500 mg of jet fuel/kg of dry soil. Four cut-horse radish tubers (each weighed about 30 g wet weight) were planted in Column 2 and 3 on the same day.

2.5. Sampling and Analysis

For the two-channel system, plants were harvested every month and dry biomass was determined; soil samples were collected after three and five months and analyzed by GC. Either soil cores or box samples were taken in each channel at three depths (from top): 0-10, 10-20, and 20-30 cm. Composite samples were made for each depth and each row of each channel. Samples were frozen until analysis. Approximately 3 g of sub sample was taken from the composite and used in TPH extraction procedure described later. The analysis was replicated in triplets.

For four-column system, a destructive sampling was done after five months. Each column was divided into three segments (from top): 0-10, 10-20, and 20-30 cm. Soil from each segment was thoroughly mixed and a composite sample of about 500 g was taken and stored in a freezer until analysis. Approximately 200 g of soil out of 500 g was sent to the soil testing lab for physical and chemical analysis. Approximately 3 g of sub sample (in triplicates) was taken from each composite and used in the TPH extraction.

For the one-column system, a destructive sampling was done. The column was divided into four segments (from bottom): 0-50, 50-100, 100-150, 150-200 mL. Soil from each segment was thoroughly mixed and a 3 g sub sample was taken from each segment and used in the TPH extraction.

Extraction of petroleum hydrocarbons from soil was done by mechanical shaking procedure, developed by Schwab et al (1999). The procedure involved weighing approximately 3 g of soil in a foil lined 20 mL scintillation vial, adding 10 mL of optima® grade acetone and a matrix recovery standard, shaking for 30 min in a reciprocating platform shaker at 120 cycles/min, centrifuging for 10 min at 2100 rpm, and collecting supernatant in a 60 mL foil lined bottle. This was repeated three times. The extract was weighed and 1 mL of extract was transferred to a 2 mL GC vial along with an internal standard. A set of JP-8 standards were prepared with the same matrix and all GC vials were stored in the freezer until analysis.

Analysis of the sample was performed on a 5890A Gas Chromatograph (Hewlett-Packard, Avondale, PA) with chemstation® integration software and HP7673A auto sampler. The GC utilizes a DB-TPH column (J & W Scientific, Folsom, CA). The 5890 GC was equipped

with an FID (flame ionization detector). The column was specifically designed for analysis of total petroleum hydrocarbons, had dimensions of 0.32 mm inside diameter, a 30 m length, and 0.25 μm film thickness. The fuel and carrier gas was H_2 (99.999%). The carrier gas was delivered at 4.0 mL/min and the fuel gas at 40 mL/min. The make-up gas was N_2 (99.999%) at a flow rate of 32 mL/min. A support gas of zero grade air was delivered at 420 mL/min. The temperature program began at 40°C for 2 minutes and hiked at 12°C/min to 320°C, and was held at 320°C for a minute. The injection port and detector temperatures were 250°C and 350°C, respectively. The injection volume was 2 μL splitless. Values are reported as ppm (mg TPH/kg dry soil).

3. Results and Discussion

3.1. Alfalfa Production in Contaminated Soil

In general, alfalfa growth in the chamber was good. The above ground dry biomass production varied from 70-110 g/m²/30 days which corresponds to 7-11 metric ton/hectare/year. In Kansas, alfalfa production of 20 metric ton/hectare/year is considered to be a good yield under field conditions. The plants were grown under growth chamber conditions, lighted by artificial lights with relatively lower intensities, which resulted in lower yield under those conditions. Dry matter production was reasonable and alfalfa plants were not affected by JP-8 in soil.

3.2. Total Petroleum Hydrocarbons: Two-Channel System

Figure 1 shows the TPH levels in channel 1 after three months and Figure 2 shows the TPH levels in the front row after three and five months. The TPH levels varied with depth and the position of the row as well (Figure 1). Initially the overall contamination level was about 1700 mg of jet fuel/kg of dry soil. After three months, the mean concentration was decreased to 215 mg of jet fuel/kg of dry soil (with a standard deviation of 59 mg of jet fuel/kg of dry soil) in the top 10 cm of front row (Figure 1). The mean concentration at 10-20 cm depth was 1249 ppm with a standard deviation of 355 ppm and at 20-30 cm was 405 ppm with a standard deviation of 118 ppm (Figure 1). For the back row of channel 1, the concentration of jet fuel was below detectable limits (GC detection limit was 100 ppm) in the top 10 cm and bottom 10 cm (Figure 1). The concentration in the middle 10 cm was 242 ppm with standard deviation of 96 ppm (Figure 1). The reduction in jet fuel concentration in the front row of channel 1 varied from 87% (0-10 cm) to 27% (10-20 cm) (Figure 1). For the back row of channel 1, the reduction of JP-8 varied from about 97% (0-10 cm and 20-30 cm) to 85% (10-20 cm) (Figure 1). The standard deviation of JP-8 concentration for one depth (10-20 cm of front row) was higher than 25% of mean concentration (Figure 1). However, this much spatial variability is rather usual in similar systems (Schwab et al., 1999). This might be due to the extraction procedure itself (Schwab et al., 1999), sampling and sub sampling processes, and overall soil heterogeneity.

There is a significant reduction in TPH concentrations in the front row of channel 1 from 3rd to 5th month (Figure 2). During this two month period, the reduction in TPH concentration varied from 41% (10-20 cm) to 74% (20-30 cm). After five months, the mean jet fuel concentration in the front row of channel 1 ranged from 732 ppm (10-20 cm) to below the

detectable limit (0-10 cm). This clearly shows a significant reduction in the TPH concentrations. The overall reduction (over five months) of TPH concentration varied from 57% (10-20 cm) to 95% (0-10 cm)

Figure 3 shows the TPH levels in channel 2 during 3rd month and Figure 4 shows the TPH levels in the front row of channel 2 during 3rd and 5th months. After three months, the mean TPH concentration in the front row of channel 2 decreased to below detection limits in top 10 cm (Figure 3). The mean concentration in 10-20 cm was 198 ppm with standard deviation of 22 ppm and in 20-30 cm was 148 ppm with standard deviation of 99 ppm (Figure 3). For the back row of channel 2, the concentration of jet fuel was below detectable limits (GC detection limit was 100 ppm) in top 10 cm, middle 10 cm, and bottom 10 cm (Figure 3). The reduction in jet fuel concentration in the front row of channel 2 varied from about 97% (0-10 cm) to 88% (10-20 cm) (Figure 3). For the back row of the channel 2, the reduction of JP-8 was about 97% throughout the soil profile (Figure 3). The standard deviation of JP-8 concentration was higher than 25% of mean concentration in all the cases (even higher than 50% in two cases)(Figure 3). This might be due to the extraction procedure itself (Schwab et al., 1999), sampling and sub sampling processes, and due to overall soil heterogeneity.

There is a reduction of more than 35% in TPH concentrations in the front row of channel 2 from 3rd to 5th month(Figure 4). The TPH levels in 0-10 cm and 20-30 cm after five months were below detection limits and the TPH concentration in 10-20 cm was 128 ppm with standard deviation of 70 ppm (Figure 2). This clearly shows a significant reduction in the TPH concentrations.

3.3. Total Petroleum Hydrocarbons: Four-Column System

Figure 5 shows the TPH levels in different depths in four-column system after five months. The overall initial concentration was about 2500 ppm in all of the columns. For column 1, the mean TPH concentration was 101 ppm with a standard deviation of 88 ppm at 0-10 cm, 177 ppm with a standard deviation of 114 ppm at 10-20 cm, and 517 ppm with a standard deviation of 269 ppm at 20-30 cm (Figure 5). The reduction in jet fuel concentration in column 1 varied from 96% (0-10 cm) to 79% (20-30 cm) (Figure 5). In column 2, the TPH concentration was below detection limits in 0-10 cm, 769 ppm with a standard deviation of 98 ppm in 10-20 cm, and 237 ppm with a standard deviation of 91 ppm in 20-30 cm (Figure 5). The reduction in jet fuel concentration in column 2 varied from 97% (0-10 cm) to 69%(10-20 cm).

For column 3, the mean TPH concentration was below detectable limits at 0-10 cm, 901 ppm with a standard deviation of 330 ppm at 10-20 cm, and 822 ppm with a standard deviation of 210 ppm at 20-30 cm (Figure 5). The reduction in jet fuel concentration in column 3 varied from 97% (0-10 cm) to 64% (20-30 cm) (Figure 5). The TPH concentration was below detection limits in 0-10 cm, 137 ppm with a standard deviation of 97 ppm in 10-20 cm, and 777 ppm with a standard deviation of 175 ppm in 20-30 cm in column 4 (Figure 5). The reduction in jet fuel concentration in column 4 varied from 98% (0-10 cm) to 69%(10-20 cm). In general, the standard deviations were more than 25% from mean for

all the columns (Figure 5). This shows the heterogeneity of samples. Also, 3 g sub samples were taken from 300 g bulk samples which might not be a representative sampling.

In general, the TPH concentrations in the top 10 cm were below detection limits (Figure 5). The TPH concentration increased with depth for columns 1 and 4 that were unvegetated (Figure 5). Column 2 and 3 had the highest TPH concentrations in the middle 10 cm (Figure 5). It is evident that the TPH concentrations at the deeper soil profile were higher than the top 10 cm (Figure 5). This might be due to unfavorable conditions such as low oxygen concentrations at deeper soil profiles that may not facilitate biodegradation and/or other losses of jet fuel from the soil system. Unfortunately, most of the leaking of jet fuel and other petroleum hydrocarbons occurs at deeper soil profiles that makes cleaning up of those soils difficult. Plants can provide conducive environment through roots to those unfavorable zones by supplying oxygen and other nutrient sources for microorganisms that could degrade jet fuel.

3.4. Total Petroleum Hydrocarbons: One-column System

The TPH concentration for each segment was based on 3896 mg of JP-8 for the whole column. This corresponds to about 4.8 mL of JP-8. The periodic weight loss of the container was observed (data not shown). There was about 52% reduction in JP-8 over a period of 18 months. If we assume the air dried soil did not facilitate microbial growth, we can consider this dry soil system as a sterile control. This implies that about 48% of jet fuel was lost by abiotic losses such as volatilization and diffusion. We can conclude that if the reduction is more than 52% at any instance, that might be due to some other losses than abiotic. In our two-channel system and four-column system, the lowest overall reduction after five months was 57% (in two-channel system, channel 1) (Figure 2). But, for many of the cases the reduction was about 97% (Figure 2, 4, and 5). This clearly shows losses other than abiotic are a major fate of JP-8 in vegetated soils. This agrees with a previous study which was conducted with soils (Dean-Ross, 1992). However, that study was conducted only with 25 g of soil samples in milk dilution bottles (Dean-Ross, 1992). Our study shows some bioremediation of JP-8 contaminated soils with or without vegetation.

4. Summary

There was a significant decrease in JP-8 concentration in both two-channel and four-column systems. The losses were not just due to volatilization but also due to biodegradation. This is a promising result that shows managing the JP-8 contaminated soils, either by adding water and nutrients (by favoring microbial growth) or by growing plants (by favoring microbial growth indirectly), could result in faster restoration of those soils. Bioremediation or plant assisted bioremediation can be a feasible and inexpensive method to clean up JP-8 contaminated soils. Further studies should be conducted to assess the influences of plant-induced upward water movement on JP-8 biodegradation in soils.

5. Acknowledgment

This work was partially supported by the U. S. EPA and the U. S. Air Force through the Great Plains/Rocky Mountain Hazardous Substance Research Center under assistance agreements R-819653, R-825550, and R-825550. It has not been submitted to the EPA for peer review and, therefore, may not necessarily reflect the views of the agency and no official endorsement should be inferred. The center for Hazardous Substance Research Provided partial support. We acknowledge Dr. K. Xia for use of and assistance with the instrumentation in Throckmorton Plant Sciences Center, Kansas State University.

Table 1. Properties of Jet Fuel (JP-8) Used in the Study.

<u>Sl. no</u>	<u>Property</u>	
1	Specific Gravity	0.8
2	Color	Light Yellow
3	Distillation Boiling Point (°C)	
	Initial	159.5
	Final	263.5
	Average	215.2
4	Freezing Point (°C)	-48
5	Flash Point (°C)	56

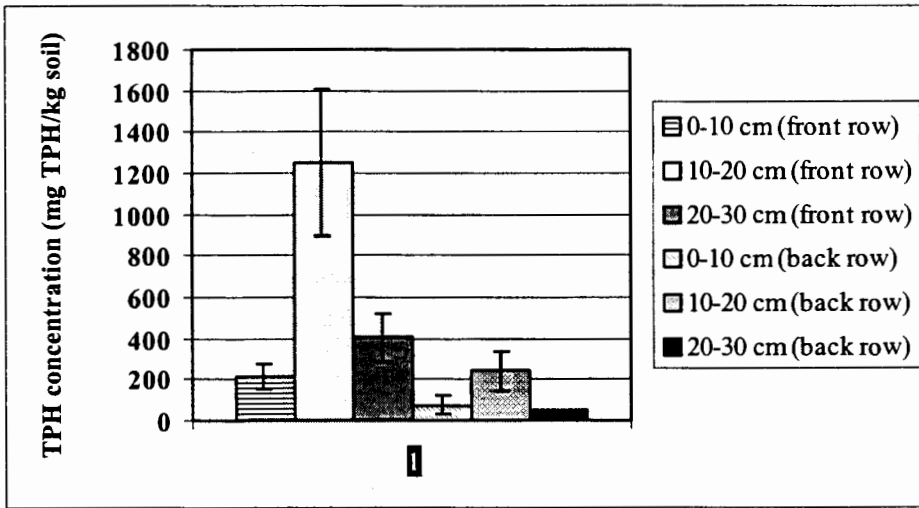


Figure 1. Total Petroleum Hydrocarbon Concentration in Two-Channel System (Channel 1) after Three Months.

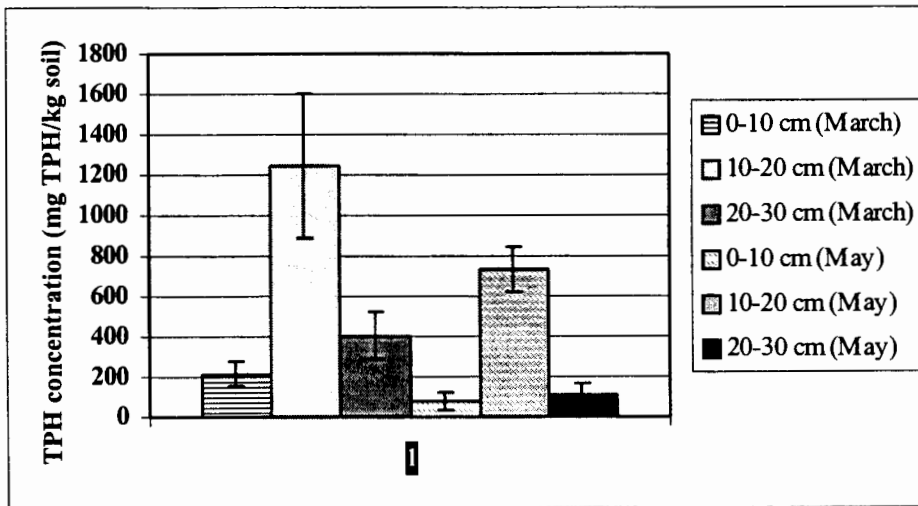


Figure 2. Total Petroleum Hydrocarbon Concentration in Two-Channel System (Channel 1: Front Row) during 3rd and 5th month.

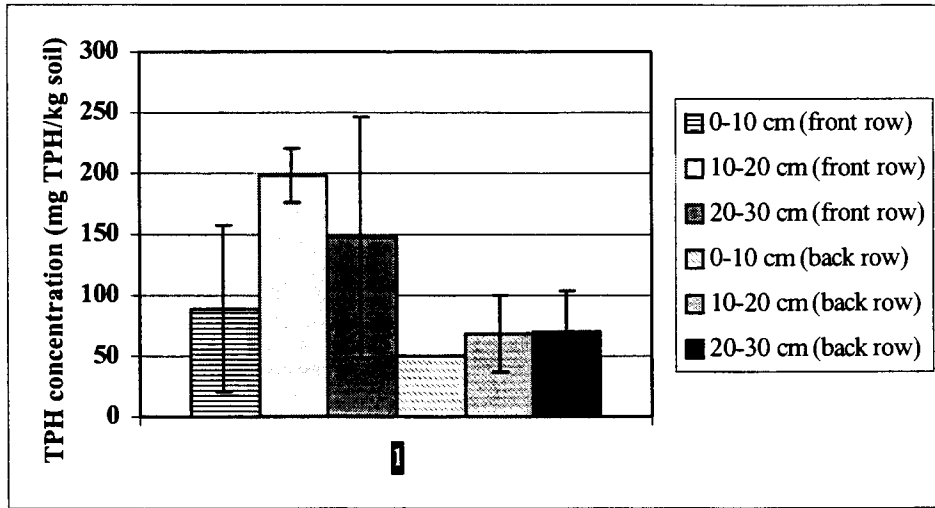


Figure 3. Total Petroleum Hydrocarbon Concentration in Two-Channel System (Channel 2) after Three Months.

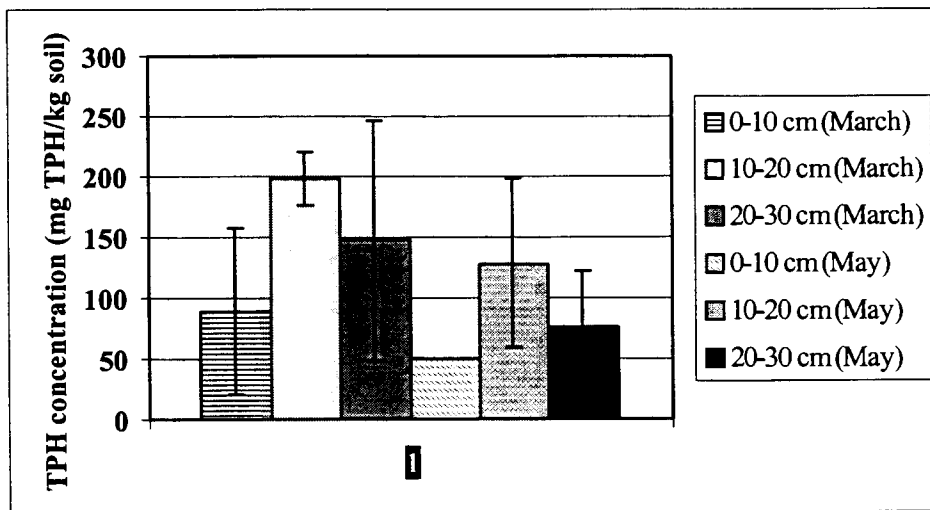


Figure 4. Total Petroleum Hydrocarbon Concentration in Two-Channel System (Channel 2: Front Row) during 3rd and 5th month.

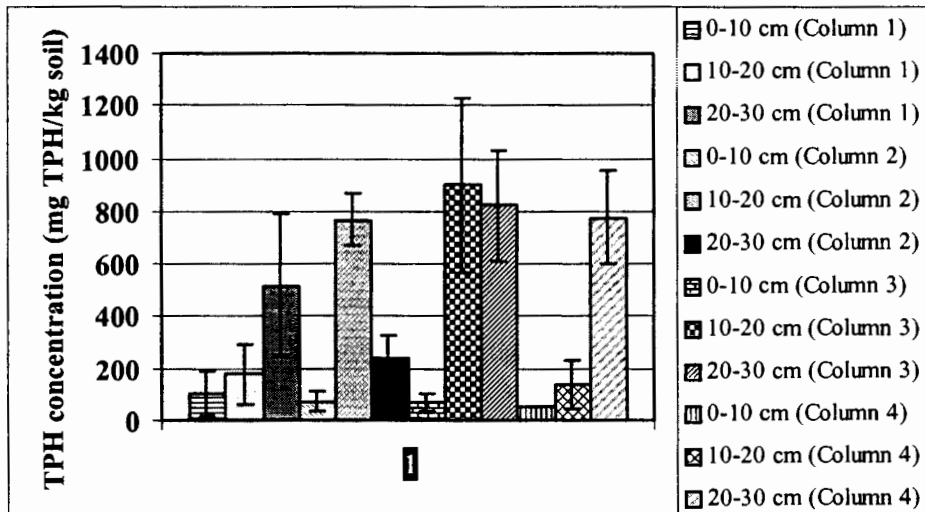


Figure 5. Total Petroleum Hydrocarbon Concentration in Four-Column System after Five Months.

6. References

- Aelion, C. M. and P. M. Bradley. 1991. Aerobic Biodegradation Potential of Subsurface Microorganisms from a Jet Fuel Contaminated Aquifer. Applied and Environmental Microbiology, 57:57-63.
- Dean-Ross, D., H. T. Mayfield, and J. C. Spain. 1992. Environmental Fate and Effects of Jet Fuel JP-8. Chemosphere, 24(2): 219-228.
- Dean-Ross, D. 1993. Fate of Jet Fuel JP-4 in Soil. Bulletin in Environmental Contamination and Toxicology, 51:596-599.
- Mayfield, H. T. 1996. JP-8 Composition and Variability. Interim Report, Armstrong Laboratory, Environics Directorate, Environmental Research Division, Tyndall AFB, FL, 32403. 27 p.
- Narayanan, M. 1994. Experimental and Modeling Studies on Bioremediation of Organic Contaminants in the Presence of Alfalfa Plants. MS thesis, Department of Chemical Engineering, Kansas State University, Manhattan, KS, 66505. 138 p.
- Schwab, A. P., J. Su, S. Wetzel, S. Pekarek, and M. K. Banks. 1999. Extraction of Petroleum Hydrocarbons from Soil by Mechanical Shaking. Environmental Science and Technology, 33(11): 1940-1945.
- Spain, J. C. and C. C. Somerville. 1985. Fate and Toxicity of High Density Missile Fuels RJ-5 and JP-9 in Aquatic Test Systems. Chemosphere, 14:239-248.

Bioprocessing effect on the stability of recombinant β -glucuronidase (rGUS) and its extractability from transgenic canola

Yun Bai¹ and Zivko L. Nikolov^{1,2}

¹Department of Chemical Engineering
Iowa State University, Ames, IA 50010

²ProdiGene Inc., College Station, TX 77845

ABSTRACT

Transgenic technology had opened up the possibility of producing heterologous proteins in plant hosts. In order to maintain the integrity of these recombinant proteins, current plant tissue processing strategies have to be reevaluated and modified if necessary. In this study, the feasibility of applying transgenic canola material on traditional canola processing was investigated by using β -glucuronidase (rGUS) as a model protein.

Different temperature treatments and organic solvent defatting effects on rGUS stability were reported in a previous paper (Bai and Nikolov, 1998). In this paper, the effect of material type, initial moisture content, and particle size on the rGUS stability and extractability was investigated. It was found that the lower the initial moisture content, the more stable the rGUS is. For the material with the same initial moisture content, rGUS activity seemed more stable in canola flakes than in whole seeds, which is most likely due to the larger surface area of the former, allowing more drying during incubation. As for rGUS extraction, smaller particles favored extraction because of their higher equilibrium concentration and lower time required to reach extraction equilibrium. For the materials with the same particle size, flaking improved rGUS extractability by potentially changing the microstructure compared to that of flours. The extraction efficiency was estimated by running Western blots and then scanned by densitometry. More than 80% rGUS was extracted by one-step NaPi buffer extraction, while including detergents (2-ME and SDS) into the extraction buffer did not further improve extractability.

INTRODUCTION

Recently many studies have focused on utilizing transgenic plants as "bioreactors" to produce various proteins with potential industrial or pharmaceutical uses (Austin et al., 1994; Krebbers et al., 1992; Pen et al., 1993; Whitlam et al., 1993). Advantages include the low cost of growing plants on large acreages, the ease of process scale-up, the availability of natural protein storage organs, and well-established practices for their efficient harvesting, transporting, storing, and processing. The most important reason is that the transgenic plants can carry out post-translational processes properly, which makes them one of the best alternatives of all eukaryotic production systems. There have been more than twenty different recombinant proteins expressed successfully in plant hosts since the first introduction of this technology in 1983 (Kusnadi et al., 1997). However, the relatively low accumulation levels of recombinant proteins and the insufficient information on downstream processing are still two major obstacles standing on the way of the fast development of producing valuable proteins in plant hosts.

Canola has been widely used as a source of oil (40% of total weight) and protein (25-30% of total weight). The traditional canola processing method consists of seed preconditioning, cooking, flaking, oil pressing and hexane extraction (Norris et al., 1982; Shahidi, 1990). Based on the

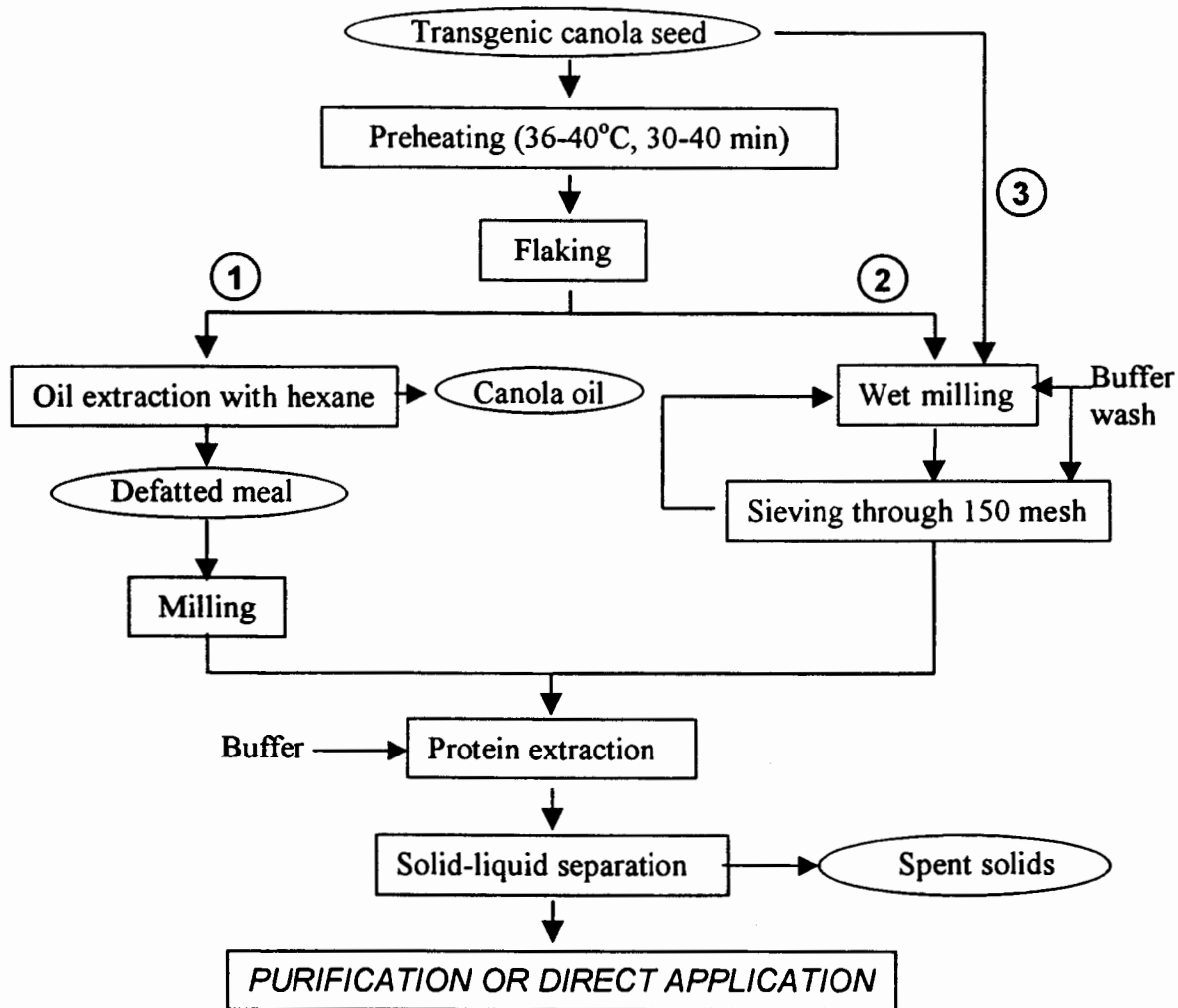


Fig 1: Proposed process flow diagram for processing of canola

extensive study of the traditional canola seed processing and the awareness of the new properties of rGUS, we proposed the above integrated flowchart for transgenic canola processing (Figure 1). There are three routes involved in this process. The first route keeps most steps of regular canola processing. Transgenic seed can be preconditioned, flaked and hexane extracted to collect oil product. The defatted meal will be further ground and extracted for recombinant protein. After solid liquid separation and clarification, the recombinant protein can be purified to get target protein. The second and third routes are much shorter because some of the steps, such as solvent extraction, dry milling, and even flaking are bypassed. The potential problems caused by the different temperature treatments and organic solvent extraction as well as the high pressure and high shear force during seed flaking and wet-grinding had been researched in our previous study (Bai and Nikolov, 1998). This work, as a continuous study, mainly focused on the effect of the moisture content and particle characteristics (size and microstructure) on the recombinant protein stability and extractability.

MATERIALS AND METHODS

Processing and extraction methods

Dry grinding and extraction.

Full-fat canola flour was prepared by grinding the whole seed with a high-speed flour mill (Magic Mill, Salt Lake City, Utah). One gram of canola flour was extracted with 10 ml 50mM NaPi buffer of pH 7.5 (1:10 solid-to-liquid ratio). The suspension was shaken at room temperature in an orbital shaker (Labline, Melrose Park, Ill.) for 30 min at 250 rpm before centrifugation.

Wet grinding and extraction

Whole canola seed (1 g) was mixed with 10 ml of 50 mM NaPi buffer at pH 7.5 and wet-ground with a laboratory homogenizer (Janke & Kunkel, Germany) at 17,000 rpm and 15°C for less than 1 min. The slurry was incubated at room temperature for 10 min without shaking before centrifugation.

The slurry prepared by either wet or dry-grinding process was first centrifuged (Beckman Model JA2-21 centrifuge, 11,000 rpm, 23°C) to remove insoluble solids. The supernatant was then filtered through Whatman No. 4 filter paper to remove the light oil-rich fraction (cream).

Initial moisture content effect

To study the initial effect of moisture content (MC) on rGUS heat stability, canola seeds and flakes were desiccated in a drykeeper (Santo Co., Japan) for different times to reduce the MC to a predetermined level. The initial MC for the whole seeds and flakes was 12% and 9%, respectively. After 2 h of desiccation, the MC of the whole seeds decreased to 9%, and after 5 h to 6%. For canola flakes, 2.5 h was needed to decrease the MC from 9% to 6%. The heat stability testing as a function of the MC was performed at 70°C. Three 2-g samples for each seed type were taken out and homogenized at 0, 2, 4, 6, and 10 h, respectively. Extracts were collected and assayed for residual rGUS activity and total extractable protein.

Particle size effect

Defatted canola flakes were dry-ground and fractionated through a series of standard testing sieves (No. 30, 40, 50, 70, 100, 120, Fisher Scientific, Philadelphia, Pa.) by using a Ro-Tap testing sieve shaker (W. S. Tyler, Mentor, Ohio) for 20 min. Five fractions with average particle sizes of 138, 180, 255, 363 and 513 μm were used to measure the kinetics of protein and rGUS extraction. Ten grams of each fraction were extracted with 200 ml extraction buffer for up to 2 h at ambient temperature by using a four-bladed turbine propeller (HST210N, Glas-Col, Terre Haute, Ind.). Stirring above 600 rpm eliminated the external mass transfer resistance to protein extraction (data not shown), and 1500 rpm was used in all experiments in order to keep the particles suspended. Slurry aliquots (0.5 ml) were taken out at a specified time and centrifuged immediately to stop the extraction. All extracts were kept at 4°C for analysis of rGUS activity and total protein.

Extraction efficiency

The extraction efficiency was estimated by comparing the amount of rGUS in the canola solids before and after an aqueous extraction. Each sample (2 g) was extracted in two steps using 20 ml of sodium phosphate buffer (pH 7.5). After the first extraction, the spent solids were rinsed with distilled water, dried at room temperature, ground by a mortar and pestle, and re-extracted

with the same buffer. The same extraction procedure was repeated except this time the buffer contained 1% SDS and 2% 2-ME. The four extracted solids obtained from the two extractions were analyzed for residual rGUS by Western blotting.

Analytical Methods

Protein and rGUS activity

rGUS activity (Jefferson et al. 1991) and total soluble protein (Bio-Rad Coomassie Plus Protein Assay) in the clarified aqueous extract were determined according to the cited standard protocols. All experiments were performed in duplicate.

SDS-PAGE and Western blotting

SDS-PAGE and Western blotting were performed as previously described (Kusnadi et al., 1998a) except that a 4-20% Tris-HCl gradient gel (Bio-Rad, Hercules, Cal.) was used for the electrophoresis and a Bio-Rad PVDF membrane was used for the Western blot. The immunoreactive protein bands on the Western blot membrane were developed by using Amersham's enhanced chemiluminescence (ECL) protocol (Amersham Life Science, England) and quantified by densitometry. Commercial *E.coli* GUS samples (Sigma, St. Louis, Mo.) with total amount from 0.002 to 0.02 µg were used as standard.

RESULTS AND DISCUSSIONS

Initial moisture content on rGUS heat stability

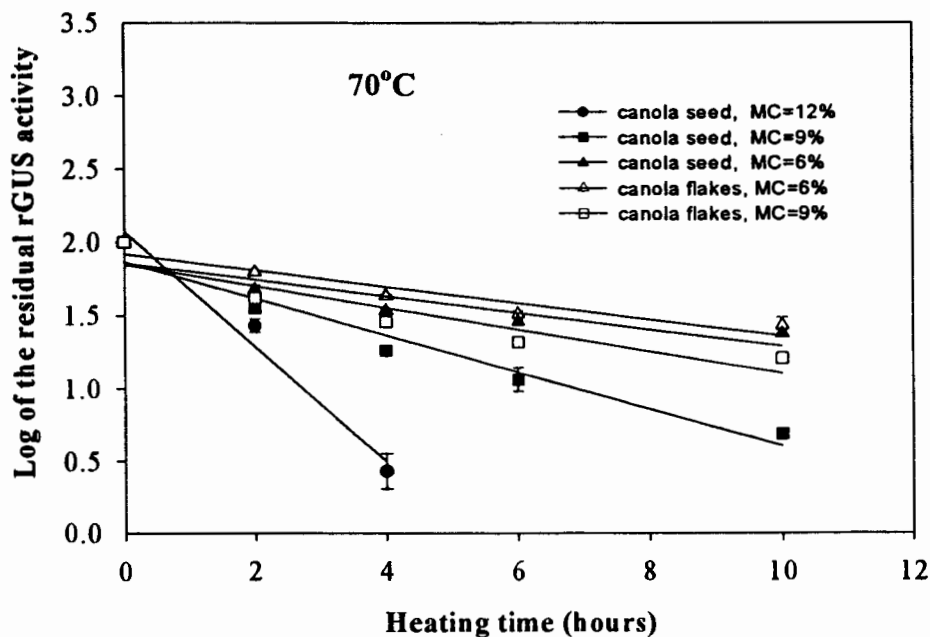


Figure 2. Effect of initial moisture content (MC) on enzyme stability at 70°C

To determine the effect of the initial moisture content on enzyme stability, whole canola seeds and flakes were exposed to 70°C for up to 10 h (Figure 2). Enzyme deactivation followed a first-order reaction by showing a straight line on the semi-log profile. The steeper the regression line, the faster the enzyme lost activity. Decreasing the initial MC of the whole seed from 12% to 9%, then to 6%(w/w) increased enzyme stability by showing a much flatter line. Generally, flakes is more stable than the whole seed with the same initial MC and the major difference between the whole seeds and flakes is that the latter has much larger specific surface area, which probably caused a faster moisture loss during heating. However, in the case of really low MC (6% for instance), flakes and whole seed exhibited similar thermostability, those two lines are almost parallel to each other. Our experimental data also showed that after 10 h of incubation, only three out of the five samples contained extractable enzyme activity, and the two samples with 6% initial moisture had greater than 20% residual GUS activity.

In summary, both lower initial MC and faster moisture loss during incubation increased enzyme thermostability.

Particle size effect on rGUS extraction

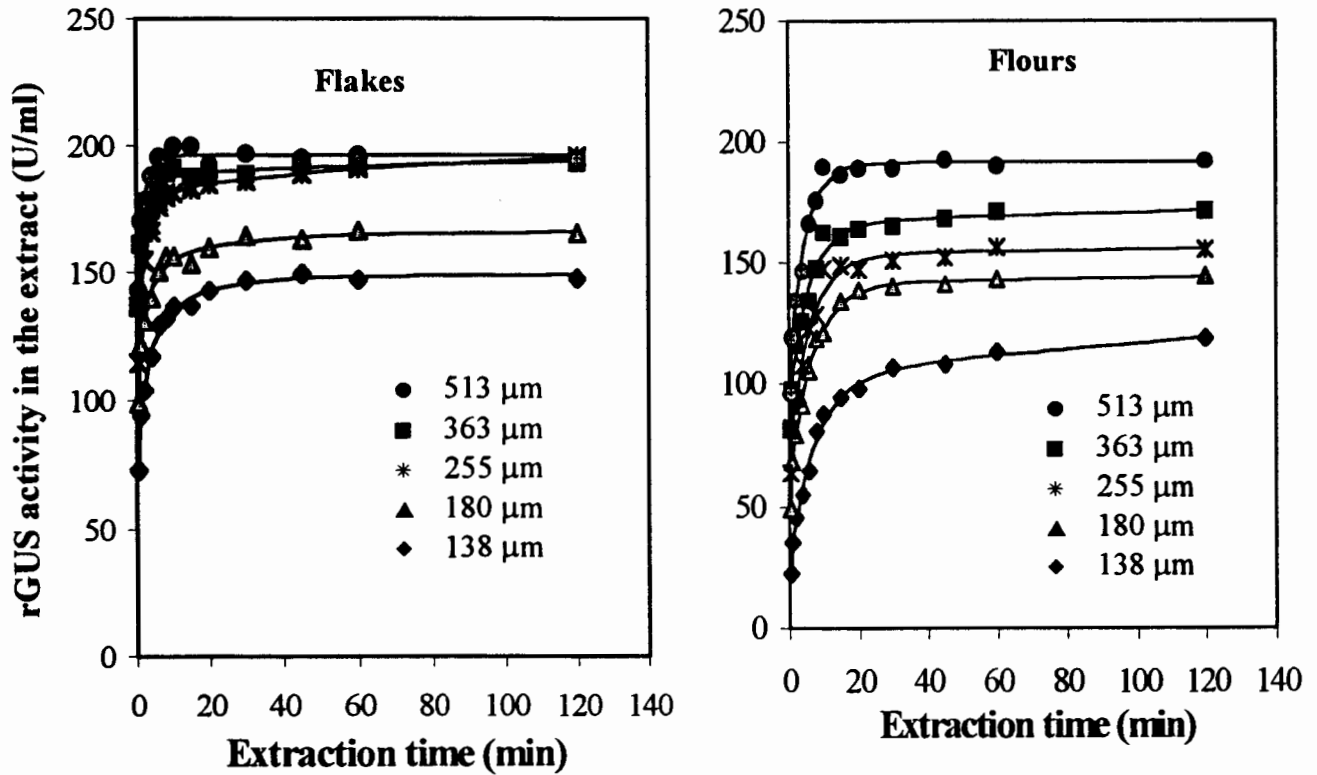


Figure 3. Particle size effect on rGUS extraction kinetics

Because the fractionation of full-fat samples by sifting is very difficult due to particle agglomeration, we investigated the particle size effect on protein extraction by using defatted samples. The kinetics of rGUS and canola protein extraction from fractionated samples with an average particle size of 138, 180, 255, 363 and 513 μm are compared in Figure 3. Generally, 20-30% more rGUS and canola protein were extracted after 2 h from particles equal to or smaller

than 255 μ m in size. By analogy to the oil extraction from canola (So and Macdonald, 1986), the sugar from sugar beet (Soddu and Gioia, 1979), the protein from defatted lupin seed (Aguilera et al., 1989), the extraction of canola protein and rGUS can be described by 1) an almost instantaneous washing of the protein from broken cells on the surface and 2) a slow intraparticle diffusion-controlled process. As shown in Figure 3, the initial concentration of canola protein and rGUS in the extract increased as the average particle size decreased. Typically, the “zero-time” samples were taken within 30 sec after mixing the flour and the buffer. In all cases, the initial rGUS or protein concentration in the extract represents the available protein on the surface of the particle, which was almost instantaneously transferred into the solution upon contacting the flour and the buffer. Therefore, in the absence of external mass transfer resistance, the measured initial concentrations should be proportional to the specific surface area. The second segment of the extraction curves represents the diffusion-controlled extraction. The significantly lower rGUS activity recovered from the particles of 363 and 513 μ m in size is an indication of the slower extraction kinetics, probably due to greater diffusion path length. Although none of the tested samples had reached the solid-liquid equilibrium after 2 hours, the particles larger than 255 μ m were still far from the equilibrium rGUS concentration, which should be independent of the particle size (So and Macdonalad, 1986). In practice, no longer than two hours of solid-liquid contact time, including filling and emptying of the extraction vessel, is expected. The kinetic data demonstrate that if canola is ground to less than 255 μ m, 90% of the maximum extraction yield of rGUS can be achieved in 10 min.

Extraction Efficiency

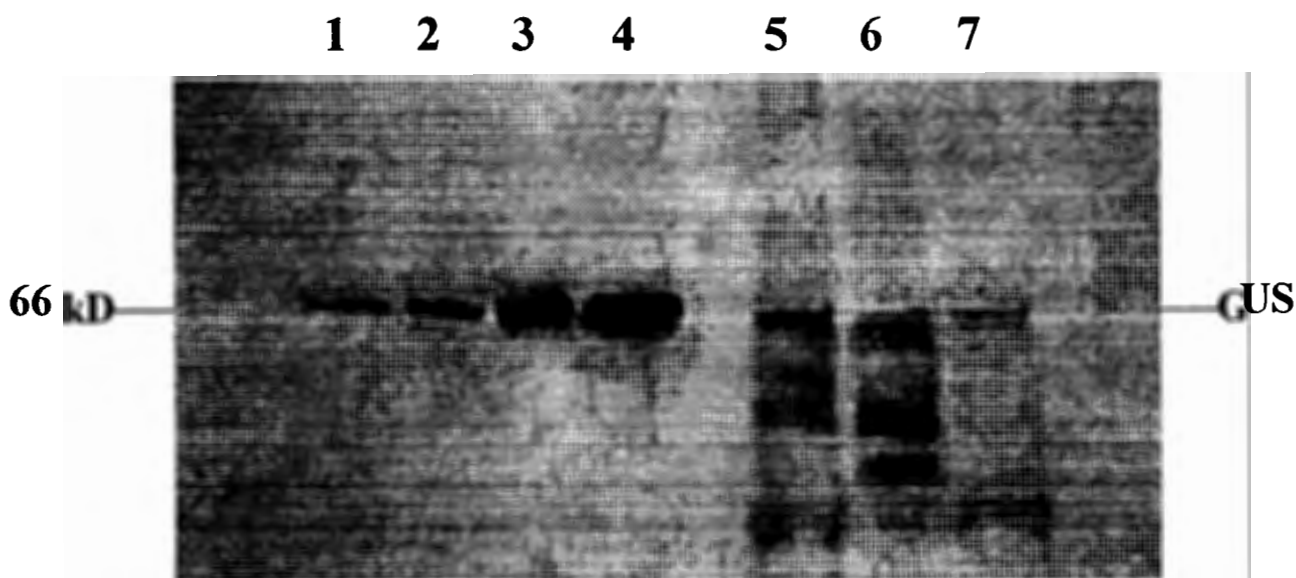


Figure 4. Western blot analysis of canola solids before and after extraction. Lanes (1-4), GUS standard; Lane (5), solids before extraction; Lane (6), solids after extraction at pH 7.5 without 2-ME and SDS; Lane (7), solids after extraction at pH 7.5 with 2-ME and SDS.

To determine the maximum achievable extraction of rGUS after 2 h of extraction, the spent solids from a 255 μ m sample were analyzed by SDS-PAGE and Western blotting (Figure 4, lanes 6 and 7). Lane 5 contains the positive control (the solids before extraction), and lanes 6 and 7 contain the spent solids after the first extraction. The visible bands (around 66 kDa) in lanes 6 and 7, which correspond to rGUS, imply an incomplete extraction. By comparing the band densities in lanes 5, 6 and 7, we estimated that about 85% of rGUS was extracted in the first extraction with the NaPi buffer. This amount was similar to that recovered by including SDS and 2-ME in the buffer. The residual rGUS in the spent solids after the second extraction was below the detection level on the Western blot. Therefore, rGUS extraction efficiency from canola was greater than that from transgenic corn (70%). In addition, the presence of 1% SDS and 2% 2-ME in the extraction buffer resulted in a complete extraction of rGUS from the corn meal (Kusnadi et al, 1998b), but apparently did not affect the enzyme extraction yield from canola.

CONCLUSIONS

Initial moisture content and the rate of loss of moisture content during canola tissue storage or incubation are two important factors affecting recombinant enzyme stability. Particle size and microstructure played an important role in rGUS extraction kinetics. A faster extraction and a higher extraction yield were achieved by extracting flaked particles with an average size equal to or smaller than 255 μ m. Further size reduction did not substantially increase the extraction yield. With the aid of Western blot and densitometry, above than 80% of total rGUS was estimated to be extracted in one stage aqueous extraction.

ACKNOWLEDGEMENT

This research was partly supported by grants from USDA/NRI and NSF. We want to thank ProdiGene Inc. and Pioneer Hi-Bred International Inc. for providing the transgenic canola seed. We would also like to thank Dr. Kusnadi for suggestions and help.

REFERENCES

- Aguilera, J.M.; Garcia, H.D. Protein extraction from lupin seeds: a mathematical model. *Int. J. Food Sci. Technol.* 1989, 24, 17-27.
- Austin, S., Bingham, E.T., Koegel, R.G., Mathews, D.E., Shahan, M.N., Sranb, R.J., Burgess, R.R. 1994. An overview of a feasibility study for the production of industrial enzymes in transgenic alfalfa. *Ann. N. Y. Acad. Sci.* 721:235-244.
- Bai, Y. and Nikolov, Z.L. 1998. Effect of processing on the recovery of recombinant β -glucuronidase from transgenic canola. In "Proceedings of the 28th Ann. Biochem. Eng. Symp.", P. J. Reilly, eds., pp. 69-76.
- Jefferson, R.A., Wilson, K.J. 1991. The GUS gene fusion system. In "Plant molecular biology manual", Vol. 1, B14, S.B. Gelven, R.A. Schilperoort, and D.P.S. Verma, eds., Kluwer, Dordrecht, pp. 1-33.
- Krebbers, E.; Bosch, D.; Vandekerckhove, J., 1992, Prospects and progress in the production of foreign proteins and peptides in transgenic plants. In "Plant protein engineering", Shewry, P. R, Gutteridges, S., eds.; Cambridge University Press: London, pp 315-325.

- Kusnadi, A.R., Nikolov, Z.L., Howard, J.A. 1997. Production of recombinant proteins in transgenic plants: Practical considerations. *Biotechnol. Bioeng.* 56, 473-484.
- Kusnadi, A.R., Evangelista, R.L., Hood, E.E., Derrick, R.W., Howard, J.A., Nikolov, Z.L. 1998a. Processing of transgenic corn seed and its effect on the recovery of recombinant β -glucuronidase. *Biotechnol. Bioeng.* 60, 44-52.
- Kusnadi, A.R., Hood, E.E., Derrick, R.W., Howard, J.A., Nikolov, Z.L. 1998b. Production and purification of two recombinant proteins from transgenic corn. *Biotechnol. Prog.* 14, 149-155.
- Norris, F.A. 1982. Extraction of fats and oils, in "Bailey's industrial oil and fat products", 4th ed., D. Swern., ed., New York: Wiley, pp. 207-214.
- Pen, J.; Sijmons, P. C.; van Ooijen, A. J. J.; Hoekema, A., 1993. Protein production in transgenic crops: analysis of plant molecular farming. In "Transgenic plants fundamentals and applications", Hiatt, A., ed., Marcel Dekker: New York, pp. 239-251.
- Shahidi, F. 1990. In "Canola and rapeseed: Production, chemistry, nutrition and processing technology", Van Nostrand Reinhold, New York, pp. 235-249.
- Salunkhe, D.K., Chavan, J.K., Adsule, R.N., Kadam, S.S. 1991. In "World oil seeds: chemistry, technology, and utilization", Van Nosrand Reinhold, New York, pp. 81-83.
- So, G.C.; Macdonald, D.G., 1986. Kinetics of oil extraction from canola (rapeseed). *Can. J. Chem. Eng.*, 64, 80-86.
- Soddu, A.; Gioia, F., 1979. Diffusion through living systems: Sugar loss from sugar beets. *Chem. Eng. Sci.*, 34, 763-773.
- Whitelam, G.C., Cockburn, B., Gandecha, A.R., Owen, M.R.L. 1993. Heterologous protein production in transgenic plants. *Biotechnol. Genet. Eng. Rev.* 11, 1-29.

MULTISTAGE ELECTROPHORESIS

Shramik Sengupta, Paul Todd, John Vellinger* and K.S.M.S Raghavarao**

Department of Chemical Engineering, University of Colorado, Boulder, CO 80309

*SHOT, Inc., 5605 Featherengill Road, Floyd Knobs, IN 47119

** (Present Address) Central Food Technology Research Institute, Mysore, India

© 1999 Shramik Sengupta, Paul Todd, John Vellinger, K.S.M.S Raghavarao

Presented at the 29th Annual Biochemical Engineering Symposium – Norman OK
Unpublished

Abstract

The electrophoretic separation of proteins and particles without gels has been a long standing goal of separations research. However, the process of electrophoresis has so far been unable to “graduate” from an analytical tool to a viable unit operation. This is primarily because of various problems such as thermal convection, particle sedimentation, droplet sedimentation, and electro-hydrodynamic zone distortion have been found to be major obstacles to scale-up. Without the need to prepare density gradients and / or use elaborate flowing systems, free electrophoresis could enjoy much more widespread use because it is a high resolution method that does not require adsorption to solid media and the subsequent solids handling. Besides, it can separate particles (cells) and solutes (macromolecules) with equal ease. Based on research experience, it was believed that the overall efficacy of electrophoresis as an unit operation could be greatly improved if (a) the migration distance were greatly reduced and (b) the process was multistaged. The current approach seeks to incorporate both features (a short migration distance and a multistage operation technique) with a view to making the process easier to operate as a whole.

The separation unit consisted of two plates with opposing right cylindrical cavities into which samples are loaded as in multistage two-phase partitioning. These plates can be rotated with respect to each other and thus the cavities can be aligned or separated as desired. the two-phase aqueous partitioning. This device, ELECSEP, was conceived to work with oppositely charged electrodes at the ends of the two cavities providing the electric driving force for the migration of particles. Unlike many other separation processes, electrophoresis is a kinetically driven and not an equilibrium limited process. That is, components are separated on the basis of electrophoretic mobility. An initial transport model was derived which tracked the migration of two different types of particles from one cavity to the corresponding collecting cavities. In addition, a “pseudoequilibrium” model was developed which could be used to predict the optimum duration of application of the electric field in order to maximize the purity of each separand. An additional goal was to figure out how to further enrich the mixture obtained

from one cycle of the process and keep doing this in a stepwise manner to achieve further purification. In terms of a classical chemical engineering separation process, this is equivalent to calculating the operating line. A corollary to calculating the operating line is the development of protocols which outline the handling of the various fluids and mixtures. This has been done for the most general case- when we wish to isolate some types of separand and discard other types from a suspension with many species of contaminants

Basic Technology

Electrophoresis is a leading method for resolving mixtures of cells or charged macromolecules (proteins and nucleic acids). The electrophoretic separation of proteins without gels has been a long-standing goal of separations research. However, the process of electrophoresis has so far been unable to “graduate” from an analytical tool to a viable unit operation. This is primarily because of various problems such as thermal convection electro-osmosis, particle sedimentation, droplet sedimentation, particle aggregation and electro-hydrodynamic zone distortion that have proved to be major obstacles to scale-up. These deterrents have led to such measures as radial electrophoresis in Couette flow, free flow electrophoresis, low gravity electrophoresis, and reorienting density gradient electrophoresis; to name a few. The last mentioned ⁽¹⁾ exploits the notion of electrophoresis in a short vertical path, and this concept forms the basis of multistage electrophoresis.

Based on research experience, it was considered that the overall effectiveness of electrophoresis as a unit operation would be greatly enhanced if (a) the migration distance were greatly reduced and (b) the process were multi-staged. The latter concept has not been previously implemented in electrophoresis. The current work seeks to incorporate both features (a short migration distance and a multistage operation technique) with a view to increasing the throughput of the process and to making the process easier to operate as a whole.

Engineering Models

The Multistage System.

The precursor to the Multistage Electrophoretic Separation (ELECSEP) unit was the Advanced Separation (ADSEP) unit developed by SHOT Inc. ⁽²⁾, which was designed for multi-staged aqueous two-phase extraction. The ELECSEP was conceived to work in a similar manner, with oppositely charged electrodes at the ends of the two cavities providing the electric driving force for the migration of the particles. The ELECSEP hardware is a combination of free electrophoresis and multistage extraction and consists of 20 or more cavities of a multi-stage thin-layer extraction system. Half-cavities oppose each other in disks that are sealed together and rotate with respect to each other. The mixture to be separated starts in a bottom cavity, and successive top cavities collect fractions; as separand particles move upward out of the bottom cavity. The half-cavities

are disk shaped; the top cavities having flat tops and the bottom cavities having flat bottoms. These two surfaces consist of palladium (Pd) metal electrodes that produce an electric field when the two cavities are in contact. Each half-cavity is only a few mm in height so that the fluid within it remains isothermal during the application of the electric field.

Two models were formulated to describe the process. The first model (called the constant - potential model) was used to predict the number of particles migrating to the upper half-cavity as a function of time and the strength of the applied electric field. The second model (called the pseudo-equilibrium model) was applied to a two-particle mixture, and was used to determine the optimum degree of separation or enrichment possible with the given dimensions of the ELECSEP

In the presence of an electric field (E), the velocity of a particle (v) of type A is given by the equation

$$v = \mu_A E \quad (1)$$

where μ_A is the electrophoretic mobility of the particle. This is the basic equation used to derive all other equations in the two operating models that follow.

3.1 The Constant Potential Operating Model

The constant voltage model may be used to monitor the migration of different types of particles. In this model, we keep track of the number of particles of each type present in each chamber as these particles migrate from the bottom to the top chambers. An important feature of this model is that it tracks the migration of particles with different electrophoretic mobility independent of each other. If a sample initially placed in one of the bottom cavities of the ELECSEP is exposed to an upper cavity, and an electric field is generated for a fixed time τ , then the number of particles of type A that are transferred to the top is given by the equation

$$n_{A(i)} = \frac{[\mu_A E \tau \pi R^2]}{(H/2)\pi R^2} [N_A]_{(i-1)} \quad (2)$$

where (H/2) is the height of each top or bottom cavity, R is the radius of the cavities, n_{Ai} is the number of particles of type A transferred during the ith step.

The mass balance for consecutive stages can be also written as

$$[N_A]_{(i)} = [N_A]_{(i-1)} - n_{A(i)} \quad (3)$$

Similar equations can be written for all types of particles. It is then seen that the model predicts that after each step, relatively fewer particles with relatively higher electrophoretic mobilities remain in the bottom cavity. Thus, initially, the top cavities

become richer in the faster moving particles and top cavities of the later stages are richer in the slower moving particles.

The Pseudo-Equilibrium Model

The pseudo-equilibrium model can be used to monitor the separation of two types of particles with different electrophoretic mobility. In this model we track the particle fraction of a given type of particle in a fluid sample. (As opposed to the concentration in terms of say “number of particles per ml” that we tracked in the previous model). The particle fraction of a certain type of particle is the ratio of the number of particles of that type in a unit volume of suspension to the total number of particles (of both types) in the same unit volume of the suspension.

If the mixture that we want to resolve consists of two different types of particles with different electrophoretic mobility, the pseudo-equilibrium model gives us the optimum duration for which the electric field needs to be applied in order to achieve the greatest resolution (in terms of particle fraction). It also enables us to predict the highest possible particle fraction of the more mobile species in the extract as a function of its particle fraction in the feed, and the mobility ratio (ratio of the electrophoretic mobility of the slower particle type to that of the faster particle type). The former parameter of the process (which we call the critical time) is given by the equation

$$t = H / \mu_A E \quad (4)$$

The highest possible particle fraction of the more mobile species in the extract is given by the equation

$$Y_{Ai}^* = \frac{1}{\left(1 - \frac{\mu_B}{\mu_A}\right) + \frac{1}{X_{Ai}} \left(\frac{\mu_B}{\mu_A}\right)} \quad (5)$$

where X_A is the particle fraction of particles of type A in the feed.

The graphical representation of equation (2) for different values of the mobility ratio turns out to be quite similar to the equilibrium curves commonly encountered in chemical engineering literature. Furthermore, if we propose to use the extract from one stage as feed for the next stage, we can use the 45° line ($Y^* = X$) as our operating line. Thus we can calculate the number of stages that we need to obtain the desired purity by a method similar to the classical McCabe Thiele Method.

Thermal model

As current passes through the sample in the cavities during electrophoresis, heat is generated. Since the two operating models implicitly assume that the effects of this heat generation can be neglected, a thermal model was also developed to substantiate the validity of this assumption. According to this model, the rate of temperature increase is given by the equation

$$\frac{dT}{dt} = \frac{I^2 H}{\pi R^2 K C_p} \quad (6)$$

where K is the conductivity of the sample in the cavities.

On inserting the appropriate values into the above equation, we obtain a predicted rate of temperature increase of 0.022 °C/s for a low conductivity buffer (0.002 M phosphate buffer)

Experiments

Particle migration experiments

The constant-potential model has been verified so far by monitoring the migration of sulfated polystyrene latex particles (Interfacial Dynamics Corp., Portland, OR). The feed had an initial concentration of 5.5×10^6 particles/ml. Field strengths of 5 or 10 V/cm. Were applied for 60 s per transfer for up to 8 transfers. 4.5×10^6 particles were extracted in 6 transfers using a field of 5 V/cm while the same number was extracted in 3 transfers using a field of strength 10 V/cm. This is in keeping with our constant potential model. Experiments to validate the pseudo-equilibrium model have not yet been completed.

Thermal experiments

The generation of sensible heat was monitored in a single cavity and the rate of increase in temperature was found to be 0.0092 °C/s, indicating that approximately half of the heat was lost to the surroundings (including the poly-carbonate ELECSEP plate).

Conclusions

The principle of multistage electrophoresis has been presented for the first time. Two elementary models of its operation have been described and one of them (the constant potential model) has been subjected to experimental tests. Also, a static adiabatic thermal model indicates that bare non-gassing Pd electrodes can be used in low-field applications. However further work needs to be done to verify the Pseudo-equilibrium model and to extend it to handle multi-particle separations.

Acknowledgements

- (1) SHOT Inc., Floyd Knobs, IN is acknowledged for sponsoring the research.
- (2) The Govt. of India is also acknowledged for sponsoring the sabbatical stay of Dr. Raghavarao at the University of Colorado at Boulder

References

- (1) Tulp A, Timmerman A and Bornhorn MG (1983) In : Electrophoresis '82 (Ed D. Stathakos) deGruyter & Co. , Berlin ; page 317
- (2) Deuser M, Vellinger JC , Naumann RJ, Guinn MR and Todd P (1995)
“Apparatus for two phase partitioning for terrestrial and space applications.”
AIAA Life Sciences and Biomedical Conference 1995 (Houston, TX)
Book of Abstracts 95-LS-42, pages 65-66.

Micropatterned Biodegradable Polymer Films for Peripheral Nerve Regeneration

Cheryl Miller¹, Carole Heath^{1,2} and Surya Mallapragada^{1,2,*}

¹Biomedical Engineering Program and ²Department of Chemical Engineering
Iowa State University, Ames, Iowa 50011

Abstract

Over 200,000 surgeries to repair peripheral nerve damage are attempted annually (Med. Dev., 1985). For successful nerve regeneration, the neurite growth cone uses environmental cues, both physical and chemical, to reinnervate the effector organ. To study how the neurite uses physical cues, micrometer-sized grooves fabricated on biodegradable polymer films are created to form physical boundaries that act as physical guidance. The neurite uses chemical stimulus by detecting and responding to diffusible cues that improve neuron outgrowth. Schwann cells seeded into the microgrooves coated with laminin provide neurotrophic factors for the regenerating neuron.

Unlike previous studies that used either physical or chemical guidance, both physical and chemical guidance mechanisms are utilized in this study by the fabrication of grooves on the substrate surface and seeding Schwann cells into laminin-lined grooves. Neurons from rat dorsal root ganglia are placed on the grooved films of poly(DL-lactide) and poly (DL-lactide-*co*-glycolide) to analyze the effect of the grooves on the directional growth of the neurons and the effect of groove size on neuron regeneration. Daily photomicrographs are taken to examine axon extension and growth cone navigational changes. Schwann cells placed in the grooves and their effect on the growth of the neurons are also being investigated.

Introduction

The peripheral nervous system is composed of blood vessels, connective tissues, axons and Schwann cells. The peripheral nervous system uses bundles of nerve fibers called axons to deliver sensory information to the central nervous system and convey motor commands to peripheral tissue.

Under physiological conditions, when an axon is transected, Wallerian degeneration occurs and can be followed by a reparative phase since the proximal segment maintains its continuity with the neuron cell body. The proximal segment of the axon initially degenerates close to the wound then starts to grow after debris is removed by macrophages. The distal portion of the axon degenerates completely. The axon and its myelin sheath are consumed by macrophages and Schwann cells, leaving the connective tissue remains to form natural conduits (Junqueira et al., 1983). As the myelin degenerates, the Schwann cells dedifferentiate and proliferate within the remaining connective tissue then align in rows which act as guides the regenerating axons and assist in axonal regrowth (Kandel and Schwartz, 1985).

During Wallerian degeneration, nerve growth factor (NGF) and laminin are expressed (Tonge et al., 1997). The Schwann cells near the edge of the wound on the proximal stump and the Schwann cells distal to the transection synthesize and secrete NGF that binds to NGF receptors on the Schwann cell surface. As the neurite reaches the NGF receptors and uses the NGF, the receptors are turned off with axonal contact, drawing the neurite to the next Schwann cell. The NGF exerts both trophic and tropic influence on the elongating axons, substrate and chemo-

tactic influence, respectively (Gilmore and Sims, 1995). Schwann cells also modify their surrounds by synthesizing and secreting extracellular matrix (ECM). The ECM components organize into basal lamina and surround mature Schwann-axon units causing neurite elongation during regeneration (Gundersen, 1987). Laminin is one ECM component that is continuously synthesized by Schwann cells to mediate interactions between the ECM and other cells.

Manipulation of the neurite growth cone is essential to reinnervate regenerating neurons. The growth cone uses environmental cues, both physical and chemical, as guidance mechanisms to reach the effector organ. The physical guidance of the neurons is dependent on the adhesive interaction of the growth cone to the surface of the biocompatible substrate (Hammarback and Letourneau, 1986). Neurites can be physically guided by fabricating three-dimensional microgrooves in substrate surfaces such as glass (Hirono et al., 1988), micromachined silicon chips (Kawana, 1996) and microelectrode arrays (Jimbo et al., 1993). Growth cones can detect and respond to chemical cues to enhance neuronal guidance. Neurotrophic factors such as laminin have been made into two-dimensional patterns onto various substrates to improve cell adhesion, stimulate neuron outgrowth and provide growth cone steering (Gundersen, 1987; Hammarback and Letourneau, 1986; Hammarback et al., 1988; and Buettner and Pittman, 1991).

Previous studies have focused on producing patterns on glass and other non-degradable substrates. However, no studies have been conducted with micropatterned biodegradable substrates for the purpose of tissue engineering to repair damaged peripheral nerves. For our project, the biodegradable polymers poly(DL-lactide) and poly(lactide-co-glycolide) are used to create biocompatible substrates. Unlike previous studies, both physical and chemical guidance mechanisms are utilized by the fabrication of grooves on the substrate surface as physical guidance and seeding Schwann cells into laminin lined grooves for chemical stimulation.

Experimental Approach

The micrometer-sized grooves are fabricated using a heated compression mold and an etched quartz die. Thin polymer films are made by compressing polymer pellets between glass slides. After cooling, these smooth films are removed from the glass and then compressed with a patterned quartz die of various groove width, spacing and depth.

The Schwann cells are cultured from the sciatic nerve of 2-3 week-old rats. After the cells are confluent, they are seeded onto microgrooved substrates. The neurons are collected from the dorsal root ganglia (DRG) from 1-3 day-old rats. The DRG are seeded on substrates with aligned Schwann cells.

Results and Discussion

Nerve cells recognize three-dimensional configurations and use these features to align and migrate along micropatterned structures. The degree of detection and response to the grooves depends on feature magnitude, feature density and cell-cell interactions as Clark (1987, 1990) indicated. As found in previous studies (Brunette, 1986; Hirono, 1988; and Clark, 1987, 1990), the deeper the groove, the more effective it is in aligning cells and the more closely the grooves are packed, the weaker the cell responses to the grooves (Clark, 1996). On narrow patterns, the neurons did not align with the grooves but on wider patterns, the neurons and Schwann cells are directionally guided by the grooves.

Our investigation has shown that chemical guidance and outgrowth of the neurons can be

influenced. When laminin is adsorbed to the substrate surface, cell adhesion is improved and rapid neurite outgrowth occurs. The neuron's outgrowth is directionally guided by a gradient of tropic factors secreted by the Schwann cells.

In Figure 1, the laminin coated PDLA substrate was seeded with Schwann cells and dissociated DRG. After 24 h, the neurons and Schwann cells were physically guided to align in the grooves and used chemical cues to produce rapid outgrowth and improved directional guidance.

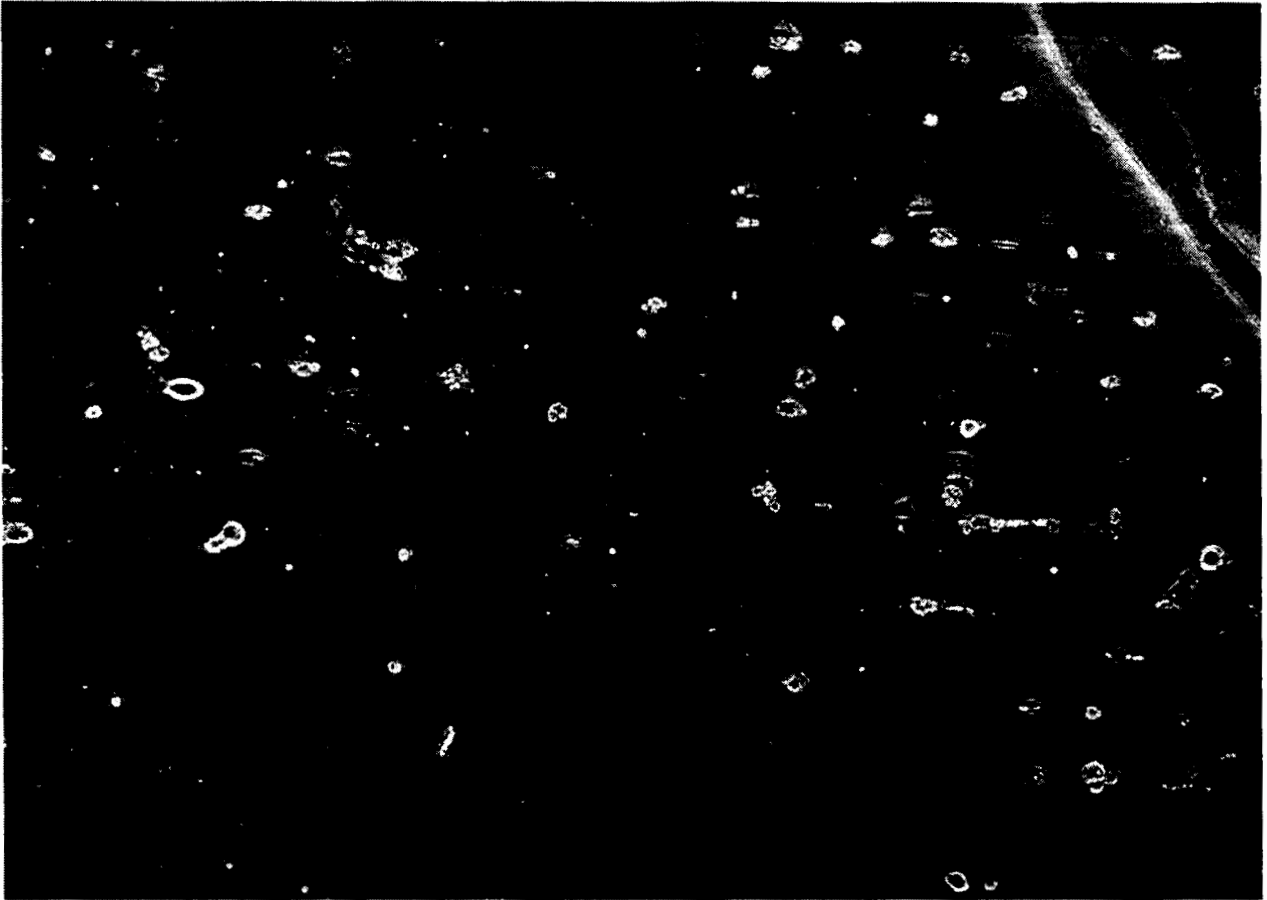


Figure 1. Cells seeded on a PDLA substrate for 1 day. View area is 1100 x 600 μm .

Summary

The ability to manipulate neurite outgrowth at the cellular level has the potential of enhancing peripheral nerve regeneration. The proper placement of successive environmental cues can direct and stimulate neurite outgrowth. Micrometer-sized grooves fabricated on biodegradable polymer films create boundaries enhancing physical guidance. Schwann cells seeded into the laminin-lined microgrooves provide chemical guidance by utilizing neurotropic and neurotrophic support for the regenerating neuron.

Acknowledgments

This project is funded by grants from the Carver Trust, the Institute for Physical Research and Technology, the National Science Foundation and the Department of Energy. Special thanks to J. Kenseth and M. Porter; A. Landin, T. Witt and H. Shanks; S. Jeftinija, J. Otaigbe, A. Ganepalli and G. Rutkowski.

References

- Brunette, D., *Exper. Cell Res.*, **164**, 11 (1986).
- Buettner, H. and R. Pittman, *Developmental Biol.*, **145**, 266 (1991).
- Clark, P., *Nanofabrication and Biosystems: Integrating Materials Science, Engineering and Biology*, Cambridge University Press, Cambridge, U.K., 1996.
- Clark, P., P. Connolly, A. Curtis, J. Dow and D. Wilkinson, *Development*, **99**, 439 (1987).
- Clark, P., P. Connolly, A. Curtis, J. Dow and D. Wilkinson, *Development*, **108**, 635 (1990).
- Medical Devices and Diagnostic Industry, pg. 3, August 1985.
- Gilmore, S. and T. Sims, *Neuroglia*, Oxford University Press, New York, 1995.
- Gundersen, R., *Developmental Biol.*, **121**, 423 (1987).
- Hammarback, J., J. McCarthy, S. Palm, L. Furcht and P. Letourneau, *Developmental Biology*, **126**, 29 (1988).
- Hammarback, J., and P. Letourneau, *Developmental Biol.*, **117**, 655 (1986).
- Hirono, T., K. Torimitsu, A. Kawana and J. Fukuda, *Brain Res.*, **446**, 195 (1988).
- Jimbo, Y., H. Robinson and A. Kawana, *IEEE Trans. Biomed. Eng.*, **40**, 8 (1993).
- Junqueira, L., J. Carneiro and A. Contopoulos, *Basic Histology*, 4th ed., pg. 162-195, Lange Medical Publications, Los Altos, CA, 1983.
- Kandel, E. and J. Schwartz, *Essentials of Neural Science and Behavior*, Appleton and Lange, Norwalk, Conn., 1985.
- Kawana, A., *Nanofabrication and Biosystems: Integrating Materials Science, Engineering and Biology*, Cambridge University Press, Cambridge, U.K., 1996.
- Tonge, D., J. Golding, M. Edbladh, M. Kroon, P. Ekstrom and A. Edstrom, *Experimental Neurol.*, **146**, 81 (1997).

Effects of Fluid-Induced Shear Stress and Simulated Aspects of Microgravity on Articular Cartilage Regeneration

David Wendt and Carole Heath, Department of Chemical Engineering, Iowa State University, Ames, IA 50011

ABSTRACT

Skeletal tissues in space-flown rats are adversely affected by the microgravity environment, a major concern for long-term human space habitation. To simulate aspects of microgravity, ground-based tissue engineering studies can be conducted in NASA-designed bioreactors called "rotating wall vessels". It is also known that tissue engineered cartilage can be grown under applied forces to stimulate production of the extracellular matrix. Therefore, modified rotating wall vessels were designed for this study to allow application of varying levels of shear stresses within the bioreactor. Chondrocytes isolated from equine articular cartilage were cultured on fibrous polyglycolic acid mesh for six weeks to assess the effects of shear stress on cartilage regeneration under conditions which simulate aspects of microgravity. Preliminary results indicate that cell/polymer constructs grown in these bioreactors are capable of producing both collagen and glycosaminoglycans, the extracellular matrix components found in native articular cartilage.

INTRODUCTION

Tissue engineers throughout the world are currently investigating virtually every tissue in the human body, but perhaps the most promising tissue to be engineered in the near-term is that of articular cartilage. When the cartilage that covers the ends of bones in diarthrodial joints becomes damaged, either through traumatic injury or gradual degradation, the unique mechanical properties it possesses are compromised. Because this tissue has a very limited ability to repair itself, further degradation may occur, often resulting in osteoarthritis. Traditionally, treatments for this ailment have been unsatisfactory, ranging from pain medication, grafts, to total joint replacement. With approximately 35 million Americans suffering from osteoarthritis, and no known cure, a successfully engineered cartilage implant would revolutionize orthopaedic medicine. Yet, much is still to be known before a fully functioning tissue is to be grown *in vitro*.

Since cartilage is a very dynamic tissue, subject to many forces *in vivo*, it is essential to study how these forces affect developing tissue. For over two decades, researchers have investigated the effects of mechanical stimuli on articular cartilage. Yet, only recently have researchers been successful at exploiting mechanical stresses to stimulate tissue-like extracellular matrices. Since the predominant force that articular cartilage is subjected to is compression, virtually all of these studies have concentrated on applying hydrostatic or hydrodynamic compressive loads during regeneration [1-3]. Yet, compression alone neglects to incorporate the importance of fluid flow as found *in vivo*. Only recently have researchers recognized the importance of fluid flow and shear stress on tissue engineering articular cartilage [4-11].

Although not commonly investigated by tissue engineers, the influence of gravity upon cellular functions is of great interest to NASA, since many of these effects may be limiting factors for long-term space habitation. The effects of a microgravity environment on cartilage tissue are significantly altered in space-flown rats [12-14]. Although the mechanisms by which microgravity

affects extracellular matrix production and organization are still unknown, alterations of fluid-induced shear on the cell surface, fluid mixing, and solute mass transfer all likely factors. Due to the complexities, costs, and limited accessibility for space-flown experiments, ground-based studies need to be conducted to unveil these mechanisms and provide a means to counteract adverse effects of microgravity.

Developed by NASA, the “rotating wall vessel” (RWV) is a novel bioreactor for ground-based experiments that attempts to simulate aspects of a microgravity environment. A unique RWV was designed and manufactured for the present study to allow for the application of varying levels of fluid-induced shear. It is therefore possible to examine the effect of applying fluid-induced shear stress on cartilage tissue in an environment that simulates aspects of microgravity.

MATERIALS AND METHODS

Chondrocytes (cartilage cells) were isolated from articular cartilage obtained from the stifle joints of foals by collagenase digestion [15]. Cells were seeded onto squares (1 cm x 1 cm x 0.5 cm) of a non-woven mesh of polyglycolic acid in a spinner flask for one week before transfer to the RWV[10].

Based on the design of the clinostat, the traditional RWV consists of two horizontal concentric cylinders rotating at the same angular velocity (Ω_1). When the annular space is completely filled with culture media under steady-state conditions, solid-body rotation of the fluid occurs. The modified rotating wall vessel designed for this investigation is depicted in Figures 1 and 2. Four pairs of needles are mounted coaxial to the vessel walls, onto which cell-polymer constructs are attached by simply threading them through the polymer mesh. As the vessel walls and fluid rotate as a solid body, the fluid flowing over the constructs induces a shear stress. By rotating the set of needles independently from the vessel walls, hence at a different angular velocity (Ω_2), the velocity at which the fluid flows over the constructs can be changed, altering the level of shear stress induced.

The modified rotating wall vessel is designed to operate under two distinct regimes simulating some aspects of microgravity. The first, simulating free-fall conditions, can be achieved by eliminating the needles and allowing the cell-polymer constructs to simply float freely within the media (Figure 3a). This is simulated when the vessel walls, and hence the fluid, are rotating at a rate such that the drag force (F_d) on the construct balances the centrifugal (F_c) and net gravitational forces (F_g). Since these vectors sum to zero there is no net force on the construct, it remains at a stationary point within the reactor, in a state of freefall within the liquid [4]. The second mode of simulated microgravity (Figure 3b), the “orbiting regime”, is achieved with the rotation of the needle-construct assembly. Although the construct is constantly subjected to the Earth’s gravitational pull as it rotates, the net gravitational vector over a complete revolution is zero. At every point in the construct’s path the vector points down (F_g), but 180° from this point where the construct is flipped 180° from the reference, the gravitational vector (F_g') is equal but opposite to that from its original position. Once again, since the construct is subjected to unit gravity, the manner in which aspects of microgravity are simulated must be looked at not discretely, but over a time frame of one revolution. Therefore, only gravitational responses that occur over perhaps a 2-3-second time frame (depending on the rotational rate) would be expected to be affected [16].

After five weeks of culture in the RWV, tissue samples were removed and analyzed for extracellular matrix components and cell density. Total collagen content was determined by quantifying the amount of hydroxyproline present in the tissue [17]. Measurement of the sulfated glycosaminoglycans (SGAG) content of the tissue was determined using a dimethylmethylene blue assay on papain-digested samples [18]. The number of cells in the tissue sample was calculated by fluorometrically measuring the amount of DNA bound to Hoechst 33258 dye [19].

Current and future experiments will also be qualitatively examined by routine H and E staining and alcian blue staining for SGAG. Because the total collagen assay does not differentiate between collagen types, anti-collagen antibody staining will be performed to qualitatively examine the relative amounts of type I and type II produced. In addition, moduli to assess the mechanical properties of the engineered tissue will also be measured utilizing a dynamic mechanical analyzer. To complement the SGAG assay, aggregation of proteoglycans will also be examined.

RESULTS

Because chondrocytes may concentrate upon matrix production rather than proliferation when subjected to stresses, it appears to be essential to seed the polymer with an initial high cell density [9]. Therefore, it was important to investigate whether chondrocytes with serial passages (multiple cell divisions) would produce extracellular matrix as well as primary cells. After five weeks of culture in the freefall regime, samples were removed from the rotating wall vessels and assayed. Both groups resulted in similar cell densities, both slightly above that of native cartilage (Table 1). The primary chondrocyte samples generated slightly more total collagen than the serial-passaged cells, yet only 2-3% of that in native articular cartilage. In contrast, SGAG levels reached those found in native cartilage for samples seeded with primary chondrocytes; a significant improvement over cells with serial passages.

Next, using primary chondrocytes only, the extremes of the RWV's operating conditions were tested for five weeks. Operating under the orbiting regime, rotating the needle/cell-polymer assembly at the same rate as the vessel walls, hence everything rotating as a solid body, an approximate zero-shear environment was tested. Condition two also operated in the orbiting regime, but with the needle/cell-polymer assembly rotated near the upper operating extreme, generating a fluid-induced shear stress at the tissue surface of approximately 1.7 dynes/cm^2 . The third condition tested once again was the freefall regime. Results are also shown in Table 1.

After several days of the high shear condition, the cell-polymer construct deteriorated and fell apart. Because polyglycolic acid fully degrades within four weeks, significant extracellular matrix must be produced to assist in providing a structure for the tissue as it continues to develop. Apparently, in this short time period of several days, not enough tissue was manufactured to maintain structural integrity of the delicate cell-polymer construct and enable it to withstand the induced high shear. It may be necessary to begin with lower levels of shear and gradually step up to higher magnitudes.

As experienced in previous conditions, both treatments resulted in similar but very poor collagen synthesis. Although not calculated, the constructs in freefall are subjected to fluid-induced shear stress as they fall through the medium. This may explain the increase in glycosaminoglycans detected in these samples as compared to those samples subjected to negligible shear. However, in

addition to shear levels, the aspects of microgravity simulated in these two treatments are different. Therefore, it is not possible to attribute the difference in extracellular GAG exclusively to the shear variable.

FUTURE WORK

Ongoing research continues to seek to discover what effects fluid-induced shear and simulated aspects of microgravity have on articular cartilage regeneration. The unique reactor vessel used for this research provides exciting promise for the discovery not only of their individual effects, but their interactions. Future experiments will concentrate on the orbiting regime. By manipulating the angular velocity of the vessel walls, it will be possible to vary the shear effects; while manipulating the angular velocity of the needles allows for examination of aspects of simulated microgravity.

ACKNOWLEDGMENTS

This work was supported by funding from the National Aeronautic and Space Administration. Special thanks to Axel Sondhof from the Iowa State Veterinary College for assistance in obtaining cartilage tissue.

REFERENCES

1. Parkkinen, J.J., *et al.*, *Effects of cyclic hydrostatic pressure on proteoglycan synthesis in cultured chondrocytes and articular cartilage explants*. Arch. Biochem. Biophys., 1993. **300**: 458-465.
2. Heath, C.A. and S.R. Magari, *Mini-review: Mechanical factors affecting cartilage regeneration in vitro*. Biotechnol. Bioeng., 1994. **46**: 1-8.
3. Carver, S.E. and C.A. Heath, *Increasing extracellular matrix production in regeneration cartilage with intermittent physiological pressure*. Biotechnol. Bioeng, 1999. **62**: 166-174.
4. Freed, L.E., G. Vunjak-Novakovic, and R. Langer, *Cultivation of cell-polymer cartilage implants in bioreactors*. J. Cell. Biochem., 1993. **51**: 257-64.
5. Freed, L.E., *et al.*, *Composition of cell-polymer cartilage implants*. Biotechnol. Bioeng., 1994. **43**: 605-614.
6. Freed, L.E., *et al.*, *Kinetics of chondrocyte growth in cell-polymer implants*. Biotechnol. Bioeng., 1994. **43**: 594-604.
7. Saini, S., T.M. Wick, and G.I.o. Technology. *Bioreactor for development of tissue engineered cartilage constructs*. in *ASME 1999 Summer Bioengineering Conference*. 1999. Big Sky, Montana.
8. Seliktar, D., *et al.*, *Application of shear flow stress to chondrocytes*, . 1998: PCT Int. Appl.
9. Vunjak-Novakovic, G., *et al.*, *Effects of mixing on the composition and morphology of tissue-engineered cartilage*. AICHE J., 1996. **42**: 850-860.
10. Vunjak-Novakovic, G., *et al.*, *Dynamic cell seeding of polymer scaffolds for cartilage*

tissue engineering. Biotechnol. Prog., 1998. **14**: 193-202.

11. Vunjak-Novakovic, G., *et al.*, *Bioreactor cultivation conditions modulate the composition and mechanical properties of tissue-engineered cartilage*. J. Orthoped. Res., 1999. **17**: 130-138.
12. Matthews, J.L., *Quantitative analysis of selected bone parameters: Mineralization in the long bones.*, in *NASA TM-81289, Final Reports of U.S. Rat experiments on the Soviet Satellite Cosmos 1129.*, M.R. Heinrich and K.A. Souza, Editors. 1981, NASA: Moffet Field, CA, 199-228.
13. Duke, J., G. Durnova, and D. Montufar-Solis, *Histomorphometric and electron microscopic analyses of tibial epiphyseal plates from Cosmos 1887 rats*. FASEB J., 1990. **4**: 41-46.
14. Montufar-Solis, D., J. Duke, and G. Durnova, *Spaceflight and age affect tibial epiphyseal growth plate histomorphometry*. J. Appl. Physiol., 1992. **73**: 195-255.
15. Nixon, A.J., G. Lust, and M. Vernier-Singer, *Isolation, propagation, and cryopreservation of equine articular chondrocytes*. Am. J. Vet. Res., 1992. **53**: 2364-2370.
16. Akins, R.E., *et al.*, *Neonatal rat heart cells cultured in simulated microgravity*. In Vitro Cell. Dev. Biol.-Animal, 1997. **33**: 337-343.
17. Woessner, J.F., *The determination of hydroxyproline in tissue and protein samples containing small proportions of this imino acid*. Arch. Biochem. Biophys., 1961. **93**: 440-447.
18. Farndale, R.W., D.J. Buttle, and A.J. Barrett, *Improved quantitation and discrimination of sulphated glycosaminoglycans by use of dimethylmethylene blue*. Biochim. Biophys. Acta, 1986. **883**: 173-177.
19. Kim, Y.J., *et al.*, *Fluorometric assay of DNA in cartilage explants using Hoechst 33258*. Anal. Biochem., 1988. **174**: 168-176.

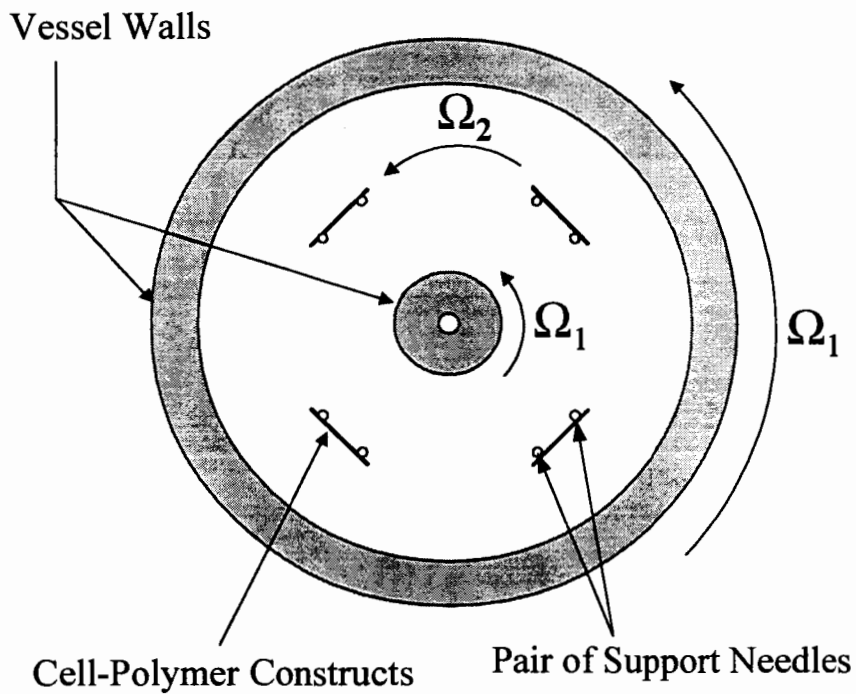


Figure 1. End view of the modified rotating wall vessel.

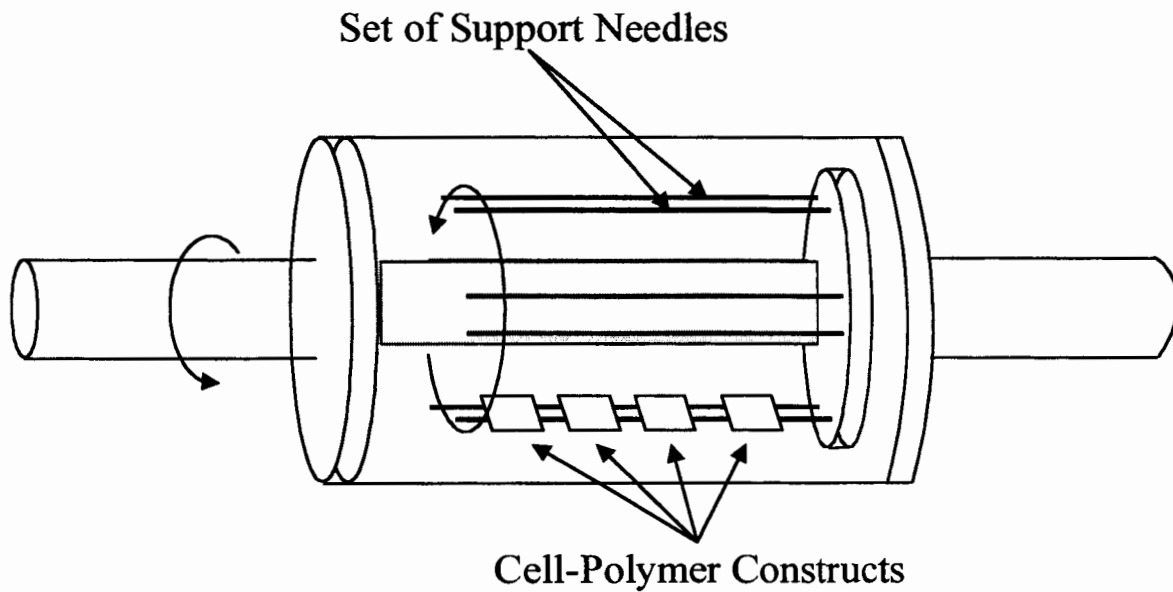


Figure 2. Front view of the modified rotating wall vessel.

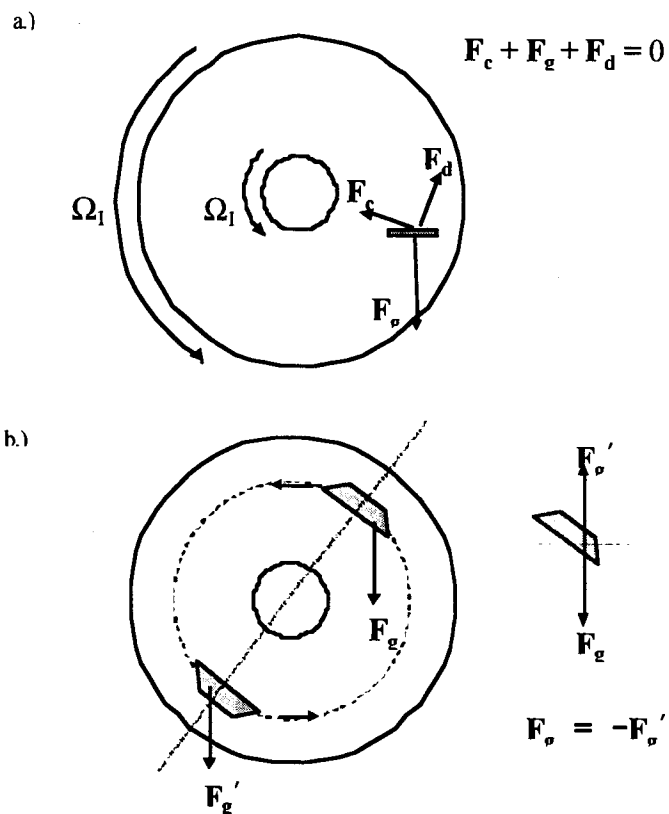


Figure 3. Modes of RWV operation to simulate aspects of a microgravity environment.
 a) Construct in state of freefall. b) Construct in orbiting regime.

Table 1. Six-week assay results for articular cartilage engineered in modified RWV's

Condition examined	GAG, $\mu\text{g/g}$ (dry)	Total collagen, mg/g (wet)	Cell number $\times 10^{-7}$, cells/g (wet)
Serial passages ¹	8,300	8.3	8.7
Primary cells ¹	46,000	4.6	9.4
Freefall ²	47,000	4.2	50
No shear ²	28,000	3.9	7.5

¹ Freefall regime
² Primary cells

Thrombolysis in a Rabbit Stroke Model Using Liposomal-Encapsulated Streptokinase

Kent Leach¹, Edgar O'Rear¹, Yiwei Miao², Art Johnson², and Eugene Patterson³

**¹School of Chemical Engineering and Materials Science
University of Oklahoma, Norman, OK 73019**

²College of Medicine, Texas A&M University, College Station, TX 77843

³University of Oklahoma Health Sciences Center, Oklahoma City, OK 73104

ABSTRACT

Plasminogen activators have been used for years to treat thrombotic crises. While some have focused on the development of more fibrin-specific thrombolytics, we have chosen to examine alternative methods of delivering thrombolytic proteins to clots. Specifically, others and we have shown that plasminogen activators are more effective when encapsulated in liposomes than when infused as free proteins. Studies using streptokinase, tissue-type plasminogen activator, and urokinase have focused on the effect of encapsulation in models of myocardial infarction, and each has shown that encapsulation enhanced thrombolysis. In this study, we have explored the potential benefits of encapsulating streptokinase (SK) for the treatment of strokes by comparing the effects of free intravenous SK and liposomal-encapsulated SK (LESK).

Following simulation of a stroke in a rabbit model, we infused comparable doses of either LESK or SK to determine the effect of each on reperfusion. LESK showed a significantly improved clot dissolving time over free SK. On average, LESK dissolved blood clots in one-fourth the time of free streptokinase [19.3 ± 12.1 minutes versus 74.3 ± 41.4 minutes, respectively]. Thus, the thrombolytic efficacy of SK is improved by encapsulating the agent in liposomes for this experimental rabbit model, presumably by preventing premature inactivation of SK prior to LESK arrival and rupture at the clot.

INTRODUCTION

Cardiovascular disease has been and continues to be the number one cause of death in the United States. Considered alone, stroke stands as the third leading cause of death. The most recent statistics show that someone in the United States suffers from stroke every 53 seconds; someone dies every 3.3 minutes (1).

A vascular occlusion, or blockage of blood flow, is the result of a two-phase process. The long-term phase is the accumulation of atherosclerotic plaques composed of cholesterol and lipids on the innermost layer of the walls of blood vessels. The slow build-up of plaque results in a narrowing of the vessel for blood flow. The acute phase of an occlusion is the lodging of a clot, a thrombus, in the vessel that will then occlude flow. In order to restore the flow of life-

sustaining oxygen and nutrients to organs and tissues, the clot must be removed as quickly as possible.

Treatment methods for stroke have vastly improved in the last decade. We are no longer helpless in the retaliation against the "brain attack". Through the use of plasminogen activators such as tissue-type plasminogen activator (tPA), prourokinase, urokinase, and streptokinase (SK), we have given hope to the nearly 600,000 annual stroke victims and 1.1 million annual heart attack victims. Plasminogen activators switch on the body's system for dissolving harmful occlusions by activating the appropriate enzymes. Initially the activators work in different manners, but all of the drugs cause the conversion of plasminogen to plasmin. Plasmin, in turn, degrades the occlusive clot and promotes the restoration of blood flow. Based on the NINDS rt-PA study (2), t-PA became the first activator to receive FDA approval for treatment of strokes in 1997.

Plasminogen activators have been used for two decades to dissolve blood clots, but each one has benefits and drawbacks (3). Plasminogen activators have a short half-life (5-20 minutes) and are rapidly cleared from the system by the reticuloendothelial system (RES). The thrombolytic agents undergo rapid deactivation once in the body due to the extreme change in environmental conditions such as temperature and pH. The rapid clearance coupled with deactivation necessitates an excessively high dosage of the drug in order to maintain dosages in the therapeutic window. Activators such as streptokinase and urokinase are derived from bacterial cultures. Upon infusion of these proteins for treatment, the resulting antibodies enhance the removal of the material from the system. Lastly, the clot-busting drugs lack complete fibrin specificity. The absence of specificity results in the dissolution of both harmful and necessary blood clots, which can in turn result in uncontrolled hemorrhaging.

In an effort to improve the clot dissolution process, new delivery techniques of the thrombolytic drugs have been considered. Previous studies have shown that liposomal-encapsulated plasminogen activators can be more effective than freely infused plasminogen activators. Studies using t-PA (4), streptokinase (5,6,7), and urokinase (8) have all shown enhanced thrombolysis when encapsulated. However, the previous studies have focused on the effect of encapsulation on myocardial infarction. In this study, we have attempted to examine the benefits of liposomal-encapsulated streptokinase (LESK) in stroke treatment.

MATERIALS AND METHODS

Preparation of Liposomes

Large unilamellar phospholipid vesicles were prepared through the detergent removal method. Briefly, POPC (160 mg; 1-palmitoyl-2-oleoyl-sn-glycero-3-phosphocholine) was dried under vacuum, together with 0.05 μ Ci of 1,2-di[1-¹⁴C]-oleoyl-L-3-phosphatidylcholine added for tracing purposes, and then resuspended in 2 ml of 1 M OG (n-octyl- β -D-glucopyranoside) in HBS [HBS:50 mM HEPES (pH 7.5), 100 mM NaCl] at 37 °C with occasional mixing.

Streptokinase (80,000 IU) was dissolved in the resuspended POPC, and then OG was removed by dialysis against 4L of HBS (6 changes, 12 hr/change) at 4°C. The resulting liposome-encapsulated streptokinase (LESK) was purified from unencapsulated SK by gel filtration in HBS at 4°C through a Sepharose CL-6B column (0.7 cm i.d. x 50 cm). LESK eluted in the void volume, as evidenced by the coincident detection of protein by absorbance at 280 nm

and of phospholipid by radioactivity in the 1.2-ml fractions. SK content in the pooled LESK peak fractions was quantified by commercially available activity kits both in the presence and absence of OG (100 mM final concentration). Encapsulation efficiency was determined to be 30%.

Animal Tests

The present study examined the performance of the liposome formulation *in vivo* with the aid of a rabbit model of stroke. Animals were treated under procedures that were examined and approved by an institutional review panel of the University of Oklahoma Health Sciences Center, as well as the University of Oklahoma. New Zealand white rabbits of either sex were anesthetized with inhaled halothan (5%). Cardiac activity was monitored by ECG. The right carotid artery was isolated, as was the left jugular vein. The jugular vein was cannulated with PE-90 tubing, which was connected to a 20 cc syringe. Right carotid artery flow was measured with a 20-MHz pulsed Doppler or electromagnetic flow probe. Arterial thrombosis was initiated by the injection of 100 units of thrombin and 0.1 ml whole blood into a 5-10-mm long segment of proximal and distal right carotid artery. After 10 ensnared minutes, the proximal ligature was released; after an additional 5 minutes, the distal ligature also was released. In some experiments, as many as three injections were necessary to form an occlusive thrombus. The thrombus was allowed to mature for 30 minutes prior to administration of the drug formulation.

The relative dosages of the two thrombolytic preparations were identical. A dosage of 6,000 units/kg was determined as adequate to produce thrombolysis. The preparation was dispersed in normal saline to a total volume of 20 cc. An initial bolus of 20% (4 ml) preceded a constant intravenous infusion of the remaining 80% over a 30 minute time period. The infusion was maintained at a steady rate with an infusion pump. Animals were observed for 2 hours following the initiation of infusion. Reperfusion was documented by 1) a resolution of electrocardiographic changes induced by ischemia, and 2) recovery of right carotid arterial flow. At the conclusion of the experiment, the artery was dissected, and thrombus mass was determined gravimetrically.

RESULTS AND DISCUSSION

The thrombolytic activity of LESK was directly compared with free streptokinase. The average time required for reperfusion with SK alone was 74 ± 41 minutes (mean \pm SD). In

	Saline (n=6)	Free Streptokinase (n=6)	Liposomal SK Encapsulation (n=7)
Time to Reperfusion	—	74 ± 41 min.	19 ± 12 min.
Carotid Artery Blood Flow (% of pre-drug flow) at:			
0 minutes	0 ± 1	0 ± 1	0 ± 1
30 minutes	0 ± 1	8 ± 9	47 ± 19
60 minutes	0 ± 1	17 ± 12	74 ± 26

decisive contrast to the free SK values, LESK greatly reduced thrombolysis times to 19 ± 12 minutes, with some observed reperfusions occurring as quickly as 8 minutes. With the assumptions of normal distributions and of equivalent sample populations, this is a statistically significant difference with $p < 0.0062$ according to the Student's *t*-test for the difference between means. Even though the return of flow is not significant at $p < 0.05$ ($p < 0.0791$), the analysis suggests it is a significant factor in the comparison of these two plasminogen activator preparations.

The results of these experiments show that encapsulation of streptokinase can be beneficial in thrombolysis. The liposome acts as a shield that conceals the agent from the body, thereby preventing the premature deactivation and removal of the material. The small size of the vesicles, approximately 300 nm, enables the liposomes to avoid detection by the RES. The liposomes are then allowed to circulate freely in the circulatory system until arriving at the clot site. Additionally, liposomes do not elicit an immune response as does free streptokinase.

Although the mechanism of thrombolysis is relatively well characterized, the method of clot dissolution using the encapsulated plasminogen activator is unknown. Several theories have been proposed for the release of the drug from the liposome. It has been suggested that shear forces cause the fragile biological vehicle to rupture when the vehicle reaches the occlusion. Another proposed theory of release involves the removal of the phospholipids from the vesicle bilayer upon infusion into the circulatory system due to the concentration gradient of lipid proteins. The phospholipid removal compromises the integrity of the vesicle and causes the release of its contents. Continuing studies in our laboratory and others are working to determine this mechanism.

CONCLUSIONS

The thrombolytic efficacy of streptokinase was improved by liposomal-encapsulation for this rabbit model of stroke. As illustrated in the table, two primary benefits resulted from the use of encapsulated streptokinase in treatment. The time required to achieve reperfusion was drastically reduced with the aid of the encapsulated agent. Also, a substantially greater percentage of carotid arterial flow was restored in a shorter time with LESK than free SK alone. We presume this improvement resulted from the prevention of both premature deactivation of the plasminogen activator and rapid clearing of the thrombolytic agent.

REFERENCES

1. American Heart Association. 1999 Heart and Stroke Statistical Update. Dallas, Tex.: American Heart Association, 1998.
2. The National Institute of Neurological Disorders and Stroke rt-PA Stroke Study Group, Tissue Plasminogen Activator for Acute Ischemic Stroke, *New England Journal of Medicine*, 333:1581-1587, 1995.
3. Robbins KC, Barlow GH, Nguyen G, Samama MM, Comparison of Plasminogen Activators, *Seminars in Thrombosis and Hemostasis*, 13:131-138, 1987.
4. Heeremans JLM., Prevost R, Bekkers MEA, Los P, Emels JJ, Kluft C, Crommelin DJA, Thrombolytic Treatment with Tissue-type Plasminogen Activator (t-PA) Containing Liposomes in Rabbits: a Comparison with Free t-PA, *Thrombosis and Haemostasis*, 73:488-494, 1995.
5. Perkins WR, Vaughan DE, Plavin SR, Daley WL, Rauch J, Lee L, Janoff AS, Streptokinase Entrapment in Interdigitation-Fusion Liposomes Improves Thrombolysis in an Experimental Rabbit Model, *Thrombosis and Haemostasis*, 77:1174-1178, 1997.
6. Nguyen PD, O'Rear EA, Johnson AE, Patterson E, Whitsett TL, Bhakta R, Accelerated Thrombolysis and Reperfusion in a Canine Model of Myocardial Infarction by Liposomal Encapsulation of Streptokinase, *Circulation Research*, 66:875-878, 1990.
7. Nguyen PD, O'Rear EA, Johnson AE, Lu R, Fung BM, Thrombolysis Using Liposomal-Encapsulated Streptokinase: An In Vitro Study, *Proceedings of the Society of Experimental Biology and Medicine*, 192:261-269, 1989.
8. Li ZL, Zhang NZ, Nie YH, Accelerated Thrombolysis by Liposomal-Encapsulated Urokinase in a Canine Model of Acute Myocardial Infarction, *Chung Hua I Hsueh Tsa Chih*, 74:338-340, 1994.

Shear Stress Modulates Platelet Aggregation at a Site of Vascular Injury

Elizabeth Y. Nguyen, Laura M. Worthen and Matthias U. Nollert

School of Chemical Engineering and Materials Science
University of Oklahoma
Norman, Oklahoma 73019

Abstract

Platelet-endothelium interactions were studied in an *in vitro* parallel plate flow system that mimicked the fluid mechanical environment found in the blood vessels. The number of platelets from whole blood that attached to an injured endothelial cell monolayer was quantified by fluorescence video microscopy. At a venous shear rate (100 s^{-1}), platelets adhered abundantly, while a significantly smaller number of platelets attached under arterial conditions (1000 s^{-1}). Platelet adhesion at the high shear rate was increased by metabolically inactivating the endothelial cells with the combination of sodium azide and deoxyglucose. In addition, inhibition of endothelial derived nitric oxide production with L-NAME or prostacyclin production with aspirin also resulted in increased platelet adherence at 1000 s^{-1} . These results suggest that platelet thrombus formation at a site of injury is modulated by endothelial derived prostacyclin and nitric oxide at high shear stress but not at low shear stress.

Introduction

Platelets play a central role in normal hemostasis and in the development of thrombosis. Mural thrombosis can be beneficial if it occurs in response to an injury of the endothelium but can be detrimental if occurs on an atherosclerotic lesion or on a prosthetic device. The mechanism involved in platelet thrombus formation has still not been satisfactorily resolved, and a better knowledge of platelet processes may be beneficial in understanding the development of vascular diseases and bleeding disorders. A study of platelet-endothelium interactions under physiological flow conditions addresses the relative contribution of fluid mechanical shear stress on the initiation of platelet adherence and the progression of platelet thrombus formation. Since both thrombosis and clinical bleeding are important medical issues with high rates of mortality, this enhanced knowledge of platelet biology may result in further insights into improved therapies for vascular disease.

In this study, endothelial cells will be exposed to shear stress to simulate the mechanical environment typical of the vascular system *in vivo*. Shear stress may modulate endothelial cell calcium concentration^{1; 7; 12} and can enhance the release of vasoactive substances, including arachidonic acid metabolites^{2; 9}, nitric oxide (NO)^{3; 10; 14}, tissue type plasminogen activator⁴, and von Willebrand factor (vWF)⁶. Some of these released substances can inhibit platelet adhesion and aggregation, while others can promote thrombus formation. This study will examine the interaction between flowing platelets and an injured endothelial cell monolayer to determine the overall effect of shear stress on platelet adhesion and aggregation.

Materials and Methods

Blood donors and platelet labeling. Whole blood was collected by venipuncture. All donors gave informed consent. The informed consent form and procedure were approved by the University of Oklahoma Institutional Review Board. None of the donors had taken any medication, including aspirin, in the preceding 14 days. 1mg of fluorescein isothiocyanate (FITC)-conjugated monoclonal antibody Tab (gift from Dr. Rodger McEver, Oklahoma Medical Research Foundation, Oklahoma City, OK) was added to each 10mL of blood, resulting in a final Tab-FITC IgG concentration of 0.76mg/mL.

Collagen-coated glass slides. Glass slides measuring 50 x 24 mm were washed five times in deionized water, then another time with 100% high grade methanol. Half of each slide was covered with 200 μ L collagen (Type I calfskin; Sigma), which was prepared at 0.8mg/mL in acidic acid.

Monolayer injury model. The endothelial cells [bovine aortic endothelial cells (BAECs) or human umbilical vein endothelial cells (HUVECs)] were cultured under static conditions at 37 °C using established methods. The bovine cells were maintained in minimum essential medium (MEM) supplemented with 10% fetal bovine serum (FBS), 1% L-glutamine, and 1% penicillin-streptomycin. HUVECs were isolated from the umbilical cord vein by collagenase digestion and cultured using medium M199 supplemented with 20%FBS, 1% L-glutamine, and 2% penicillin-streptomycin. Primary HUVEC were used in experiments.

Endothelial cells were grown to confluence (typically for 5 days) on 50 x 24 mm glass slides. A precision razor blade was used to incise a micro-injury on the endothelial cell monolayer. The micro-injury was perpendicular to blood flow, and the width of the injury varied across the monolayer from 20 to 100 μ m. The injury was produced with a small amount of applied pressure to minimize damage to the subendothelial matrix beneath the endothelial cell monolayer.

Imaging system. Epifluorescence video-microscopy was used to obtain real-time images of platelet adhesion and aggregation at the defined micro-injury. The video microscopy system consisted of an inverted Diaphot 300 microscope (Nikon) with a 40X fluorite objective. To minimize photobleaching, the adherent platelets were only illuminated for approximately 5 seconds every 30 seconds during which time a single video frame was captured and digitized.

Data analysis. A field of view was chosen for analysis such that both the upstream and downstream edges of the injury were perpendicular to the direction of flow and approximately 60 μ m apart. The number of adherent platelets and the percent coverage of the injured section were quantified by ISEE computer software (Inovision) running on a Silicon Graphics workstation.

Treatment of cells. In certain experiments, the endothelial cells were pretreated for 20 minutes with a mixture of 50mM 2-deoxyglucose (DOG) and 0.06% NaN₃ in HBSS. In

other experiments, endothelial cells were treated with L-nitro-amino-arginine methyl ester (L-NAME), aspirin or with both. The cells were pretreated with 300mM of L-NAME 20 minutes prior to the experiments and the same concentration of L-NAME was also added to the whole blood. Cells were pretreated with 100mM aspirin for 24 hours. In all cases, the cells were washed three times with HBSS and medium without additives was added to the cells just prior to the start of experiments.

Results

Platelet adhesion and aggregation on injured endothelium. Under venous (100 s^{-1}) conditions, platelets attached on the exposed subendothelium to obtain almost complete coverage of the injured section (*Figs. 1 & 2*). A significantly smaller ($p < 0.005$) number of platelets attached to the subendothelial matrix at the arterial shear rate (1000 s^{-1}) (*Figs. 1 & 2*). A very small number of platelets (typically less than 0.1% of the platelet surface density at the injury) attached to intact endothelial cells, either upstream or downstream of the injury.

NaN_3 and DOG were used to treat the bovine endothelial cells in order to assess the impact of endothelial cell metabolic activity on platelet adhesion and aggregation. Under venous conditions (100 s^{-1}), platelet attachment was abundant on injured endothelium, regardless of treatment with NaN_3 and DOG (*Fig. 2*). Under arterial conditions (1000 s^{-1}), a significantly greater ($p < 0.010$) number of platelets attached to injured endothelium that had been metabolically inactivated (*Fig. 2*).

Role of prostacyclin and NO. We investigated the possible role of endothelial derived prostacyclin and NO in inhibiting platelet attachment and aggregation. Endothelial cell monolayers were incubated with either the nitric oxide synthase inhibitor L-NAME, or the prostacyclin inhibitor aspirin, or both before the monolayers were injured and exposed to blood flow. As illustrated in Figure 3, incubation with either inhibitor caused a significant ($p < 0.05$) increase in the number of adherent platelets. The combination of L-NAME and aspirin caused a further increase in the number of adherent platelets.

Discussion

The number of platelets from whole blood that adhered and aggregated at a site of injury was quantified, and the percent coverage of the injury by platelets was determined. Under venous conditions (100 s^{-1}), high levels of platelet attachment occurred onto exposed subendothelium in contrast to a much smaller number of platelets that attached under arterial conditions (1000 s^{-1}). Metabolic inhibition of the endothelium by NaN_3 and DOG enhanced platelet accumulation at the high shear rate, suggesting that endothelial cells play a critical role in modulating platelet adhesion at a site of injury.

The mechanism for the reduced platelet adhesion at high shear rate was investigated by metabolically inhibiting the endothelial cells with NaN_3 and DOG. These compounds are inhibitors of the electron transport system which prevent endothelial cells from synthesizing or releasing biologically-active substances. Our results show that pretreatment of the endothelial cells with these metabolic inhibitors increased platelet adhesion to the injury at the arterial shear rate (1000 s^{-1}), which suggest that viable endothelial cells may have released anti-thrombogenic substances to hinder platelets from attaching. This is consistent with the observation that the release of PGI_2 and NO ^{8, 11, 13} is enhanced at high shear. In

FIGURE 1

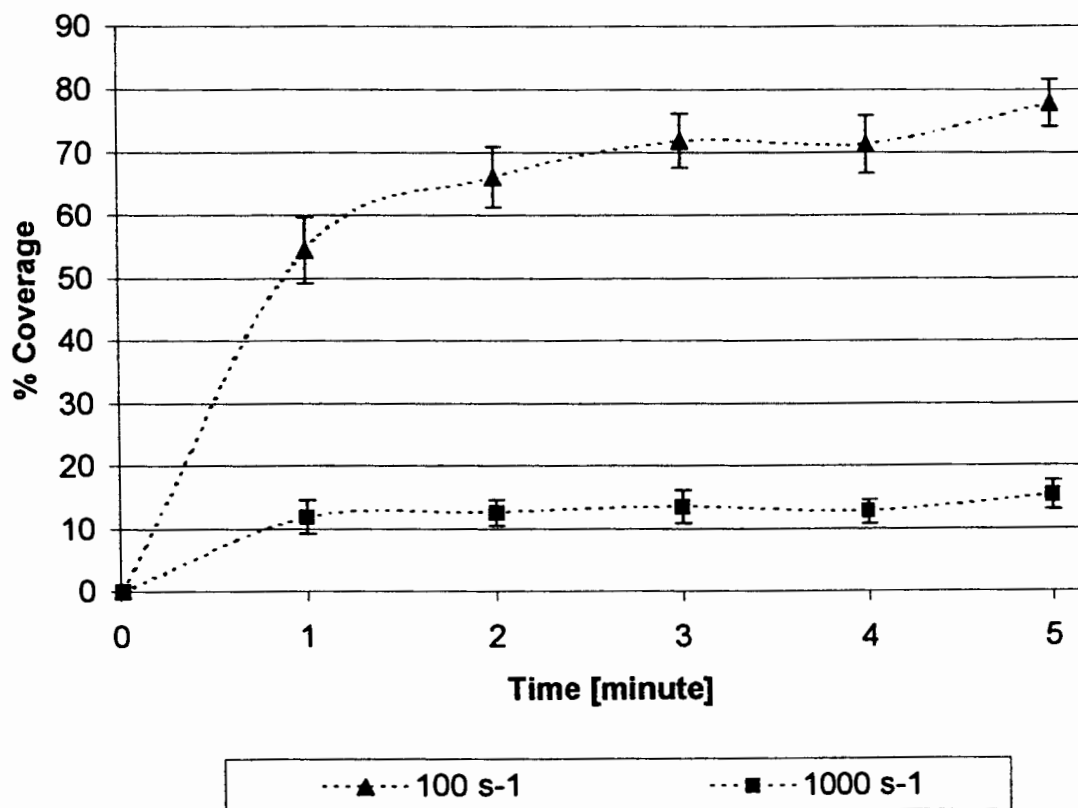


Figure 1: Effect of shear rate on platelet adhesion and aggregation on injured endothelium. For each experiment, duplicate slides were analyzed. Percent coverage of the injury site by platelets. $n = 18$ at 100 s^{-1} and $n = 15$ at 1000 s^{-1} .

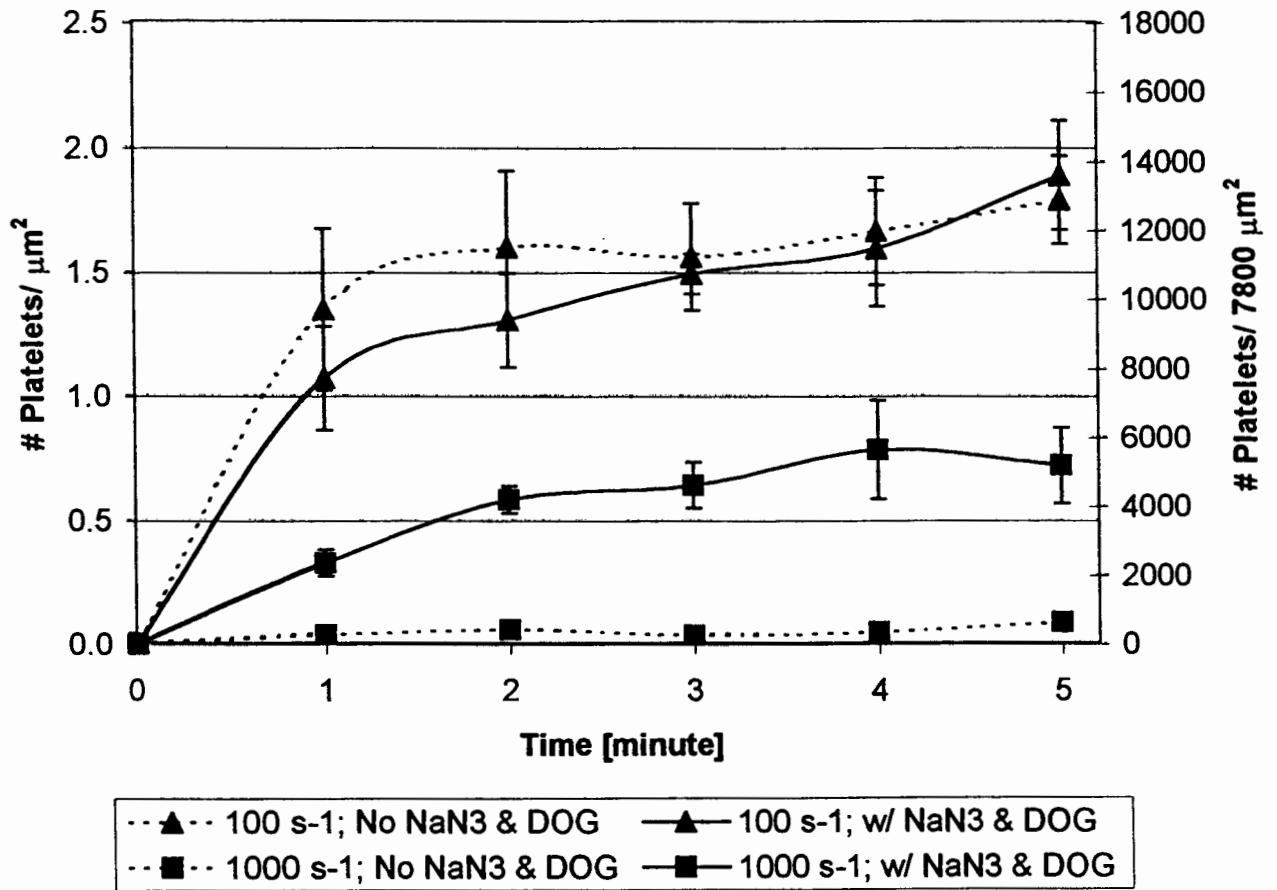


Figure 2: The effect of adding the metabolic inhibitors, NaN₃ or DOG on the accumulation of platelets at a site of injury to an endothelial cell monolayer.

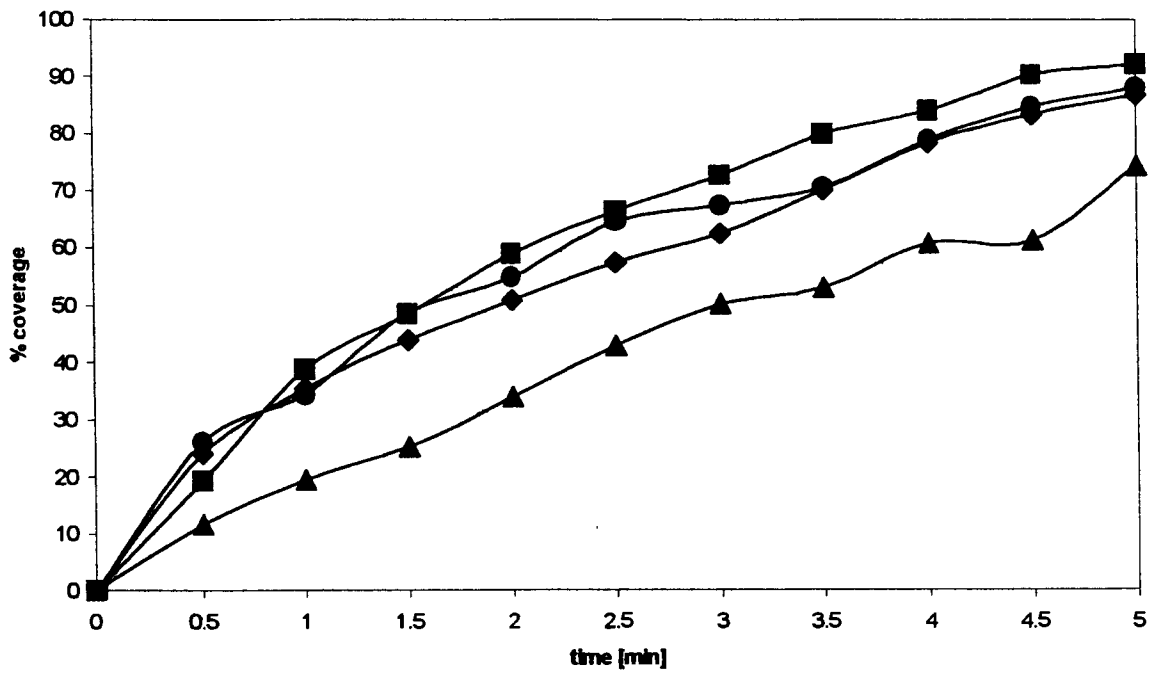
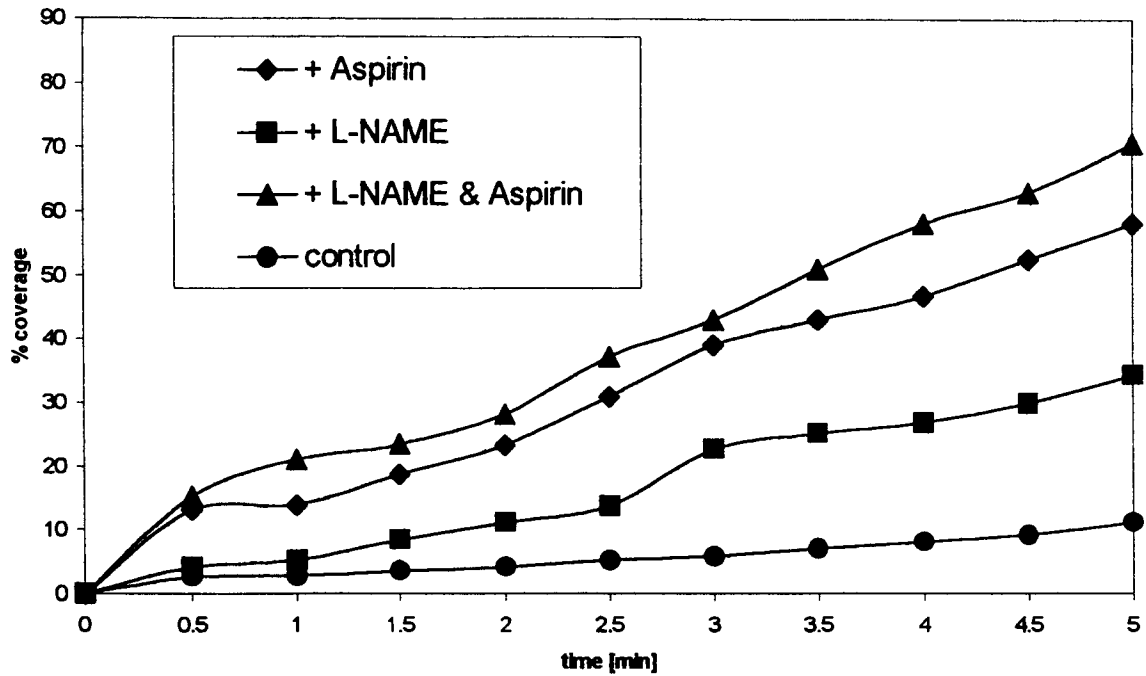


Figure 3: The effect of the nitric oxide release inhibitor, L-NAME, and the PGI₂ release inhibitor, aspirin, on platelet accumulation at a site of injury to an endothelial cell monolayer.

spite of the potential release of these substances at the low shear rate, the concentration of vWF in the subendothelium and on the endothelial surfaces may have been sufficient to mediate platelet attachment at the injury. However, at the high shear rate, an increase in vWF concentration in response to agonist stimulation was required in order to overcome the anti-thrombogenic effect related to endothelial cells.

These results demonstrate the critical role for the endothelium in modulating platelet adhesion and aggregation to an injured vessel wall. Platelet attachment can be enhanced either by preventing release of anti-thrombogenic substances from endothelial cells or by promoting release of pro-thrombogenic compounds.

Lierature Cited

- 1) Ando, J., Ohtsuka, A., Katayama, Y., Korenaga, R., Ishikawa, C. and Kamiya, A. Intracellular calcium response to directly applied mechanical shearing force in cultured vascular endothelial cells. *Biorheology* **31**, 57-68, 1994.
- 2) Bhargyalakshmi, A., Berthiaume, F., Reich, K. M. and Frangos, J. A. Fluid shear stress stimulates membrane phospholipid metabolism in cultured human endothelial cells. *J Vasc Res* **29**, 443-9, 1992.
- 3) Corson, M. A., James, N. L., Latta, S. E., Nerem, R. M., Berk, B. C. and Harrison, D. G. Phosphorylation of endothelial nitric oxide synthase in response to fluid shear stress. *Circ Res* **79**, 984-91, 1996.
- 4) Diamond, S. L., Eskin, S. G. and McIntire, L. V. Fluid flow stimulates tissue plasminogen activator secretion by cultured human endothelial cells. *Science* **243**, 1483-5, 1989.
- 5) Frangos, J. A., Eskin, S. G., McIntire, L. V. and Ives, C. L. Flow effects on prostacyclin production by cultured human endothelial cells. *Science* **227**, 1477-9, 1985.
- 6) Galbusera, M., Zoja, C., Donadelli, R., Paris, S., Morigi, M., Benigni, A., Figliuzzi, M., Remuzzi, G. and Remuzzi, A. Fluid shear stress modulates von Willebrand factor release from human vascular endothelium. *Blood* **90**, 1558-64, 1997.
- 7) James, N. L., Harrison, D. G. and Nerem, R. M. Effects of shear on endothelial cell calcium in the presence and absence of ATP. *Faseb J* **9**, 968-73, 1995.
- 8) Koller, A., Dornyei, G. and Kaley, G. Flow-induced responses in skeletal muscle venules: modulation by nitric oxide and prostaglandins. *Am J Physiol* **275**, H831-6, 1998.
- 9) Nollert, M. U., Hall, E. R., Eskin, S. G. and McIntire, L. V. The effect of shear stress on the uptake and metabolism of arachidonic acid by human endothelial cells. *Biochim Biophys Acta* **1005**, 72-8, 1989.
- 10) Osanai, T., Fujita, N., Fujiwara, N., Nakano, T., Takahashi, K., Guan, W. and Okumura, K. Cross talk of shear-induced production of prostacyclin and nitric oxide in endothelial cells. *Am J Physiol Heart Circ Physiol* **278**, H233-H238, 2000.
- 11) Posch, K., Simecek, S., Wascher, T. C., Jurgens, G., Baumgartner-Parzer, S., Kostner, G. M. and Graier, W. F. Glycated low-density lipoprotein attenuates shear stress-induced nitric oxide synthesis by inhibition of shear stress-activated L-arginine uptake in endothelial cells. *Diabetes* **48**, 1331-7, 1999.
- 12) Shen, J., Lusinskas, F. W., Connolly, A., Dewey, C. F., Jr. and Gimbrone, M. A., Jr. Fluid shear stress modulates cytosolic free calcium in vascular endothelial cells. *Am J Physiol* **262**, C384-90, 1992.

- 13) Tsao, P. S., Lewis, N. P., Alpert, S. and Cooke, J. P. Exposure to shear stress alters endothelial adhesiveness. Role of nitric oxide. *Circulation* **92**, 3513-9, 1995.
- 14) Uematsu, M., Ohara, Y., Navas, J. P., Nishida, K., Murphy, T. J., Alexander, R. W., Nerem, R. M. and Harrison, D. G. Regulation of endothelial cell nitric oxide synthase mRNA expression by shear stress. *Am J Physiol* **269**, C1371-8, 1995.

Characterization of Kinetics and Thermostability of *Acremonium strictum* Glucooligosaccharide Oxidase

Zhiliang Fan, Gbemeloluwa B. Oguntimein, and Peter J. Reilly

Department of Chemical Engineering, Iowa State University, Ames, Iowa 50011-2230

The kinetic and thermostability properties of a glucooligosaccharide oxidase from *Acremonium strictum* were determined. It is most active at pH 9-10.5 and is most stable at pH 6.5. Values of both K_M and V_{max} on maltose are highest at pH 10. Highest values of K_M and V_{max} occur with glucose, maltopentaose, and maltoheptaose, while lowest values of K_M are with maltotriose and of V_{max} are with maltohexaose. This enzyme produces only maltobionic acid from maltose. Values of K_M with any substrate or pH are always substantially above 1 mM. Activation energies for catalysis and thermoinactivation are 23 kJ/mol and 421 kJ/mol, respectively.

INTRODUCTION

Glucooligosaccharide oxidase (E.C.1.1.3.-, GO) was first purified and characterized from the filamentous fungus *Acremonium strictum* T1 (Lin et al., 1991). It is a single glycosylated polypeptide with a molecular mass of 61 kDa, has 1 mol FAD/mol enzyme, and has an isoelectric point at pH 4.3-4.5. GO oxidizes glucose and disaccharides with reducing-end glucosyl residues linked by α - or β -1,4 bonds, for example maltose, cellobiose, and lactose, but not most of other monosaccharides and disaccharides (Lin et al., 1991). GO oxidizes the reducing-end residues of maltooligosaccharides composed of α -1,4 bonds up to at least chain length 7.

The first thirty N-terminal amino acid residues of GO appeared to have no homology with any other protein sequence (Lin et al., 1991).

GO can be used to produce oligosaccharide acids such as lactobionic and maltobionic acids (Lin et al., 1993) and to quantitatively determine substrates such as maltose, lactose, and cellobiose because of its high specificity for them (Lin et al., 1991).

This article reports the further characterization of GO, including its kinetics and thermostability, beyond the studies of Lin et al. (1991, 1993, 1996).

MATERIALS AND METHODS

Materials

4-Aminoantipyrine (4-AA), sodium N-ethyl-N-(2-hydroxy-3-sulfopropyl)-*m*-toluidine (EHST), horseradish peroxidase (87 U/mg, where 1 U forms 1 mg purpurogallin from pyrogallol in 20 s at pH 6.0 and 20°C), catalase (10,900 U/mg, where 1 U decomposes 1.0 μ mol H_2O_2 per min at pH 7.0 and 25°C), glucose, maltotriose (G_3), maltotetraose (G_4), maltopentaose (G_5), maltohexaose (G_6), and maltoheptaose (G_7) were purchased from Sigma. Maltose and trifluoroacetic acid (TFA) came from Fisher. Pyridine and hexamethyldisilazane (HMDS) were purchased from Pierce. Crude GO was a gift from Amano Enzyme U.S.A. and was used unchanged.

Progress of the GO-Catalyzed Reaction

The reaction was carried out at 37°C in a 150-mL beaker with magnetic stirring. The 120-mL reaction mixture contained 0.2 g/L GO, 700 U/mL catalase, and 1.5% maltose. Its pH was con-

trolled to 8.5 with a pH-stat by adding 2 *N* NaOH.

Samples of 100 or 150 μL were taken from 0-300 min and were heated in vials at 100°C for 5 min. The internal standard was 100 μL of 0.5% sucrose solution. Samples were kept at 50°C until they dried, derivatized by adding 500 μL pyridine, 450 μL HMDS, and 50 μL TFA, and incubated at 70°C for 3 h to complete the derivatization (Dowd et al., 1993). Samples of 1 or 2 μL were analyzed with a Hewlett Packard 6890 gas chromatograph with a 30-m \times 0.25-mm i.d. \times 0.1 μm film thickness DB-5 fused silica capillary column (J&W Scientific) and a flame ionization detector.

GO Assay

GO activity or reaction rate was estimated by the modified peroxidase chromogen method by adding 2 mL assay reagent, consisting of 0.3 *M* maltose, 1.5 *mM* EHST, 0.45 *mM* 4-AA, and 3 U/mL peroxidase in pH 5 acetate buffer at 35°C to the samples or vice-versa. Stirring was as before. After a 5-min incubation, the optical density was measured at 550 nm using a 1-cm path-length cuvette. Reaction rate or GO activity was determined by the slope of the absorbance vs. incubation time curve compared with the standard curve using H_2O_2 instead of GO.

Effect of pH on Reaction Rate at 35°C

Samples containing 0.2 mL of 0.5 *M* maltose, 0.2 mL of buffer solution, and 0.1 mL of 0.144 g/L GO were incubated at each of thirteen pHs between 4.0 and 11.5 at 35°C. A Fisher Accumet 825MP meter was used to determine buffer pH, using pH 4.00, 7.00, and 10.00 standards. Reaction rates were measured as above.

Effect of pH on Kinetics of Maltose Oxidation at 35°C

Maltose from 0.002 to 0.2 *M* in various buffer solutions from pH 6.9 to pH 10.5 and 0.1 g/L GO was incubated at 35°C. Eight samples were taken from 0.5 to 16 min at each substrate concentration for each pH, and reaction rates were determined as above. V_{max} and K_M values were determined by fitting the Michaelis-Menten equation to the reaction rate vs. substrate concentration curve with a nonlinear regression routine.

Effect of pH on GO Thermostability at 52.9°C

Samples of 0.25 mL buffer solution and 0.1 mL of 0.452 g/L GO were incubated at 52.9°C at each of nine pHs between 4.5 and 9.2 for eight different times up to 50 h. These 72 samples were chilled in an ice bath for 30 s, followed by 5 min at 35°C, and then residual activities were measured as above, but using only one sample incubated for 5 min. The first-order thermoinactivation rate coefficient, k_d , is the slope of the $\ln(\text{activity})$ vs. incubation time curve.

Effect of Temperature on Reaction Rate at pHs 7 and 10

Samples of 0.25 mL of 0.6 *M* maltose in pH 7 phosphate buffer or pH 10 carbonate buffer, both without NaCl, and 0.1 mL of 0.144 g/L GO solution were incubated at ten different temperatures between 23 and 57°C for pH 7 and at twelve different temperatures between 17 and 40°C for pH 10. Reaction rates were measured as above. Activation energies for catalysis were calculated from slopes of $\ln(\text{rate})$ vs. $1/T$ curves from 23°C to 41°C for pH 7 and 21°C to 33°C for pH 10.

Effect of Temperature on GO Thermostability at pH 7

Mixtures of 0.25 mL of pH 7 phosphate buffer without NaCl and 0.1 mL of 0.144 g/L GO were incubated at eleven different temperatures between 50 and 60°C for eight times ranging from 0-422 min at 50°C to 0-7 min at 60°C. Activities and values of k_d were measured as above. The activation energy for thermoinactivation was determined from the slope of the $\ln k_d$ vs. $1/T$ curve.

Effect of Substrate Chain Length on Oxidation Kinetics at pH 10 and 35°C

Glucose, maltose, G₃, G₄, G₅, G₆, and G₇ were used to determine substrate specificity. Mixtures of 0.5 mL of substrate solution (0.002-0.2 M) in pH 10 carbonate buffer without NaCl and 0.1 mL of 0.144 g/L GO solution were incubated at 35°C. Reaction rates, and from them V_{max} and K_M values, were determined as above.

RESULTS

Composition of Reaction Mixture

The progress of the GO-catalyzed oxidation of maltose at pH 8.5 and 35°C is shown in Figure 1. The maltose was consumed completely at the end of the reaction.

Only three significant peaks other than that of the sucrose internal standard were detected by GC. The derivatized reaction mixture after maltose oxidation yielded peaks with retention times of 39.07, 40.98, and 45.76 min. The first two peaks were trimethylsilyl (TMS)- α -maltose and TMS- β -maltose by comparison to a derivatized sample of pure maltose. The third peak had a molecular weight by CIMS when using NH₃ as the carrier gas of 1023 ($M + 17$), corresponding to TMS-maltobionic acid.

Effect of pH on GO Activity and Thermostability

The effects of pH on GO activity on maltose at 35°C and on GO thermostability at 52.9°C was shown in Figure 2. GO is most active at pH 9-10.5. Activity is somewhat affected by choice of buffer, carbonate buffer giving slightly higher values at optimal pHs. It is also severely affected above pH 10 by low GO thermostability. GO is most stable at pH 6.5, where it retains about 50% of its maximal activity.

Effect of pH on Kinetics of Maltose Oxidation at 35°C

Figure 3 shows the effect of pH on the kinetics of the GO-catalyzed reaction at 35°C. Both K_M and V_{max} reach maxima around pH 10. Although K_M values are relatively high, they are low enough that maltose concentrations in either reaction samples or in the assay solution or both are much more than sufficient to saturate the enzyme. Therefore, the reaction rates or activities measured on maltose throughout this work are actually values of V_{max} .

Effect of Temperature on GO Activity and Thermostability

Figure 4 shows the effect of temperature on GO activity at pHs 7 and 10. Activation energies are 23.7 ± 0.8 kJ/mol between 23 and 41°C at pH 7 and 23.2 ± 0.8 kJ/mol between 21 and 33°C at pH 10, the second values here and later being the standard errors. The effect of temperature on GO

thermostability at pH 7 is shown in Figure 5. The activation energy for GO thermoinactivation between 50 and 60°C at pH 7 is 421 ± 13 kJ/mol.

Effect of Substrate Chain Length on Oxidation Kinetics at pH 10 and 35°C

Values of K_M and V_{max} for GO with glucose and maltooligosaccharides from maltose to G₇ are shown in Figure 6. Values of K_M are very high with glucose, G₅, and G₇, intermediate with maltose, G₄, and G₆, and lowest with G₃. Values of V_{max} are relatively constant from glucose to G₅, lower with G₆, and higher with G₇. A second determination of K_M and V_{max} with G₆ gave essentially the same results.

DISCUSSION

This work differs from that of Lin et al. (1991) in the following ways: 1) the effect of pH on GO activity was measured in buffer solutions with constant ionic strength; 2) the effect of pH on GO thermostability was measured at a higher temperature so that a normal curve resulted, providing more information on the actual optimal pH for thermostability; 3) activation energies for catalysis and thermoinactivation were obtained; 4) K_M and V_{max} values were obtained for maltose at different pHs; 5) K_M and V_{max} values rather than total activities of GO oxidation of substrates from glucose to G₇ were obtained.

The optimal pH for GO activity on maltose at constant ionic strength is similar to that found by Lin et al. (1991), with highest activity at pH 9.0-10.5. This is higher than the optimal pHs of all other O₂-dependent flavin oxidases acting on CH-OH groups, which range from pH 5.6 (glucose oxidase) (Kusai et al., 1960) to pH 8.9 (L-galactonolactone oxidase) (Bleeg and Christensen, 1982). The K_M values for maltooligosaccharides of different chain lengths at pH 10 are much higher than those of other oxidases oxidizing their natural substrates. The isoelectric point of GO is about pH 4.3-4.5 (Lin et al., 1991) and its optimal pH for thermostability is about 6.5, very different than the optimal pH for activity. However, the activation energies for activity of GO at pH 7 and pH 10 are nearly equal, suggesting that the catalytic mechanism is the same at the two pHs.

The variation of K_M and V_{max} with substrate chain length is unusual and not fully explainable. Enzymes with very small active sites generally exhibit increasing values of K_M and decreasing values of V_{max} with homologous substrates of increasing chain length, while enzymes with extended active sites show the opposite. It is unclear why moderately positive correlations between K_M and V_{max} appear with both variations of pH (Fig. 3) and substrate chain length (Fig. 6).

These properties excite interest for the following reasons: 1) It is surprising for an O₂-dependent flavin oxidase, especially one from a filamentous fungus, to have such a high optimal pH for activity; 2) It is unusual for the optimal pHs for activity and thermostability for an enzyme to be so different from one another; 3) It is unusual that K_M values are so high, and also that they vary so much with substrate chain length; 4) It is extremely surprising for an enzyme to be so specific for one glycosyl residue, in this case glucose, and for one glycosidic bond, in this case the (1→4) bond, but yet oxidize substrates with both α - and β -configurations of that bond. These factors lead to the possibility that the true substrate of GO is yet to be found.

Much remains to be learned about GO. A more complete sequence would clarify its relationship with other oxidases and other less related enzymes.

ACKNOWLEDGMENT

We thank Y.-C. Tsai of National Yang-Ming University for providing the enzyme-producing strain of *A. strictum* to Amano Pharmaceutical Co., Ltd., R. Tominaga of Amano Enzyme U.S.A. for providing the enzyme to us, Grain Processing Corp. for funding this project, Zivko Nikolov for his helpful discussions, Anthony Pometto for providing a pH-stat, Preston Rhamy for technical help, Alain Laederach for assisting with the amino acid sequence matching, and Kamel Harrata for help with mass spectroscopy.

REFERENCES

- Bleeg, H.S., Christensen, F. 1982. Biosynthesis of ascorbate in yeast. Purification of L-galactono-1,4-lactone oxidase with properties different from mammalian L-gulonolactone oxidase. *Eur. J. Biochem.* 127:391-396.
- Kusai, K., Sekuzu, I., Hagihara, B., Okunuki, K., Yamauchi, S., Nakai, M. 1960. Crystallization of glucose oxidase from *Penicillium amagasakiense*. *Biochim. Biophys. Acta* 40:555-557.
- Lin, S.-F., Yang, T.-Y., Inukai, T., Yamasaki, M., Tsai, Y.-C. 1991. Purification and characterization of a novel glucooligosaccharide oxidase from *Acremonium strictum* T1. *Biochim. Biophys. Acta* 1118:41-47.
- Lin, S.-F., Hu, H.-M., Inukai, T., Tsai, Y.-C. 1993. Production of novel oligosaccharide oxidase by wheat bran solid-state fermentation. *Biotechnol. Adv.* 11:417-427.
- Lin, S.-F., Hwang, Y.-L., Tsai, Y.-C. 1996. Immobilization of glucooligosaccharide oxidase of *Acremonium strictum* for oligosaccharic acid production. *Biotechnol. Tech.* 10: 63-68.

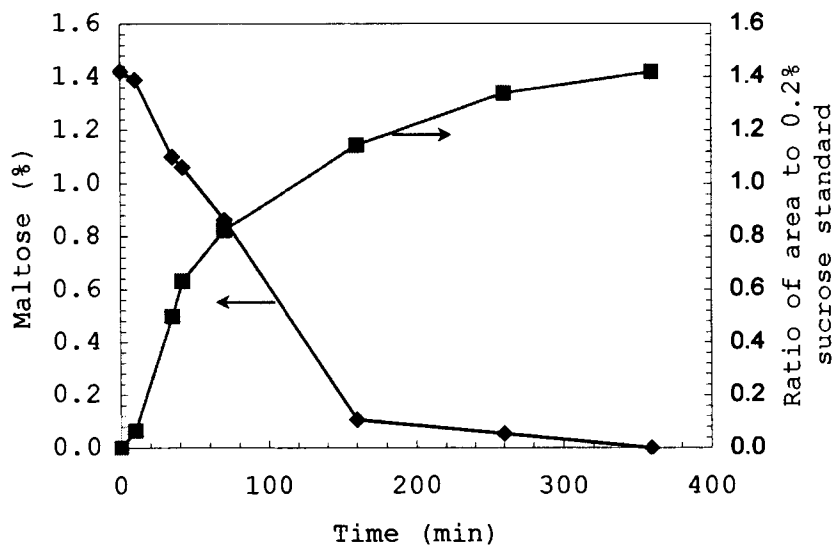


Figure 1. GO-catalyzed production of maltobionic acid from maltose at pH 8.5 and 37°C.

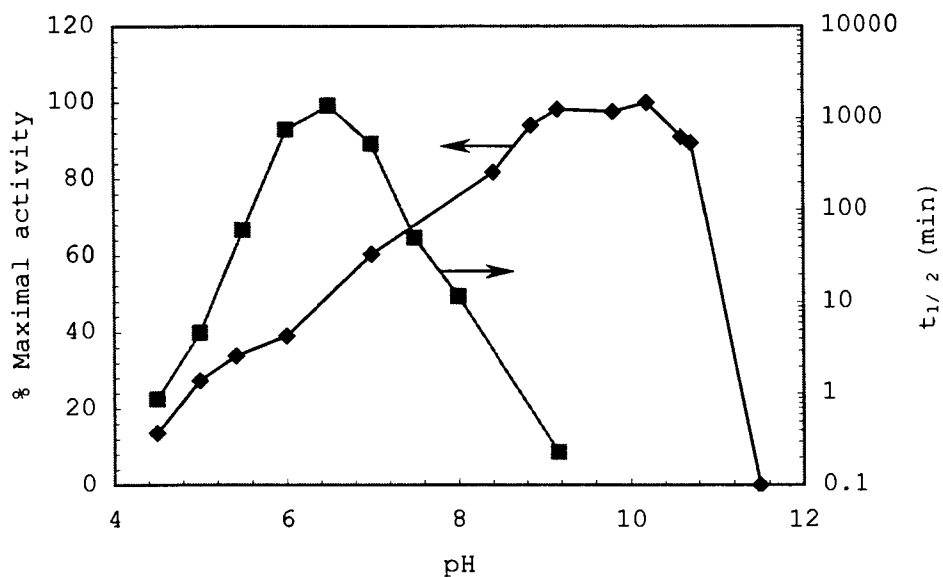


Figure 2. Effect of pH on GO activity on maltose substrate at 35° C and GO thermostability at 52.9°C.

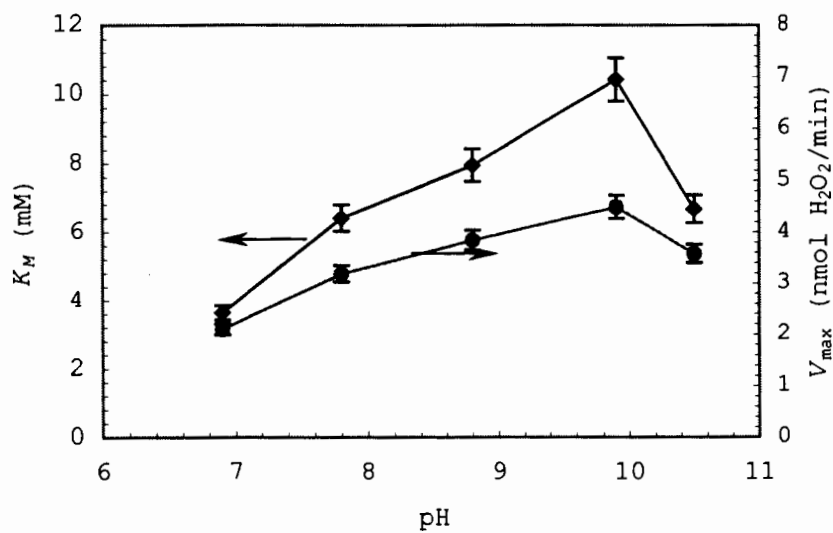


Figure 3. Effect of pH on V_{max} and K_M at 35°C with maltose substrate. Ranges on all the symbols here and in Fig. 6 signify standard errors.

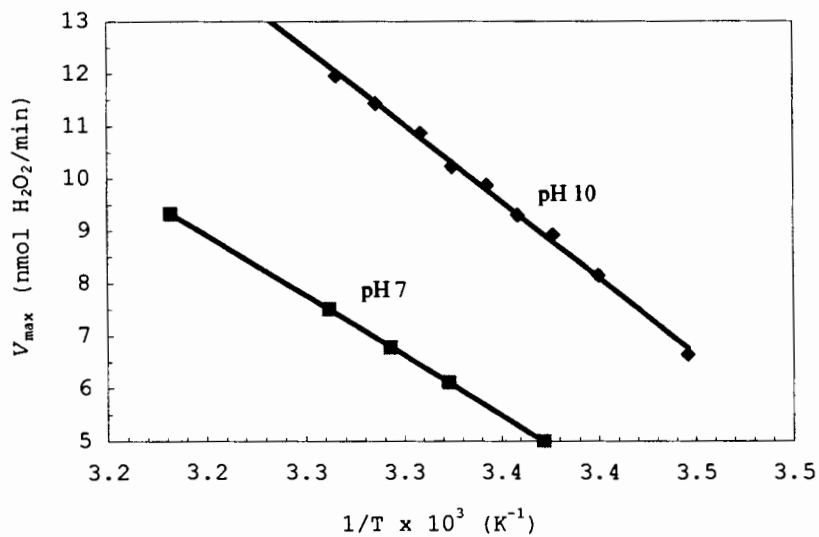


Figure 4. Effect of temperature on V_{max} of GO with maltose substrate at pHs 7 and 10.

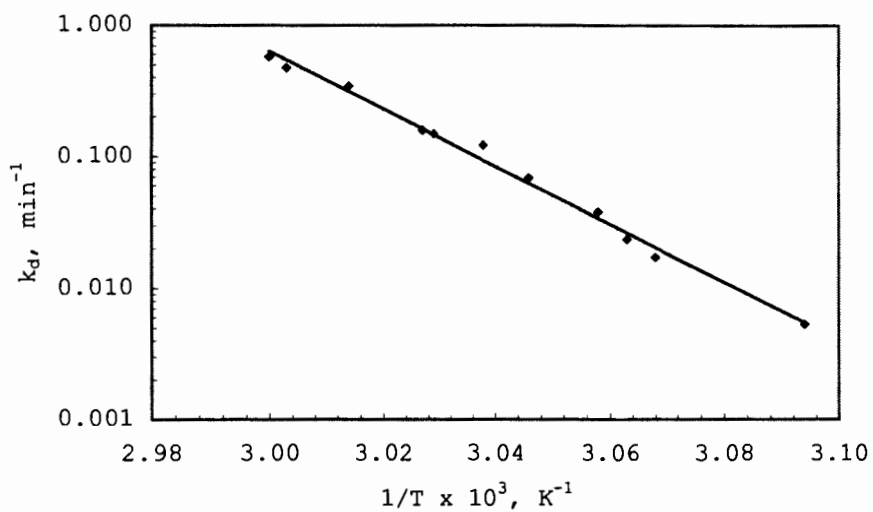


Figure 5. Effect of temperature on GO thermostability at pH 7.

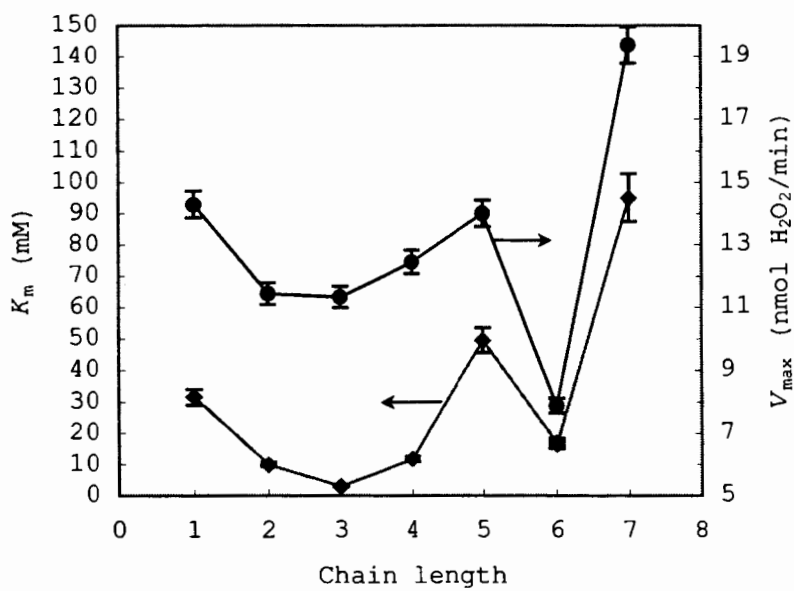


Figure 6. Effect of maltooligosaccharide chain length on V_{max} and K_M at pH 10 and 35°C.

Automated Docking of α -(1 \rightarrow 4)- and α -(1 \rightarrow 6)-Linked Glucosyl Trisaccharides and Maltopentaose into the Soybean β -Amylase Active Site

William M. Rockey, Alain Laederach, and Peter J. Reilly*

Department of Chemical Engineering, Iowa State University, Ames, Iowa 50011-2230

The Lamarckian genetic algorithm of AutoDock 3.0 was used to dock α -maltotriose, methyl α -panoside, methyl α -isopanamide, methyl α -isomaltotrioside, methyl α -(6¹- α -glucopyranosyl)-maltoside, and α -maltopentaose into the closed and, except for α -maltopentaose, into the open conformation of the soybean β -amylase active site. In the closed conformation, the hinged flap at the mouth of the active site closes over the substrate. The nonreducing end of α -maltotriose docks preferentially to subsites -2 or +1, the latter yielding nonproductive binding. Some ligands dock into less optimal conformations with the nonreducing end at subsite -1. The reducing-end glucosyl residue of nonproductively-bound α -maltotriose is close to residue Gln194, which likely contributes to binding to subsite +3. In the open conformation, the substrate hydrogen-bonds with several residues of the open flap. When the flap closes, the substrate productively docks if the nonreducing end is near subsites -2 or -1. Trisaccharides with α -(1 \rightarrow 6) bonds do not successfully dock except for methyl α -isopanamide, whose first and second glucosyl rings dock exceptionally well into subsites -2 and -1. The α -(1 \rightarrow 6) bond between the second and third glucosyl units causes the latter to be improperly positioned into subsite +1; the fact that methyl α -isopanamide is not a substrate of β -amylase indicates that binding to this subsite is critical for hydrolysis.

INTRODUCTION

β -Amylase [α -(1,4)-D-glucan maltohydrolase, EC 3.2.1.2] attacks α -(1 \rightarrow 4) glycosidic linkages to produce β -maltose [α -D-glucopyranosyl-(1 \rightarrow 4)- β -D-glucose] units from the nonreducing ends of maltooligosaccharides.^{1,2} The enzyme has a multiple-attack mechanism, cutting multiple β -maltose units from a maltooligosaccharide chain before the chain is released;^{2,3} the enzyme does not hydrolyze α -(1 \rightarrow 6) bonds.⁴ Substrate binding into the active site does not induce an overall conformational change in the enzyme, but a major local change occurs in loop 3, which borders the rim of the active site,⁵ resulting in open and closed enzyme conformations.

The β -amylase active site is an $(\alpha,\beta)_8$ barrel core with four identified subsites, -2, -1, +1, and +2,⁶ each subsite holding one glucosyl unit of the oligosaccharide substrate. Since the rate of oligosaccharide hydrolysis increases with each additional glucosyl unit up to five,⁷ it can be inferred that a fifth subsite exists. Subsite -2 has the highest binding affinity for a glucosyl ring.⁷ The enzyme hydrolytic site is located between subsites -1 and +1. It consists of two highly conserved residues, Glu186 and Glu380, located below and above, respectively, the plane of the second glucosyl unit from the nonreducing end of the chain (Glc_B).^{5,8} Glu186 appears to be the general acid and Glu380 appears to be the general base in the hydrolysis of the α -(1 \rightarrow 4) bond between Glc_B and Glc_C. Their roles are reversed in the corresponding condensation reaction.⁵

The nonreducing end of the polysaccharide chain enters the barrel first and is assisted into

place by the movable flap loop 3, which is hinged about residues Gly96 and Asp102.^{5,8} This flap is not only involved in catalysis, but its opening is also necessary for product release.⁵ In addition to loop 3's functions in catalysis and substrate maneuvering, it shields the catalytic site from solvent molecules, and it also retains a water molecule located near Glu380 in situ.^{5,9}

Automated docking is able to provide information about protein-ligand interactions of systems that are difficult or impossible to study with X-ray crystallography. In this study, automated docking with the program AutoDock 3.0¹⁰⁻¹³ (AD) using the Lamarckian genetic algorithm (LGA)¹³ generated docked structures of α -(1 \rightarrow 4)- and α -(1 \rightarrow 6)-linked glucosyl trisaccharides and the pentasaccharide α -maltopentaose in the soybean β -amylase active site. The trisaccharides included α -maltotriose [α -D-glucopyranosyl-(1 \rightarrow 4)- α -D-glucopyranosyl-(1 \rightarrow 4)- α -D-glucose], methyl α -panoside [methyl α -D-glucopyranosyl-(1 \rightarrow 6)- α -D-glucopyranosyl-(1 \rightarrow 4)- α -D-glucose], methyl α -isopanoside [methyl α -D-glucopyranosyl-(1 \rightarrow 4)- α -D-glucopyranosyl-(1 \rightarrow 6)- α -D-glucose], methyl α -isomaltotrioside [methyl α -D-glucopyranosyl-(1 \rightarrow 6)- α -D-glucopyranosyl-(1 \rightarrow 6)- α -D-glucose], and methyl α -(6¹- α -D-glucopyranosyl)-maltoside. All trisaccharides were docked into both the open- and closed-flap conformations of the enzyme, while α -maltopentaose was docked only into the latter. The enzyme structures were obtained from the Research Collaboratory for Structural Bioinformatics protein databank. Structure **1bya** is the unliganded, open-flap conformation, while structure **1byb** is the closed conformation obtained by soaking the enzyme with 200 mM maltose.⁵

This study is a continuation of a previous article that reported the automated docking of the even-numbered oligosaccharide chains α - and β -maltose, α - and β -2-deoxymaltose, and α -maltotetraose into the soybean β -amylase active site.¹⁴ The previous study used AD 2.4¹⁰⁻¹² with the simulated annealing docking method. We are using the LGA of version 3.0 here for its greater efficiency and its ability to dock ligands with greater numbers of torsions,¹³ maltotriose and maltopentaose having 18 and 30, respectively, while maltose and maltotetraose have 12 and 24. To ensure the validity of AD 3.0 LGA results, α - and β -maltose were also docked here using the LGA and compared with the simulated annealing results from the previous study.¹⁴

COMPUTATIONAL METHODS

The LGA describes the relationship between a ligand and a protein by the translation, orientation, and conformation of the ligand.¹³ These so-called "state variables" are the ligand's genotype, and the resulting atomic coordinates along with the interaction and intramolecular energies are the ligand's phenotype. Each docking cycle, or generation, consists of a regimen of fitness evaluation, crossover, mutation, and selection; the probabilities that a given individual will undergo crossover and mutation are determined by the user. A Solis and Wets local search then minimizes energy on a user-specified proportion of the population. The user-specified parameter "elitism" determines how many of the top population members enter the next generation.

Docking jobs were run primarily on a DEC AlphaServer 8400/440 with four 440-MHz processors and 1024 MB of memory running Digital UNIX 4.0, although a DEC 3000/900 workstation with a 275-MHz processor and 256 MB of memory and an SGI O2 workstation with a 195-MHz MIPS R10000 processor and 256 MB of memory running IRIX 6.5 were also used.

Using the docked crystallographic α -maltose structures from **1byb** as a reference, the nonreducing end of the ligand was superimposed over the ring of a particular glucosyl residue of

the crystallographic structure. This procedure in effect placed the nonreducing end of the ligand near a particular subsite and facilitated docking by avoiding the need to search meaningless spaces.¹⁴

Three different cases were studied for the docking of α -maltotriose, with its nonreducing end being placed near subsites -2, -1, and +1 in turn. Dockings of trisaccharides with α -(1 \rightarrow 6) bonds and α -maltopentaose were started with their nonreducing ends in subsite -2. Trisaccharides were docked in both the open and closed conformations of β -amylase (**1bya** and **1byb**, respectively), while α -maltopentaose was docked only in the closed conformation. It was assumed that flap orientation did not affect subsite coordinates, and so crystal coordinates of the docked ligands in the closed flap were also used in the open-flap conformation.¹⁴

After docking, the resulting structures for each job were sorted into clusters using a 1.0-Å tolerance all-atom root mean square deviation (RMSD) from the lowest-energy structure. The glucosyl-ring heavy-atom RMSD from the docked crystallographic maltose structures of **1byb** was then calculated for each cluster. Since crystallographic coordinates exist only for subsites -2, -1, +1, +2 in **1byb**, the coordinates for Glc_C of α -maltotriose docked in +1, +2, +3 served as a reference for calculating subsequent RMSDs.

Explicit hydrogen bond modeling was carried out by differentiating polar and nonpolar hydrogens. In this study, a hydrogen bond between the ligand and the enzyme was assumed using a distance-based criterion. Suspected ligand residue hydrogen bond interactions were detected using the Swiss Pdb-Viewer program.¹⁷ The minimal distance detection threshold was set to 2.195 Å and the maximal distance was set to 3.300 + 0.050 Å.

RESULTS AND DISCUSSION

Docking of α -maltotriose in the closed conformation

α -Maltotriose can dock in three different binding modes: to subsites -2, -1, +1; -1, +1, +2; or +1, +2, +3 (Figs. 1 and 2). Docking in subsites -2, -1, +1 would result in β -maltose and α - or β -glucose residues from cleavage of the bond between Glc_B and Glc_C. Binding in subsites -1, +1, +2 would result in α - or β -maltose and β -glucose residues, since in this instance the bond between Glc_A and Glc_B is broken. Docking in subsites +1, +2, +3 is a novel case observed here. This binding mode is nonproductive, since the cleavage point is between subsites -1 and +1; nevertheless, it occurs repeatedly.

The lowest total energy of α -maltotriose docked in subsites -2, -1, +1 (cluster 10) is -151.6 kcal/mol and its internal energy is relatively more positive at -11.6 kcal/mol, which reflects a large degree of strain in the ligand's bonds. The lowest total energy of α -maltotriose docked in subsites -1, +1, +2 is that of cluster 8, with a total energy of -153.4 kcal/mol; however, this cluster is 1.41 Å from the crystal structure **1byb** and has an internal energy of -52.4 kcal/mol. Such a negative value indicates that there is little internal strain within the ligand, and thus its docking is probably nonproductive. Cluster 17 has a total energy of -145.7 kcal/mol with an internal energy of -23.5 kcal/mol and is 0.97 Å from **1byb** when docking into subsites -1, +1, +2. Experimentally, binding in subsites -2, -1, +1, leading to bond cleavage between Glc_B and Glc_C, is preferred over binding in subsites -1, +1, +2 by approximately 240:1.⁷ The most energetically favorable position for α -maltotriose to dock is in subsites +1, +2, +3, although this is not a pro-

ductive binding mode. Its total docked energy is -160.7 kcal/mol with an internal energy of -42.8 kcal/mol. Again, such a negative internal energy indicates that the ligand has little conformational strain.

Analysis of the proportion of intermolecular energies per ring of the three binding modes confirms that subsites -2 and $+1$ have the highest binding affinity. For α -maltotriose docked in subsites $-2, -1, +1$, 40.9% and 39.3% of the intermolecular interaction energy is attributed to Glc_A and Glc_C , respectively. In the $+1, +2, +3$ docking mode, 46.9% of the energy is due to interactions with Glc_A and 21.5% is due to interactions with Glc_C . When α -maltotriose is docked in subsites $-1, +1, +2$, the intermolecular energy is nearly equally shared among the rings, with Glc_A having the highest proportion at 36.1% . However, docking in this mode is not ideal, and we found that the protein-ligand interactions were different from the ones observed in the other docking schemes ($-2, -1, +1$ and $+1, +2, +3$). Using the cleavage distribution of maltotriose, Suganuma et al.⁷ showed that subsite -2 had the highest binding affinity of the subsites $-2, +2$, and $+3$, but their methodology did not allow them to characterize the affinities of the two subsites surrounding the cleavage point.

The torsional angles for α -maltotriose docked in subsites $-2, -1, +1$ and $+1, +2, +3$ are quite different from the corresponding angles of two α -maltose units docked in subsites $-2, -1$ and $+1, +2$. The torsional angles ϕ_{BC} and ψ_{BC} are particularly different from the relaxed conformation assumed between the two α -maltose molecules of **1byb**. In the case of docked α -maltotriose, the bond between Glc_B and Glc_C is about to be hydrolyzed, while in the case of **1byb**, the bond already has been hydrolyzed. The values of ϕ_{BC} and ψ_{BC} of α -maltotriose cluster 17 docked in subsites $-1, +1, +2$ also indicate a high degree of torsional strain between rings Glc_B and Glc_C , although not to the extent of α -maltotriose docked to subsites $-2, -1, +1$. The less negative internal energy and greater degree of torsional strain of the latter binding mode outweigh its slightly less negative total energy to support the experimental results that maltotriose preferentially reacts when bound in subsites $-2, -1, +1$. For the case of nonproductive binding in subsites $+1, +2, +3$, the torsional angles between Glc_A and Glc_B are relatively similar to those of α -maltose docked in subsites $+1, +2$.

The greatest number of hydrogen bonds occur at subsites -2 and $+1$. Gln194 is the main hydrogen binding residue of subsite $+3$. Subsite $+2$ also has only one hydrogen binding residue, His300, as found by Mikami et al.⁵

Docking of α -(1 \rightarrow 6)-linked trisaccharides in the closed conformation

In no case do the trisaccharides methyl α -panoside, methyl α -isomaltotrioside, and methyl α -(6¹- α -glucopyranosyl)-maltoside dock productively into the closed-flap conformation of the β -amylase active site (Fig. 1). Methyl α -(6¹- α -glucopyranosyl)-maltoside is not accommodated in the barrel of the closed conformation at all, but rather remains above the barrel; this failure to dock is likely due to steric hindrance. The total docked energies of the first three of these trisaccharides are relatively less negative than that of α -maltotriose, ranging from -123.4 kcal/mol to -137.9 kcal/mol. Their docked internal energies are quite negative: the lowest-energy docked conformer of methyl α -isomaltotrioside has an internal energy of -16.8 kcal/mol.

For α -(1 \rightarrow 6) bonds, ϕ_{XY} is defined by $\text{O}_{5X}-\text{C}_{1X}-\text{O}_{6Y}-\text{C}_{6Y}$, ψ_{XY} is defined by $\text{C}_{1X}-\text{O}_{6Y}-\text{C}_{6Y}-\text{C}_{5Y}$, and ω_{XY} is defined by $\text{O}_{6Y}-\text{C}_{6Y}-\text{C}_{5Y}-\text{O}_{5Y}$. The α -(1 \rightarrow 6) bond angles are quite dissimilar to

the corresponding α -(1 \rightarrow 4) bonds of α -maltotriose. Indeed, no similarity is seen at all in the α -(1 \rightarrow 6)-dihedral angles among the α -(1 \rightarrow 6)-linked ligands; such random angles indicate that β -amylase does not induce α -(1 \rightarrow 6)-linked residues to assume a particular configuration and is thus unsuited to hydrolyze these bonds.

Methyl α -isopanose is an interesting exception among the four trisaccharides containing α -(1 \rightarrow 6) linkages. Glc_A and Glc_B of this ligand dock very close to subsites -2,-1, with a two-ring RMSD value of 0.33 Å and with a total docked energy of -173.4 kcal/mol, the lowest docked energy of any trisaccharide, including α -maltotriose. In this docked conformation, the internal energy is -22.1 kcal/mol. The torsional angles between Glc_A and Glc_B are nearly identical to those found in **1byb**. Nevertheless, isopanose is not hydrolyzed by sweet potato β -amylase.¹⁸ In fact, the α -(1 \rightarrow 6) bond between Glc_B and Glc_C causes the latter to dock in a position quite different from the third ring of α -maltotriose docked in the same subsite, as seen by comparing their dihedral angles between Glc_B and Glc_C. An analysis of the residue proximities for methyl α -isopanose shows that although Glc_A and Glc_B possess nearly the same residual interactions as Glc_A and Glc_B of α -maltotriose docked in the same subsites, Glc_C of methyl α -isopanose has a single hydrogen bond with Tyr192, as opposed to the seven interactions with five different residues formed by Glc_C of α -maltotriose with subsite +1.

Clearly, hydrogen bond formation (as modeled by residue distance-based interactions) plays an important role in oligosaccharide hydrolysis by β -amylase. The α -(1 \rightarrow 6) bonds of trisaccharides prevent some of their glucosyl rings from positioning themselves close enough to the proper amino acid residues to form hydrogen bonds, leaving the glycosidic bond too far away from the catalytic acid and base to allow hydrolysis.

Docking of α -maltopentaose in the closed conformation

α -Maltopentaose assumes a docked conformation resembling a combination of α -maltotriose docked in subsites -2,-1,+1 and +1,+2,+3 (Fig. 1); the ligand's torsional angles most closely resemble the angles of these two α -maltotriose conformers, although a significant difference is seen in the torsions between Glc_A and Glc_B. The discrepancy can be accounted for by the larger size of α -maltopentaose; a similar difference was observed between docked α -maltotetraose and two α -maltose molecules docked in subsites -2,-1 and +1,+2 by Laederach et al.¹⁴ The total docked energy of α -maltopentaose is -204.6 kcal/mol, with an internal energy contribution of -63.4 kcal/mol. The difficulty of docking α -maltopentaose to **1byb** suggests that the crystal conformation is not well suited to binding larger substrates and that the β -amylase active site will adopt a significantly different conformation upon binding long chains. Interestingly, the greatest difference in ring conformation is observed with Glc_B docked to subsite -1. Therefore, the presence of Glc_E does not allow the ligand to bend in the same way that was observed with α -maltotetraose.¹⁴

α -Maltopentaose docking was a computationally rigorous problem. The random nature of the LGA is beneficial for exhaustively searching a given space for docked conformations; however, the thirty torsions of maltopentaose hindered the efficiency of the algorithm.

Docking of trisaccharides in the open conformation

The docking of trisaccharides in the open-flap conformation produced sparsely populated clusters, indicating that the ligands in the open conformation of β -amylase are only loosely bound and are free to adapt a number of conformations. Allowing for the conformational restrictions imposed by the α -(1 \rightarrow 6) bond, no significant difference in docked structures is observed among α -maltotriose, methyl α -panoside, methyl α -isopanoside, methyl α -isomaltotriose, and methyl α -(6¹- α -glucopyranosyl)-maltoside.

The lowest energy observed among the docked structures is -151.3 kcal/mol with an internal energy of -47.3 kcal/mol for α -maltotriose. Distributing the atomic intermolecular energies among the rings shows that Glc_A near subsite -2 contributes 45.1% of the interaction energy, while Glc_B and Glc_C contribute 30.2% and 24.7%, respectively. Trisaccharides with α -(1 \rightarrow 6) bonds tend to have less negative internal energies than α -maltotriose; in the lowest-energy docked structure of methyl α -isomaltotriose, for example, the internal energy is -20.8 kcal/mol. Glc_A and Glc_C contribute 38.4% and 29.8% of the intermolecular interaction energy between methyl α -isomaltotriose and the enzyme, with the remainder shared between Glc_B and the methyl group.

Although three jobs were performed with the nonreducing end of the α -maltotriose placed successively in subsites -2 , -1 , or $+1$, the initial placement of the ligand does not affect the outcome of the docking in the open conformation, since in all cases the nonreducing end of the trisaccharide tends to migrate toward subsite -2 (Fig. 3). In most cases, however, the ligands do not assume a docked conformation at all comparable to the docked α -maltose units in the crystal structure **1byb**.

β -Amylase's hinged flap is comprised of residues 96-103^{5,8}, and α -maltotriose docked closely to three of these residues, Gly96, Asn98, and Asp101, along with the adjacent residues His93 and Gln94. From these results, one may surmise that an oligosaccharide enters the enzyme in the open conformation and is drawn into the barrel of the enzyme toward the high-binding affinity subsites -2 or $+1$. The ligand hydrogen-bonds with the flap itself, and the flap then closes, positioning the oligosaccharide for optimal hydrogen-bonding interaction and inducing torsional stress within the ligand.

ACKNOWLEDGMENTS

The authors gratefully acknowledge the assistance of Michael Dowd of the USDA Southern Regional Research Center in New Orleans, La. for generating the computer model for α -maltopentaose and for many helpful discussions; of the Iowa State University High Performance Computing Group for use of its FARM server; of Arthur Olson and Garrett Morris of the Scripps Research Institute in La Jolla, Cal. for their assistance and provision of AutoDock 3.0; and of Pedro Coutinho of the CNRS Centre d'Architecture et Fonction des Macromolécules Biologiques in Marseille, France for use of his data analysis utilities.

REFERENCES

1. Ohlsson E. The two components of malt diastase, especially with reference to the muta-

- rotation of the of the products formed in the hydrolysis of starch. *Z Physiol Chem* 1930;189:17-63.
2. Bailey JM, French D. Significance of multiple reactions in enzyme-polymer systems. *J Biol Chem* 1957;226:1-14.
 3. French D, Youngquist RW. The mode of action of β -amylase on starch oligosaccharides. *Stärke* 1963;15:425-431.
 4. Summer R, French D. Action of β -amylase on branched oligosaccharides. *J Biol Chem* 1956;222:469-477.
 5. Mikami B, Degano M, Hehre EJ, Sacchettini JC. Crystal structures of soybean β -amylase and maltal: Active site components and their apparent roles in catalysis. *Biochemistry* 1994;33:7779-7787.
 6. Davies GJ, Wilson KS, Henrissat B. Nomenclature for sugar-binding subsites in glycosyl hydrolases. *Biochem J* 1997;321:557-559.
 7. Suganuma T, Ohnishi M, Hiromi K, Morita Y. Evaluation of subsite affinities of soybean β -amylase by product analysis. *Agric Biol Chem* 1980;44:1111-1117.
 8. Mikami B, Hehre EJ, Sato M, Katsube Y, Hirose M, Morita Y, Sacchettini JC. The 2.0-Å resolution structure of soybean β -amylase complexed with α -cyclodextrin. *Biochemistry* 1993;32:6836-6845.
 9. Kunikata T, Nishimura S, Nitta Y. Maltal binding mechanism and a role of the mobile loop of soybean β -amylase. *Biosci Biotechnol Biochem* 1996;60:1104-1108.
 10. Goodsell DS, Olson AJ. Automated docking of substrates to proteins by simulated annealing. *Proteins* 1990;8:195-202.
 11. Goodsell DS, Lauble H, Stout CD, Olson AJ. Automated docking in crystallography: Analysis of the substrates of aconitase. *Proteins* 1993;17:1-10.
 12. Goodsell DS, Morris GM, Olson AJ. Docking of flexible ligands. Applications of AutoDock. *J Mol Recog* 1996;9:1-5.
 13. Morris GM, Goodsell DS, Halliday RS, Huey R, Hart WE, Belew RK, Olson AJ. Automated docking using a Lamarckian genetic algorithm and an empirical binding free energy function. *J Comp Chem* 1998;19:1639-1662.
 14. Laederach A, Dowd MK, Coutinho PM, Reilly PJ. Automated docking of maltose, 2-deoxymaltose, and maltotetraose into the soybean β -amylase active site. *Proteins* 1999;37:166-175.
 17. Guex N, Peitsch MC. SWISS-MODEL and the Swiss-PdbViewer: An environment for comparative protein modeling. *Electrophoresis* 1997;18, 2714-2723.
<http://www.expasy.ch/spdbv/mainpage.htm>.
 18. Sakano Y, Sano M, Kobayashi T. Hydrolysis of α -1,6-glucosidic linkages by α -amylase. *Agric Biol Chem* 1985;49:3041-3043.
 19. Cason C and the Persistence of Vision Development Team. POV-Ray for Windows. 1998.
<http://www.povray.org>.

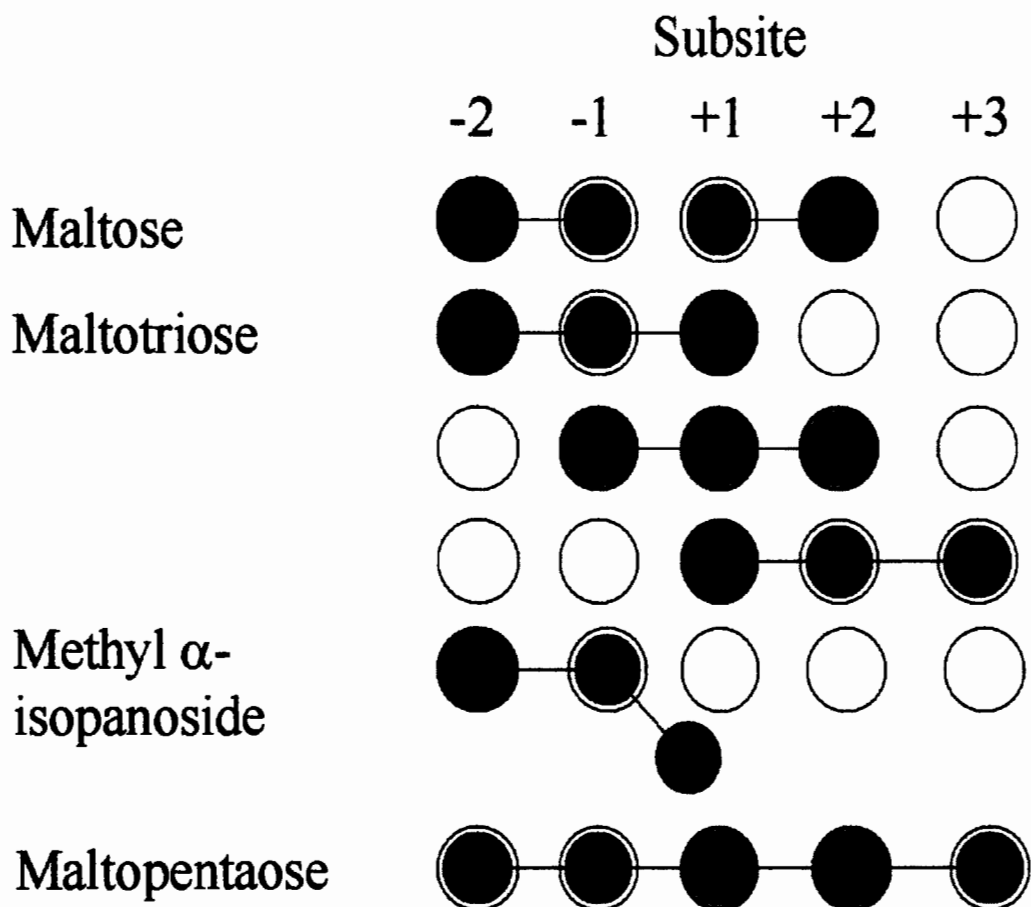


Fig. 1. The possible docking modes of maltose, maltotriose, methyl α -isopanoside, and maltopentaose. Cleavage occurs between subsites -1 and +1. Maltose docks in two possible configurations, while maltotriose docks in three. Dark, light, and white borders signify residues with highest, intermediate, and lowest subsite interaction energies. Trisaccharides with α -(1 \rightarrow 6) glycosidic bonds other than methyl α -isopanoside generally do not dock.

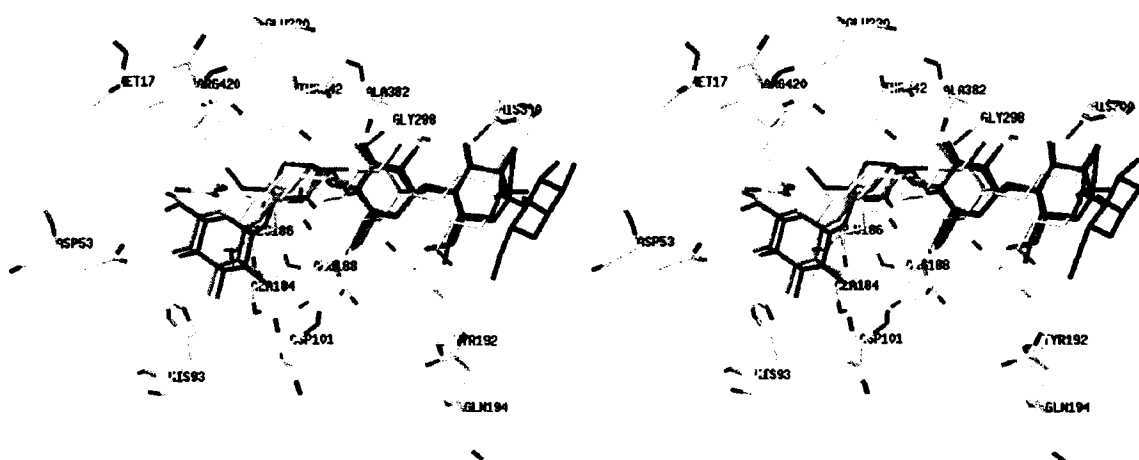


Fig. 2. α -Maltotriose docked in subsites $-2,-1,+1$, $-1,+1,+2$, and $+1,+2,+3$, along with two α -maltose ligands (dark gray) in the closed-flap crystal structure of β -amylase from **1byb**.

Structures in Figures 2-5 were generated in Swiss-PdbViewer 3.5b3.¹⁷

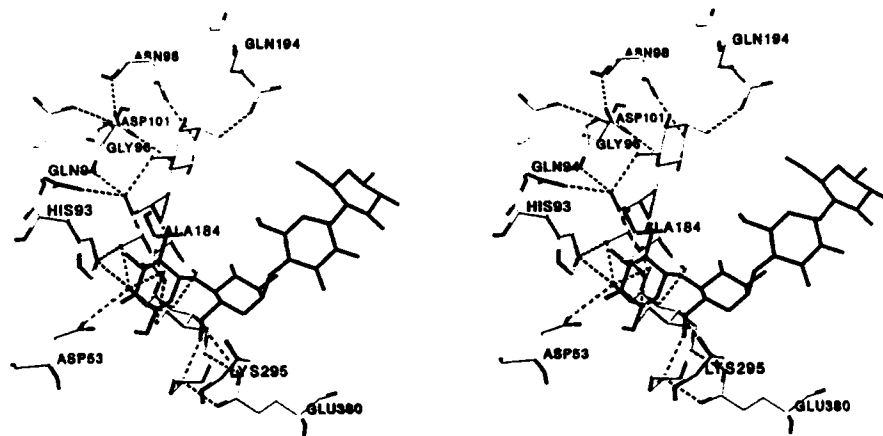


Fig. 3. α -Maltotriose docked in the open conformation of β -amylase from 1bya, along with two α -maltose ligands (dark gray) from the closed-flap crystal structure of 1byb. Distance-based residue interactions are also shown (dashed lines). The structure was rendered with POV-Ray.¹⁹

High-performance anion-exchange chromatography of sugar and glycerol phosphates on quaternary ammonium resins

Ian C. Schneider, Preston J. Rhamy, Ruth J. Fink-Winter, and Peter J. Reilly*
Department of Chemical Engineering, Iowa State University, Ames, IA 50011-2230

Abstract

Twenty-six sugar and glycerol phosphates were separated by high-performance anion-exchange chromatography on an alkyl quaternary ammonium column at pH 6.0 with 0.1 M sodium acetate eluant. Capacity, asymmetry, and response factors of the compounds vary widely. Secondary acidic dissociation constants of fourteen of these phosphates were determined in an attempt to explain the separation mechanism.

Introduction

High-performance anion-exchange chromatography (HPAEC) with strong-base resins has been widely used to separate sugars; early articles described the separation of simple mono-, di-, and oligosaccharides [1-7], homologous oligosaccharide series [7-9], and oligosaccharides with several different monomeric residues [10-15]. These separations usually occurred at very high pH where the slight acidity of carbohydrates allows a proton to be abstracted.

Strong-base resins have also separated sugar compounds such as aldonic and uronic acids that are negatively charged at more neutral pHs [6,16-18]. The separation of sugar phosphates, which usually also have a negative charge near neutral pH, has been comparatively neglected. We report here the use of HPAEC with an alkyl quaternary ammonium resin at pH 6.0 with 0.1 M sodium acetate (NaOAc) buffer to separate 26 sugar and glycerol phosphates. Except for L-3-glycerophospho-D-1-*myo*-inositol, all have two potentially dissociable hydrogen atoms. Capacity factors of the α -sugar 1-phosphates have been correlated with those of the phosphate-free parent compounds, obtained with 0.1 M NaOH eluant on an almost identical column [7], and secondary acidic dissociation constants of some of the phosphates have been measured to allow comparison of factors that determine capacity factors. We had previously separated some of these phosphates by capillary gas chromatography following their derivatization with hexamethyldisilazane [19].

Experimental

Materials.—Sugar and glycerol phosphates obtained from Sigma Chemical were used without further purification.

Chromatography.—The eluant was room temperature 0.1 M NaOAc buffer, made with solid NaOAc and deionized water and brought to pH 6.00 with glacial HOAc. The pH was measured with a Fisher Accumet 910 pH meter and Corning 476087 general purpose combination electrode, standardized with Fisher pH 4.00 potassium biphthalate and pH 7.00 $K_2HPO_4/NaOH$ buffers. Sugar and glycerol phosphate samples were dissolved in 0.1 N NaOAc buffer to, with one exception, 2-20 g/L. Injection volumes were 20 μ L and eluant flow was 1 mL/min. Variations in data caused by changes in eluant batches were normalized by use of capacity factors of standards. In

general each sample was chromatographed twice; peak dimensions and asymmetry and response factors were calculated individually and then averaged. Weights and therefore response factors are based on the free acid contents of the pure, dry compounds in the samples.

Measurement of acidic dissociation constants.—The negative \log_{10} of the secondary acidic dissociation constant (pK_2) was obtained by titration at 25°C of salts of a number of the sugar and glycerol phosphates subjected to HPAEC. This was done with the same pH meter but with a Corning 476531 general purpose combination electrode standardized with 50 mM of either Fisher pH 2.00 HCl/KCl or pH 4.00 potassium biphthalate buffer, plus 50 mM Fisher pH 7.00 K_2HPO_4 /NaOH and 50 mM Fisher pH 10.00 K_2CO_3 / KBO_3 /KOH buffers. The titrant was 10 or 100 mM Fisher standardized HCl, except for the free acid of DL-glyceraldehyde 3-phosphate, when it was 10 mM Fisher standardized NaOH, and the initial sample concentration was generally 4-10 mM. In these ranges there is little effect of varying either acid or sample concentration on pK_2 , obtained by measuring the pH at 50% of the acid volume needed to reach the equivalence point (Fig. 1) and correcting to infinite dilution by calculating the activity coefficient f_i for each ion i with the Debye-Hückel equation as modified by Davies [20], where z_i is the charge and I is the ionic strength.

$$-\log_{10} f_i = 0.5115 \frac{z_i^2 I^{1/2}}{1 + I^{1/2}} - 0.1z_i^2 I$$

Values of pK_1 , which would be obtained from the pH at 1.5 times the acid volume needed to reach the equivalence point, are much more strongly affected by changes of acid and sample concentrations (Fig. 1) [21].

Results

HPAEC with strong-base resin and 0.1 M NaOAc buffer eluant at pH 6.0.—Twenty-six sugar and glycerol phosphates, one with one dissociable hydroxyl group and 25 with two, were chromatographed on the CarboPac PA1 column. Their k' values are presented in order of increasing magnitude in Table 1. Neither sugar bisphosphates nor compounds with both phosphate and carboxyl groups exited the column with the present eluant, although presumably they would if a gradient with an increasing concentration of NaOAc buffer were imposed upon the column. Furthermore, no satisfactory peak could be obtained with DL-glyceraldehyde 3-phosphate.

Measurement of acidic dissociation constants.—Values of pK_2 were obtained for fourteen of the 26 sugar and glycerol phosphates that had been subjected to HPAEC (Table 1). In addition, values for seven of the chromatographed phosphates had been obtained previously [22]. For five phosphates, values from both the literature and from our work exist; three agree rather closely but two pK_2 's, those for α -D-galactose 1-phosphate and DL-glycerol 3-phosphate, differ significantly from each other, that obtained here for the former being higher and that for the latter being lower than the corresponding literature values [22].

Discussion

At pH 6.0, the value at which chromatography was conducted, L-3-glycerophospho-D-1-myoinositol, the one compound with only one dissociable hydroxyl group, is almost all negatively charged. The bulk of the pK_2 values of the 24 compounds with two dissociable hydroxyl groups

are between 6.1 and 6.6. Therefore at pH 6.0 slightly more than half of the phosphate groups of these compounds have one negative charge, somewhat fewer than half have two negative charges, and a very small fraction have no negative charges. This difference in net charge causes L-3-glycerophospho-D-1-*myo*-inositol to be eluted much before the other compounds.

Asymmetry factors varied greatly, being much higher for the later-eluting compounds than for the ones that eluted earlier. The tailing of those compounds with higher k' values, which decreases the probability that they can be fully separated, presumably would be ameliorated by using an eluant with an increasing NaOAc concentration gradient. This was not done in this project so that k' values unaffected by changing buffer composition could be obtained.

Response factors also varied greatly. Differences in molecular structure did not seem to explain this. Those compounds having very low response factors, such as α -L-fucose 1-phosphate, β -L-fucose 1-phosphate, and D-erythrose 4-phosphate, were no more likely to have low capacity factors than those compounds with high response factors, such as L-3-glycerophospho-D-1-*myo*-inositol, α -D-galactose 1-phosphate, D-glucose 6-phosphate, β -D-glucose 1-phosphate, and D-xylulose 5-phosphate.

Capacity factors of the 24 sugar and glycerol phosphates with two dissociable hydroxyl groups that gave discernable peaks ranged from 3.45 to 8.05, with the bulk falling between 4.5 and 6.0. An increasing NaOAc gradient would reduce this range but, as mentioned above, it would probably increase resolution between most peaks by reducing their asymmetry.

There is a statistically insignificant negative correlation ($R = 0.71$) between k' and pK_2 for the seventeen sugar and glycerol phosphates having both values, caused by the relative similarity of the latter values to each other. This suggests that other factors also have a substantial effect on k' , unlike the case with sugars and sugar alcohols, where the pK range is much wider and there is a strong correlation between k' and pK for monosaccharides [7].

Correlations between k' values of the same sugar phosphates obtained by us and by others on strong-base columns under different conditions are not possible because not enough compounds in common have been chromatographed. However, several further important observations on our results can be made:

(i) Both α -L-fucose 1-phosphate and α -D-glucose 1-phosphate were eluted before their corresponding β -linked forms. Sterically it appears easier for equatorial β -1-phosphate groups rather than axial α -1-phosphate groups to bind to the alkyl quaternary ammonium groups on the carrier; in addition β -D-glucose 1-phosphate has a lower pK_2 than does α -D-glucose 1-phosphate.

(ii) α -D-Mannose 1-phosphate and α -D-ribose 1-phosphate were eluted after D-mannose 6-phosphate and D-ribose 5-phosphate, respectively, but 2-deoxy- α -D-ribose 1-phosphate was eluted before 2-deoxy-D-ribose 5-phosphate. Furthermore, α -D-galactose 1-phosphate and D-galactose 6-phosphate were eluted at about the same time, as were α -D-glucose 1-phosphate and D-glucose 6-phosphate. The inductive effect of the ring oxygen causes high acidity of the hydrogen atom of the anomeric hydroxyl group [23], and by extension to hydrogen atoms of phosphate groups linked to the oxygen atom of that group. This would make k' values of most sugars with α -1-phosphate groups greater than the equivalent sugars with phosphate groups linked to other hydroxyl groups. However, the lack of a 2-OH in 2-deoxy- α -D-ribose 1-phosphate eliminates the possibility of hydrogen bonding between it and the phosphate group, decreasing the acidity of the latter and making k' of 2-deoxy- α -D-ribose 1-phosphate lower than that of 2-deoxy-D-ribose 5-phosphate.

(iii) There is a rough correlation ($R = 0.88$) between k' values for seven sugars eluted with 0.1 N NaOH from a Dionex HPIC-AS6 column [7] and those of corresponding sugars with α -1-phos-

phate groups eluted with 0.1 M NaOAc buffer from a very similar Dionex CarboPac PA1 column (Fig. 2). As noted above, the strong acidities of anomeric sugar hydroxyl groups should carry over to the corresponding α -1-sugar phosphates.

iv) There is a statistically insignificant positive correlation ($R = 0.61$) between k' values of parent sugars and those of the corresponding sugars with phosphate groups elsewhere on the molecule other than the reducing oxygen atom.

Sugar and glycerol phosphates are important physiological agents and have potential industrial uses. Their analytical and preparative separation is of value. The technique described here allows that possibility.

Acknowledgement

The authors are grateful for the support of the U.S. Department of Agriculture through the Biotechnology Byproducts Consortium, a partnership of Iowa State University, the University of Iowa, and the City of Cedar Rapids, Iowa. They also thank Charles Glatz and his group for the use of the pH meter and Walter Trahanovsky for helpful discussions.

References

- [1] R. D. Rocklin and C. A. Pohl, *J. Liq. Chromatogr.*, 6 (1983) 1577-1590.
- [2] D. C. Johnson, *Nature*, 321 (1986) 451-452.
- [3] W. T. Edwards, C. A. Pohl, and R. Rubin, *Tappi J.*, 70 (1987) 138-140.
- [4] M. R. Hardy, R. R. Townsend, and Y. C. Lee, *Anal. Biochem.*, 170 (1988) 54-62.
- [5] N. J. Chatterton, P. A. Harrison, W. R. Thornley, and J. H. Bennett, *Plant Physiol. Biochem.*, 27 (1989) 289-295.
- [6] D. A. Martens and W. T. Frankenberger, Jr., *Chromatographia*, 29 (1990) 7-12.
- [7] T. J. Paskach, H.-P. Lieker, P. J. Reilly, and K. Thielecke, *Carbohydr. Res.*, 215 (1991) 1-14.
- [8] K. Koizumi, Y. Kubota, T. Tanimoto, and Y. Okada, *J. Chromatogr.*, 454 (1988) 303-310.
- [9] K. Koizumi, Y. Kubota, T. Tanimoto, and Y. Okada, *J. Chromatogr.*, 464 (1989) 365-373.
- [10] M. R. Hardy and R. R. Townsend, *Proc. Nat. Acad. Sci. U.S.A.*, 85 (1988) 3289-3293.
- [11] R. R. Townsend, M. R. Hardy, O. Hindsgaul, and Y. C. Lee, *Anal. Biochem.*, 174 (1988) 459-470.
- [12] L.-M. Chen, M.-G. Let, and M.-C. Shao, *FASEB J.*, 2 (1988) 2817-2824.
- [13] M. R. Hardy and R. R. Townsend, *Carbohydr. Res.*, 188 (1989) 1-7.
- [14] R. R. Townsend, M. R. Hardy, D. A. Cumming, J. P. Carver, and B. Bendiak, *Anal. Biochem.*, 182 (1989) 1-8.
- [15] W. T. Wang and D. Zopf, *Carbohydr. Res.*, 189 (1989) 1-11.
- [16] A. T. Hotchkiss, Jr. and K. B. Hicks, *Anal. Biochem.*, 184 (1990) 200-206.
- [17] M. O'Neill, P. Albersheim, and A. Darvill, *Methods Plant Biochem.*, 2 (1990) 415-441.
- [18] H.-P. Lieker, K. Thielecke, K. Buchholz, and P. J. Reilly, *Carbohydr. Res.*, 238 (1993) 307-311.
- [19] S. L. Johansen, A. Sivasothy, M. K. Dowd, P. J. Reilly, and E. G. Hammond, *J. Am. Oil Chem. Soc.*, 73 (1996) 1275-1286.
- [20] C. W. Davies, *J. Chem. Soc.*, (1938) 2093-2098.
- [21] D. A. Skoog, D. M. West, and F. J. Holler, *Fundamentals of Analytical Chemistry*, 6th

- ed., Saunders College Publishing, Fort Worth, 1992, pp 227-228.
- [22] R. M. C. Dawson, D. C. Elliott, W. H. Elliott, and K. M. Jones, *Data for Biochemical Research*, 3rd ed., Oxford Science Publications, Oxford, 1986, pp 55-73.
- [23] J. A. Rendelman, Jr., *Adv. Chem. Ser.*, 117 (1971) 51-69.

Table 1. Separation of organic phosphates on a Carbowac PA1 quaternary ammonium column eluted with 0.1 M NaOAc buffer at pH 6.0; acidic dissociation constants of many of the same phosphates.

Compound	t_R^a min	k'	W μg	w_0 min	a min	AF	H $\text{mV}\cdot 10^4$	A $\text{mV}\cdot \text{min}\cdot 10^4$	RF $\text{mV}\cdot \text{min}/\text{g}$	pK_1	pK_2
L-3-Glycerophospho- D-1- <i>myo</i> -inositol	1.61 (2) ^b	0.11	2.2	0.205	0.09	1.3	3.0	0.32	14.9		
α -L-Fucose 1-phosphate	6.52 (2)	3.45	152	0.455	0.34	0.34	2.7	0.76	0.50		
2-Deoxy- α -D-ribose 1-phosphate	7.86 (2)	4.42	90	0.455	0.22	1.1	5.1	1.18	1.31		
α -D-Galactose 1-phosphate	8.01 (2)	4.56	183	0.775	0.51	0.52	19.2	6.47	3.53	1.00 ^c	6.17 ^c , 6.50 (2)
β -L-Fucose 1-phosphate	8.10 (1)	4.63	176	0.55	0.30	0.83	4.2	1.42	0.81		
D-Galactose 6-phosphate	8.28 (2)	4.77	295	0.75	0.29	1.6	17.7	5.98	2.03		6.51 (4)
<i>myo</i> -Inositol 1-phosphate	8.35 (2)	4.78	60	0.465	0.25	0.86	4.8	1.07	1.78		
D-Mannose 6-phosphate	8.45 (2)	4.85	247	0.73	0.26	1.8	17.7	6.45	2.62		6.63 (3)

α -D-Glucose 1-phosphate	8.65 (1)	4.92	360	1.29	0.33	2.9	13.2	7.66	2.13	1.11 ^c	6.13 ^c , 6.26 (5)
D-Glucose 6-phosphate	8.58 (2)	4.93	318	0.99	0.38	1.6	22.8	10.52	3.31		6.11 ^c
2-Deoxy-D-ribose 5-phosphate	8.56 (2)	4.94	226	0.84	0.17	3.9	10.2	4.19	1.85		6.28 (3)
DL-Glycerol 3-phosphate	8.68 (2)	5.00	203	1.04	0.245	3.2	6.6	3.38	1.66		6.66 ^c , 6.44 (3)
D-Ribose 5-phosphate	8.73 (1)	5.10	409	1.33	0.39	2.4	12.0	6.35	1.55		6.33 (7)
α -D-Xylose 1-phosphate	9.00 (2)	5.23	196	0.89	0.185	3.8	9.3	4.07	2.08		6.26 (2)
α -D-Mannose 1-phosphate	9.17 (2)	5.28	59	0.415	0.175	1.4	3.0	0.74	1.15		
⁸⁸ D-Fructose 6-phosphate	9.15 (2)	5.31	229	0.95	0.31	2.1	13.2	5.98	2.62	0.97 ^c	6.11 ^c
Dihydroxyacetone phosphate	9.58 (2)	5.59	107	0.97	0.36	1.7	2.4	1.16	1.07	1.77 ^c	6.45 ^c
D-Fructose 1-phosphate	9.46 (2)	5.60	237	1.36	0.28	3.8	9.6	5.83	2.47		6.19 (3)
Glycerol 2-phosphate	9.58 (2)	5.68	341	1.72	0.47	2.7	6.3	4.93	1.45	1.34 ^c	6.55 ^c , 6.55 (5)
α -D-Ribose 1-phosphate	9.74 (2)	5.69	110	0.935	0.21	3.5	6.6	2.69	2.44		6.28 (2)
D-Erythrose 4-phosphate	10.02 (2)	5.96	176	0.655	0.235	1.8	1.2	0.45	0.26		
<i>myo</i> -Inositol 2-phosphate	10.45 (2)	6.18	158	1.36	0.295	3.6	8.1	5.07	3.21		5.84 (2)
D-Ribulose 5-phosphate	11.65 (2)	7.06	149	1.36	0.33	3.2	3.0	2.03	1.36		

β -D-Glucose 1-phosphate	11.91 (2)	7.21	62	1.77	0.27	6.1	6.1	4.39	7.04	5.89 (2)
D-Xylulose 5-phosphate	13.17 (2)	8.05	45	1.53	0.425	2.6	4.5	3.75	8.28	
DL-Glyceraldehyde 3-phosphate										1.42 ^c 6.45 ^c , 6.41 (2)

^a Explanation of symbols: t_R : elapsed time between injection and peak mode; k' : capacity factor, $(t_R - t_0)/t_0$, where t_0 is elapsed time between injection and beginning of solvent peak and is between 1.43 and 1.47 min in all cases; W : weight of standard entering detector, based on pure, dry free acid; w_0 : peak width at baseline; a : elapsed time between beginning of peak at baseline and peak mode; AF : asymmetry factor, $(w_0 - a)/a$; H : peak height; A : peak area; RF : response factor, A/W [38]

^b Number of chromatographic runs or titrations in parentheses.

^c Ref. 22.

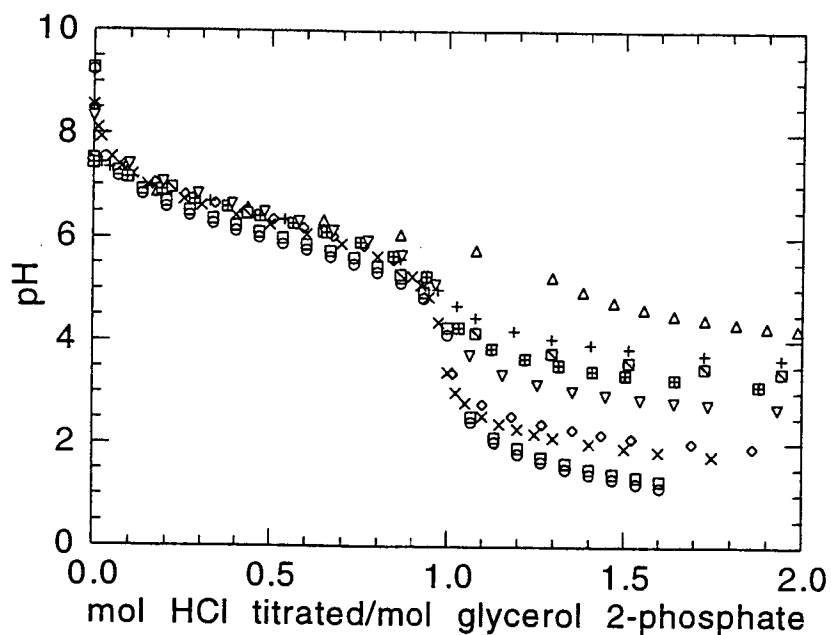


Fig. 1. Effect of HCl concentration and initial sample concentration on the titration of glycerol 2-phosphate. (HCl, mM/glycerol 2-phosphate, mM): \triangle , 1/0.116; $+$, 1/0.463; \boxtimes , 10/0.463; \boxplus , 10/1.06; ∇ , 10/5.19; \diamond , 100/29.6; \times , 100/100; \square , 1000/300; \circ , 1000/600.

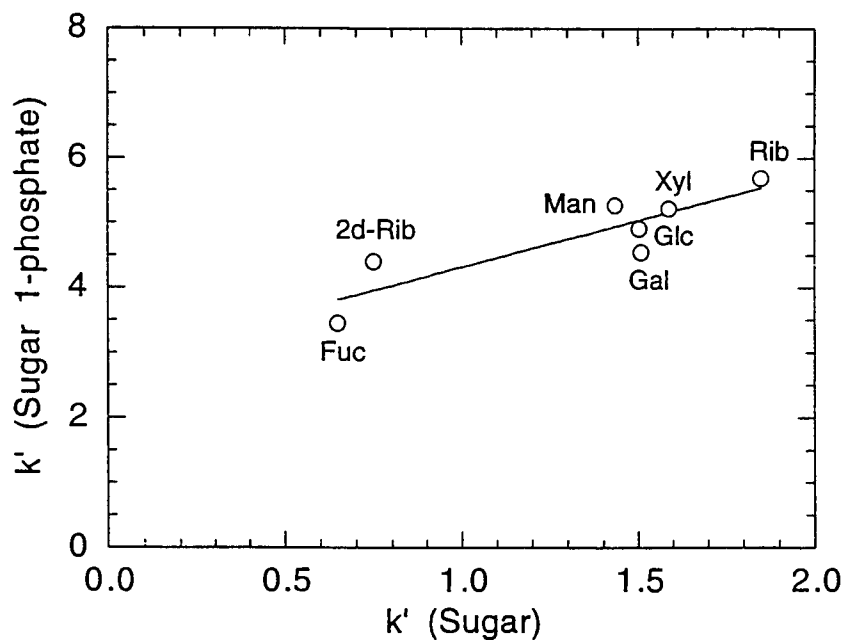


Fig. 2. Correlation of capacity factors of parent sugars eluted from a Dionex HPIC-AS6 column with 0.1 N NaOH with their corresponding α -1-phosphates eluted from a Dionex CarboPac PA1 column with 0.1 M NaOAc buffer at pH 6.0.

Effects of Salts on Subtilisin Crystallization

Xiaojing Pan and Charles E. Glatz

Department of Chemical Engineering, Iowa State University, Ames, IA 50011, USA

ABSTRACT

The effects of salts on crystallization of the protease ProperaseTM subtilisin were investigated. Three kinds of salt, NaCl, NaNO₃ and NaSCN were selected to study the effect of salts. The solubilities of ProperaseTM subtilisin in three kinds of salt solutions were measured. The effectiveness of salts in decreasing the solubility of protein followed the reverse order of the Hofmeister series: SCN⁻>NO₃⁻>Cl⁻. The average length and diameter of crystals were measured during crystallization, indicating the growth rate and the morphology of crystals changed with the nature of salts. The effects of salts on protein crystallization were related with the molar Gibbs energy of hydration of ions.

INTRODUCTION

Protein crystallization has been widely studied as a purification method and a prerequisite to determine 3D protein structure by X-ray diffraction. However, due to the complexity of protein, protein crystallization was not understood as well as crystallization of small inorganic molecules (Durbin and Feher, 1996). Many efforts have been performed for studying the nucleation and growth process of protein crystals so as to forming a general picture for protein crystallization.

Protein crystallization depends on many parameters, including pH, temperature, pressure and additives. All of these parameters can affect solubility of protein, nucleation and growth of protein crystals. Both the nature and the concentration of salts were found to affect the solubility of protein. Salting-in and salting-out are two common terms to describe the effect of salt concentration. With the addition of salts, the solubility of protein increases first and then decreases after passing through a maximum value (Timasheff and Fasman, 1969). The research on the effectiveness of various salts in salting-out proteins may be tracked back to the Hofmeister series established in 1888. The Hofmeister series ranked various salts according to their abilities to precipitate HEW protein.

- cations : Li⁺>Na⁺>K⁺>NH₄⁺>Mg²⁺
- anions: SO₄²⁻>HPO₄²⁻>CH₃COO⁻>C₆H₅O₇³⁻>C₃H₂O₅²⁻>HCO₃⁻>CrO₄²⁻>Cl⁻>NO₃⁻>>ClO₃⁻>SCN⁻

Later on, the Hofmeister series has been tested in crystallization of other proteins, e.g. lysozyme, α -amylase, hemoglobin, albumin (Veelster et al., 1996; Qasim et al., 1981; Ries-Kutt et al., 1989, 1991; Poillon et al., 1979). According to the isoelectric point of the protein and the pH condition for crystallization, these proteins can be divided into two groups. For acidic proteins in basic buffers, the effectiveness of various salts usually follows the Hofmeister series, except for the relative positions of some salts. However, for

basic proteins in acidic buffers, e.g. lysozyme, the cation series followed the Hofmeister series, but the anions influence solubility according to the reverse order of the Hofmeister series. Moreover, anions have more marked effects than cations for the basic proteins in acidic buffer (Ries-Kutt et al, 1991).

Research on the effects of salts on protein crystallization has been focused on solubility. Growth rate effects are rarely studied. The knowledge in this field is mainly based on the crystallization of small molecules. Salts mainly exert two kinds of effects on the growth rates of crystals: one is the thermodynamic effect, and the other is the kinetic effect (Zhang et al., 1996). When the thermodynamic effect is predominant (Mersmann, 1994), the addition of salts changes the solubility of the molecules of interest, changing the solution supersaturation and, hence, the growth rate of the crystals. It can be expected that the lower solubility is corresponding to the higher growth rate. On the other hand, when the kinetic effects outstrip the thermodynamic effects, the change of solubility becomes unimportant. The blocking of crystal surfaces may be the main factor (Zhang et al., 1996). It is hypothesized that ions may be incorporated into the lattice and ion-protein interactions compete with protein-protein interactions to decrease the growth rate of crystals.

During the crystallization process, hydrated protein molecules continuously diffuse from the bulk to the surfaces of crystals, and then are incorporated into the crystals after the water molecules in the hydration shell are released. Therefore, water molecules have an important role in protein crystallization. The purpose of current study was to determine how the nature of salt affects the growth rate of ProperaseTM subtilisin crystals. Since various salts have different hydration states, which may affect the protein crystallization, we will further investigate the role of water in protein crystallization.

MATERIALS AND METHODS

Materials

ProperaseTM subtilisin stored in stabilizing solution was provided by Genencor International. Before applied in our study, subtilisin was twice crystallized. Sodium acetate, sodium chloride, sodium nitrate and sodium thiocyanate were purchased from Fisher Scientific. The 10K OMEGA low protein-binding polyethersulphone membranes purchased from Pall Filtron were applied for diafiltration of protein. 0.22 μm cellulose acetate filters were obtained from Costar.

Diafiltration of protein stock solution

The stabilizers and formulation chemicals in protein stock solution were removed by 5 sequential diafiltrations with volumes of 10mM sodium acetate buffer (pH=5.5) equal to the sample volume, which was performed in an ultrafiltration cell. 10K OMEGA membranes were used to retain protein molecules. A transmembrane pressure of 15~20 psi was applied to the ultrafiltration cell.

Measurement of solubility

In order to reduce the time required to reaching solid-liquid equilibrium, the measurement of solubility was divided to two parts: the first part was to get crystal seeds and the second part was to reach solvation equilibrium.

First, the appropriate salt solution was mixed with the protein solution in sodium acetate buffer to get a protein solution with about 50mg/ml subtilisin and 0.5M salt. The protein solution was added in a 0.5ml microcentrifuge tube to produce seeds. After three days agitation, the supernatant and crystals were separated by centrifugation. The supernatant was decanted and the crystals were kept as seeds. Then, 0.5 ml stock solution with the same salt concentration and 30 mg/ml protein were added in the seed tube and allowed to crystallize for 2 weeks. After that, the concentration of supernatant was measured every week up to the point at which the value did not decrease any more. The final value was considered as the protein solubility. The protein concentration was measured by activity assay.

Single crystal growth study

A schematic diagram of the experimental procedure is given by Figure 1. All of experiments were conducted at room temperature and atmosphere pressure. After the diafiltration of protein stock solution, an appropriate amount of salt solution filtered through 0.22 μ m filter was added in the protein solution to initiate crystallization. The final salt concentration was 0.5M.

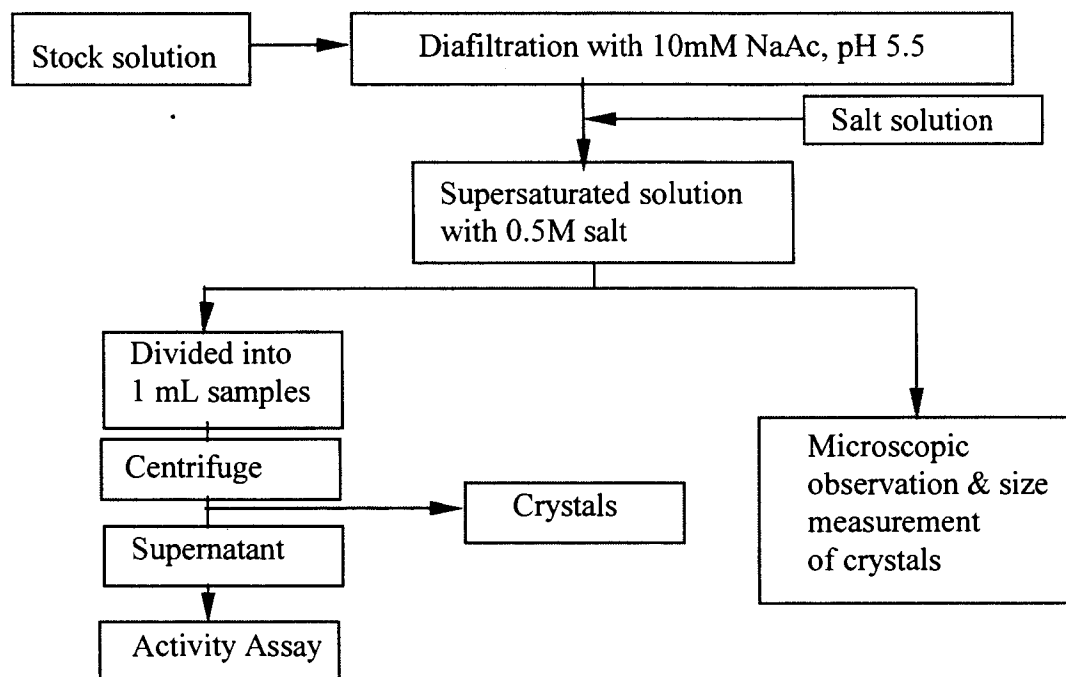


Figure 1: Schematic illustration of single crystal growth experiment

Three milliliter supersaturated protein solutions was placed in a Falcon plastic petri dish with a lid. The lid was sealed by PTFE thread seal tape and put under a Nikon

microscope (Optiphot-2, Fryer Company Inc., MN) for the whole experiment. The lengths and widths of crystal were measured by an image analysis system (Image-Pro Plus 4.0, Media Cybernetics, MD) connected to the microscope. The rest of the supersaturated solution was divided into 1ml samples for determining the concentration profile. The supernatant and crystals in each sample were separated by centrifugation. Activity assay was applied to determine the concentration of supernatant.

RESULTS AND DISCUSSION

1. Effects of salts on the solubility of ProperaseTM subtilisin

Figure 2 shows the solubility of ProperaseTM subtilisin in three kinds of salt solutions. Protein solubility in NaSCN solution is the lowest. There is no significant difference between the solubility of subtilisin in NaCl and NaNO₃ solutions. The effectiveness of the three anions on decreasing the solubility of subtilisin is $\text{SCN}^- > \text{NO}_3^- > \text{Cl}^-$. This order follows the reverse order of the Hofmeister series. Since the pI of subtilisin is around 10 and is larger than the pH value of crystallization solution (pH = 5.5), the current situation is that of a basic protein in an acidic buffer. The results obtained are consistent to the explanation proposed by Ries-Kutt et al. (1991).

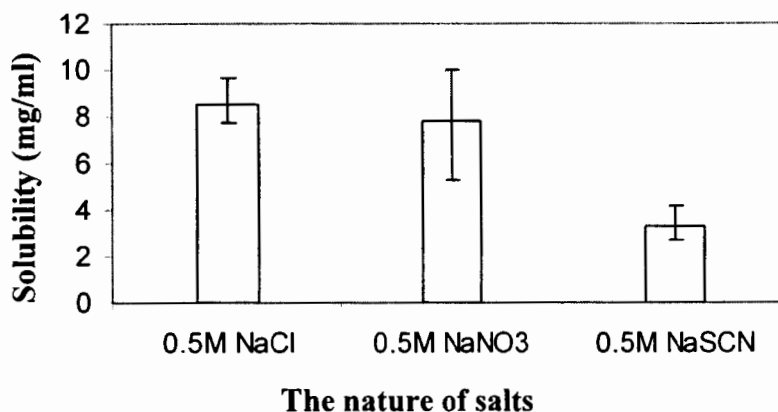


Figure 2: The solubility of ProperaseTM subtilisin in various salt solutions (buffer solution was 10mM NaAc with pH=5.5)

2. Effects of salts on growth rate of ProperaseTM subtilisin crystals

Pictures of ProperaseTM subtilisin crystals in various salt solutions are shown in Figure 3. These crystals have similar cross section but different L/D ration where L is the length of crystal and D is the equivalent diameter of the cross section. The L/D ration of subtilisin crystals in 0.5M NaCl, 0.5M NaNO₃ and 0.5M NaSCN were 3.1 ± 0.3 , 11.4 ± 1.7 and 34.5 ± 12.7 (95% confidence), respectively. During the growth process, it was also noted that the L/D ratio did not change with the size of crystals. The results showed the L/D ration increased according to the order of ions: $\text{Cl}^- < \text{NO}_3^- < \text{SCN}^-$. The change of the morphology of crystals in different salt solutions is mainly due to the change of the relative growth rates of different crystal faces.

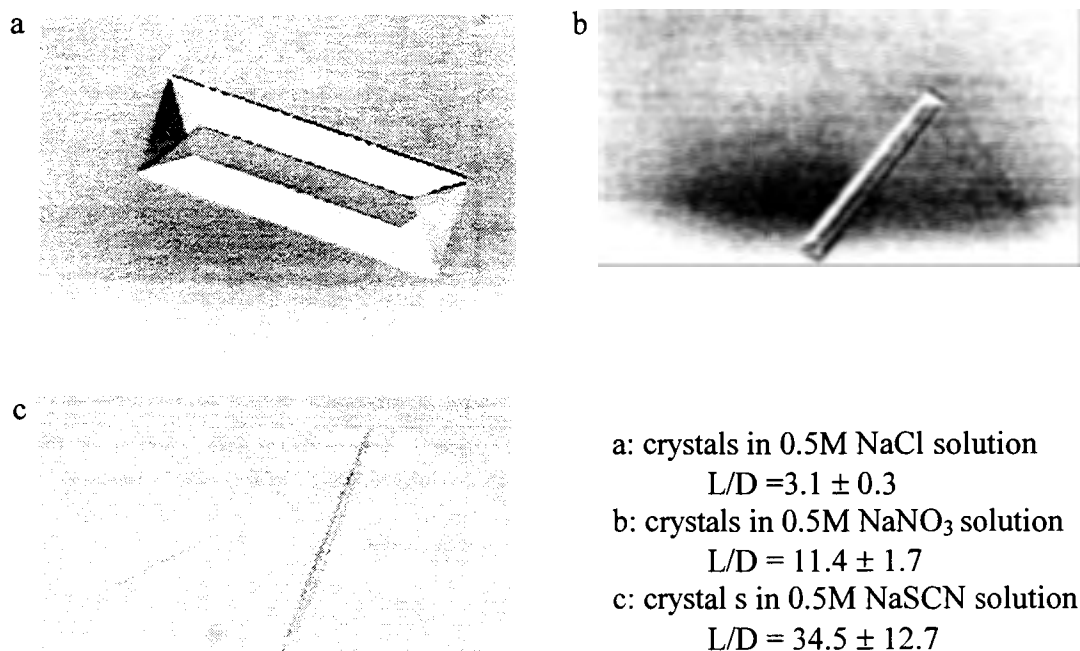


Figure 3: Pictures of Properase™ subtilisin crystals in various salt solutions.

Figure 4 shows the crystal growth curves of Properase™ subtilisin crystals in three kinds of salt solutions. By microscopy, it was noted that no new nuclei were observed after the measurable crystals emerged in a short time. So it was assumed that the crystals started to grow when the salt solution was added into the protein solution. Since the L/D ratio of crystals stays stable for the whole crystallization, the lengths of crystals are used to represent the sizes of crystals. The observation also showed the crystals grew with almost the same rate, which meant no significant growth dispersion in the growth process. The corresponding concentration profiles during the crystal growth are shown in Figure 5. With the growth of crystals, the protein concentration in solution decreases and approaches the protein solubility.

The average lengths of crystals were expressed as a function of time by fitting a Chebyshev polynomial function to the data of Figure 4. Differentiating the expression gave the growth rate (dL/dt) as a function of time. The corresponding dimensionless supersaturation $\frac{c-s}{s}$ was obtained from the concentration profile in Figure 5, where c is the concentration of supernatant and s is the solubility of protein. The curves of the growth rate vs. the dimensionless supersaturation in various salt solutions are plotted on a log-log scale in Figure 6. The figure shows the growth rate decreases with the decreasing supersaturation. The change trends of the growth rate with the supersaturation are similar in the three kinds of salt solutions, but the supersaturation required for the same growth rate increased following the order of $Cl^- < NO_3^- < SCN^-$.

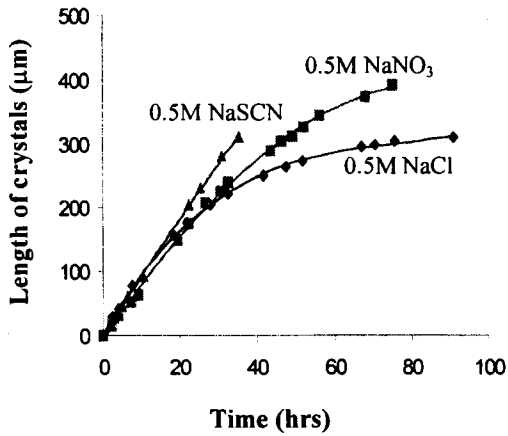


Figure 4: Single crystal growth curves in various salt solutions. (Buffer solution: 10mM NaAc, pH=5.5)

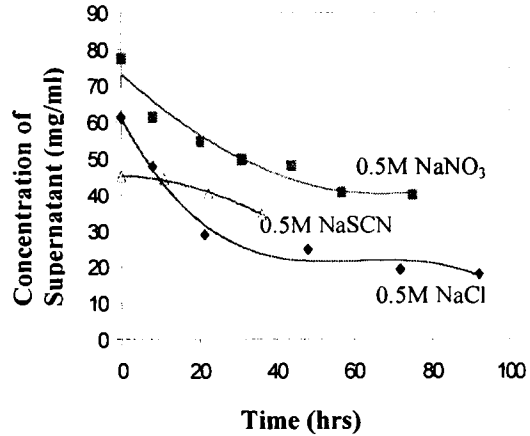


Figure 5: The concentration profiles of supernatants in single crystal growth experiments. (Buffer solution: 10mM NaAc, pH=5.5)

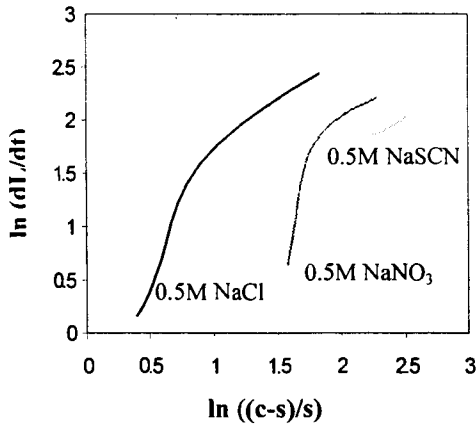


Figure 6: \ln (growth rate) vs. \ln (dimensionless supersaturation) calculated from the curve fit for the crystal lengths and the concentration profile vs. time

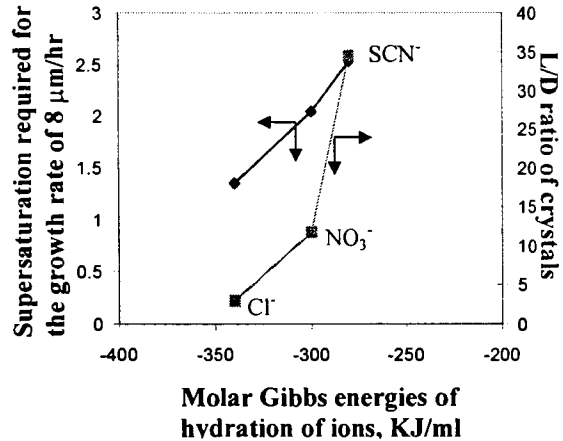


Figure 7: The correlation between the molar Gibbs energies of hydration of ions and the crystal growth of protein in various salt solutions

3. The correlation between the crystal growth of protein and the hydration of ions

When salts are added into protein solutions, water molecules will also form hydration shells around the ionized cations and anions. These ions compete with protein molecules for water molecules, which may affect protein crystallization. The correlation between the crystal growth of protein and the molar Gibbs energies of hydration of ions is shown in Figure 7. Different ions have different abilities to grasp water molecules, so their thermodynamic properties of hydration change with the nature of ions (Marcus, 1991, 1994). The molar Gibbs energies of hydration of anions increase in the order of Cl^- , NO_3^- and SCN^- , so the supersaturation required for the same growth rate and the L/D ratio of subtilisin crystals increased with the increasing molar Gibbs energy of hydration of ions.

Currently, only the apparent correlation between the hydration of ions and protein crystallization is observed, the underlying mechanism needs to be further investigated.

CONCLUSION

Effects of salts on subtilisin crystallization were investigated in our study. The following conclusions can be made:

- The solubility of Properase™ subtilisin in various salt solutions decreased in the order of NaCl, NaNO₃ and NaSCN, which follows the reverse order of the Hofmeister series.
- The morphology of crystals in various salt solutions changed due to the change of relative growth rates of different crystal faces. The length/diameter ratio of Properase™ subtilisin crystals increases with the order of NaCl, NaNO₃ and NaSCN
- Salts also affect the whole growth rate of protein crystals. The growth rate decreased in the order of NaCl, NaNO₃ and NaSCN. Supersaturation required for the same growth rate increases with molar Gibbs energy of hydration of ions

ACKNOWLEDEMENTS

The authors would like to thank NSF for funding this project and Todd Becker of Genencor International for the generous supply of subtilisin.

REFERENCE

- Bhargava, A. and P. Jelen, 1996. Lactose solubility and crystal growth as affected by mineral impurities. *J Food Science*, 61(1), 180-184.
- Durbin, S. and G. Feher 1996. Protein crystallization. *Annu. Rev. Phys. Chem.*, 47, 171-204.
- Genencor International Inc., U.S. patent "5,041,377" issued on Aug. 20, 1991.
- Marcus, Y., 1991. Thermodynamics of solvation of ions, part 5, Gibbs free energy of hydration at 298.15 K. *Journal of Chemical Society, Faraday Trans.*, 87(18), 2995-2999.
- Marcus, Y., 1994. A simple empirical model describing the thermodynamics of hydration of ions of widely varying charges, sizes and shapes. *Biophysical Chemistry*, 51, 111-127.
- Mersmann, A., 1994. *Crystallization technology handbook*. Marcel Dekker Inc., New York.
- Poillon, W. and J. Bertles, 1979. Deoxygenated sickle hemoglobin--effects of lyotropic salts on its solubility. *J Biol. Chem.*, 254, 3462-3467.
- Qasim, M. A. and A. Salahuddin, 1981. Influence of salts of Hofmeister series on the salting-out of bovine & buffalo serum albumins. *Indian J. Biochem Biophys*, 18, 393-397.
- Ries-Kutt, M. and A. Ducruix, 1989. Relative effectiveness of various ions on the solubility and crystal growth of lysozyme. *J Biol. Chem.*, 264, 745-748.

- Ries-Kautt, M. and A. Ducriux, 1991. Crystallization of basic protein by ion pairing. *J Crystal Growth*, 110, 20-25.
- Timasheff, S. and G. Fasman, 1969. *Structure and stability of biological macromolecules*. Marcel Dekker Inc., New York, 417-575.
- Veelser, S., A. Lafont, S. Marcq, J.P. Astier and R. Boistelle, 1996. Prenucleation, crystal growth and polymorphism of some proteins. *J Crystal Growth*, 168, 124-129.
- Zhang, S., J. Yuan, H.A. Mohameed and J. Clrich, 1996. The effect of different inorganic salts on the growth rate of NaCl crystallized from sea water. *Cryst. Res. Technolo.*, 31, 19-25.

A Microcosm Study on Biodegradation of Methyl tert-butyl Ether (MTBE)

Qizhi Zhang¹, Lawrence C. Davis², Larry E. Erickson¹

¹*Dept. of Chem. Eng., Kansas State University, Manhattan, KS 66506, Phone: (785)532-5584, FAX: (785)532-7372,* ²*Dept. of Biochemistry, Kansas State University, Manhattan, KS 66506, Phone: (785)532-6124, FAX: (785)532-7278*

Abstract

A microcosm study was performed to evaluate the possible biodegradation of methyl tert-butyl ether (MTBE) by both introduced and/or indigenous microorganisms in soils. Microcosms were prepared using 125 ml serum bottles. Each bottle contained 5 g of soil and 20 ml of Basal Salt Medium (BSM) solution with MTBE concentration of 0.84 mM (millimoles per liter). The soil was taken from an experimental soil channel system that had been contaminated with MTBE for more than half of a year. The microcosms were incubated for 165 days at room temperature. The incubation process was monitored by analyzing the headspace of each bottle for MTBE, CO₂, and O₂ concentrations. Slight decline of MTBE concentration in the headspaces indicated slow biodegradation of MTBE. More CO₂ was produced and more O₂ was consumed for all the soil microcosms than for the control. Some of the produced CO₂ appeared to be formed from organic matter in the soil and part of the O₂ consumed appeared to be incorporated into biomass or other products.

Keywords: MTBE, biodegradation, microcosm, microorganism

Introduction

Methyl tert-butyl ether (MTBE) is one of the two oxygenates (ethanol and MTBE) required for use in 1992 under the Clean Air Act Amendments program for areas that exceeded federal carbon monoxide standards in the winter. The increase in molecular oxygen for fuels containing oxygenates results in fewer products of incomplete combustion, which are responsible for many problems in urban air quality.

The substantial use of fuels with oxygenates has made MTBE an important groundwater contaminant. Reformulated gasoline is about 50 times more soluble in water than conventional gasoline. Because MTBE does not bind well to soil (its organic carbon-based partition coefficient [K_{oc}] is 12.3 cm³/g) and is highly soluble in water (water solubility equals to 52,160 mg/L), it can migrate with groundwater rapidly (EPA, 1998). The result is that accidental spills of gasoline containing MTBE or leaks from storage tanks can pose a hazard to groundwater supplies.

Microorganisms break down compounds to more simple species and thereby extract energy required for their growth and metabolism. MTBE's poor biodegradability has been generally supported by laboratory testing of anaerobic biodegradation (Sufliata and Mormile, 1993) and by both bench- and field-scale tests of aerobic biodegradation (API, 1994). Having studied the degradability of a number of fuel additives, Sufliata and Mormile (1993) suggested that the chemical structure of these compounds greatly affect their susceptibility to biological decay. Compounds that contain a tertiary or quaternary carbon atom, like MTBE, are far more recalcitrant than other unbranched or moderately branched chemicals.

However, there is still substantial evidence that suggests that MTBE can biodegrade under well-controlled conditions. Biodegradation of MTBE by pure or mixed bacterial cultures has been reported in several laboratory studies (Mo et al., 1995; Mo et al. 1996, Mo et al. 1997; and Yeh and Novak 1994). Yeh and Novak (1994) observed degradation of MTBE for microcosms made with organically poor soil under methanogenic conditions and with nutrient amendments added. They hypothesized that the first and rate-limiting step in MTBE degradation may be cleavage of the ether bond. Daniel and Borden (1997) conducted laboratory microcosm studies under aerobic and denitrifying conditions and a field-scale investigation. They reported similar patterns of biodegradation of BTEX and MTBE. That is, biodegradation rates were higher near the contaminant source and lower further downgradient (Daniel and Borden, 1997).

A research group at university of Notre Dame (Mo et al., 1995; Mo et al. 1996 and Mo et al. 1997) isolated fifteen pure bacterial strains with the capacity to degrade MTBE when it was the sole carbon source. The enrichment cultures were developed from activated sludges and soil acquired from Amoco Corporation (Naperville, IL, USA), and soil near a ginkgo tree and fruit of the same ginkgo tree. These strains degraded up to 40% of 200 ppm of MTBE in 1~2 weeks of incubation at 22~25°C. They also developed a mixed culture in bioreactors using MTBE as sole carbon source for over one year. The mixed culture degraded 160 ppm of MTBE after three days incubation in batch experiments and showed greater capability for degradation of MTBE than pure cultures.

A review (Zhang et al., 1998) of recent studies of biodegradation of MTBE indicated that no published work was found regarding the biodegradation of MTBE by indigenous microorganisms associated with plants. It was mentioned in one review article on phytoremediation (Newman et al., 1998) that MTBE was metabolized by poplar cell cultures, and that eucalyptus trees were capable of taking up MTBE under laboratory conditions.

An experimental channel system study (Zhang et al., 1999) investigated the fate and transport of MTBE in groundwater under vegetation conditions. Two bacteria strains (*Rhodococcus* and *Arthrobacter*) obtained from the Notre Dame group were introduced into four channels planted with alfalfa. The total mass balance on MTBE for a six-month monitoring period showed that the fractions of MTBE which were not recovered in all the planted channels ranged from 12% to 28% while full recovery was observed in the unplanted channel. The four vegetated channels with introduced bacteria had less MTBE

recovered from the soil surface than another channel which was vegetated but without any introduced bacterium.

In order to distinguish the effects of soil microorganisms and the presence of plants on the loss of MTBE within the soil channel system, this study was conducted. The primary focus was to determine if microorganisms present in the soil channels degraded MTBE and, if so, to evaluate MTBE degradation kinetics.

Materials and Methods

Microcosms were prepared to investigate the effects of both the indigenous and the introduced bacteria on MTBE decay. Serum bottles with volume of 125 mL with rubber stoppers were used to contain the soil/water microcosms, allowing for gas sampling from the headspace.

The top 12 cm of soils from six channels were sampled, weighed and added to the serum bottles. The channels had been contaminated with MTBE for more than one and half years. Channels 1, 2, 3, 5 and 6 were planted. Channels 1 and 2 had been inoculated with strain *Rhodococcus* and channels 5 and 6 with strain *Arthrobacter* seven months ago.

Each serum bottle was sealed with rubber stopper after 5 g soil (wet weight) and 20 mL of BSM (Basal Salt Medium) solution spiked with MTBE at 100 μL MTBE/L were added. Triplicates were made with every soil sample. Two controls were prepared, with one using soil autoclaved at 17 psi and 246.2 $^{\circ}\text{F}$ for 30 minutes and another having only the 20 mL of BSM solution spiked with MTBE at 100 μL MTBE/L.

Substrate (MTBE) disappearance, carbon dioxide production and oxygen consumption was monitored by sampling the headspace of the microcosms; samples were analyzed using gas chromatograph equipped with a flame ionization detector. The headspace of each bottle was sampled immediately after preparation, and periodically at 10-day intervals.

Results and Discussion

To estimate the volume of the 5g soil, a bulk density of wet soil of 1.25 g/mL was assumed. So the volume of 5g soil became 4 mL. The headspace volume in each serum bottle turned out to be: $(125 - 20 - 4) = 101$ mL. Initially available oxygen in each bottle headspace was $101 \text{ mL} \times 21\% = 21.2$ mL which was 8.68×10^{-4} moles of oxygen under 1atm, 298 $^{\circ}\text{K}$. On the 92nd day of the incubation 20 ml pure O_2 was added into each serum bottle to make up for the depleted oxygen in the microcosm headspaces. As a result, the total amount of oxygen entering each microcosm became $21.2 \text{ mL} + 20 \text{ mL} = 41.2$ mL, which is equal to 1.69×10^{-3} moles of oxygen under 1atm, 298 $^{\circ}\text{K}$.

The carbon fraction and degree of reduction of MTBE (C₅H₁₂O) are as follows:

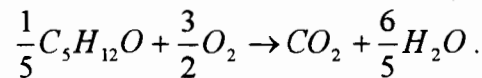
$$\sigma_{MTBE} = \frac{5 * 12}{88} = 0.682$$

$$\gamma_{MTBE} = \frac{5 * 4 + 12 * 1 + 1 * (-2)}{5} = 6.0$$

Initial MTBE concentration in the BSM solution was:

$$\frac{100 \mu L}{1LH_2O} = \frac{0.1mL * 0.74 g / mL}{1LH_2O} = 74 ppm = 0.84 mM$$

If MTBE was completely mineralized, we would have



For every mole of MTBE mineralized, 7.5 moles of oxygen are needed and 5 moles of CO₂ are produced. In the 20 mL BSM solution, there was 0.84 mM x 20 mL = 1.68 x 10⁻⁵ moles of MTBE. Thus the maximum amount of oxygen required to completely mineralize 1.68 x 10⁻⁵ moles of MTBE should be 1.68 x 10⁻⁵ x 7.5 = 1.26 x 10⁻⁴ moles. That is, for 1.68 x 10⁻⁵ moles of MTBE to be completely mineralized, 14.5% of the 8.68 x 10⁻⁴ moles of O₂ would be used and 1.68 x 10⁻⁵ x 5 = 8.40 x 10⁻⁵ moles of CO₂ would be produced. Under 1 atm and 298°K, 8.40 x 10⁻⁵ moles of CO₂ equals to 2.05 mL in volume, which is 2.05 mL/101 mL = 2.03% of the headspace volume.

Figure 1 shows the MTBE disappearance profiles over incubation time for microcosms made of soil taken from six different soil channels and for the autoclaved microcosm control. Compared with the control, slightly more MTBE disappearance was observed. The biodegradation of MTBE in soil microcosms was not significant. Figures 2 and 3 demonstrate the CO₂ production and O₂ consumption as a function of incubation time. Obviously more CO₂ was produced and more oxygen was consumed in all the soil microcosms than in the control.

As we can see from the curves, MTBE concentration decreased slowly. Assuming 20% of MTBE disappeared after the 165 days of incubation, the CO₂ produced from MTBE would be 1.68 x 10⁻⁵ moles, and O₂ consumption should be 2.52 x 10⁻⁵ moles. However, from the previous figures, we measured approximately 6.61 x 10⁻⁴ moles (16%) of CO₂ and as low as 1.12 x 10⁻⁴ moles (2.7%) of O₂ remained. So the amount of oxygen dissipated equaled to (1.69 x 10⁻³ - 1.12 x 10⁻⁴) moles. In other words, up to 1.58

$\times 10^{-3}$ moles of O_2 was used. Both CO_2 production and O_2 consumption were much higher than that required for the MTBE that disappeared to be completely mineralized.

The organic matter of the soils was measured to be 0.7~1.3%. Assuming half of the organic matter is carbon, we can estimate that, among the 5g of soil, there was 17.5~32.5mg (1.46~2.71 mmoles) of carbon. To completely oxidize all of the organic carbon, the same number of moles of oxygen is needed and the same number of moles of CO_2 will be produced. This number is significantly larger than the produced amount of CO_2 and the consumed amount of O_2 . Thus, most of the CO_2 must be formed from the soil organic matter and part of the O_2 consumed appeared to be incorporated into biomass or other products. Depending on alkalinity of the soil and buffering capacity, some CO_2 might remain in the soil solution also.

Results from plating soil suspensions made from soil samples from the microcosms indicated the presence of at least three different colony morphologies. Number of colonies increased from 10^7 /mL before the incubation to 10^9 /mL after 178 days of incubation. More microbiological work is needed to track the population of the microorganisms, to examine culture identities and identify any pure culture(s) capable of using MTBE as a single carbon and energy source.

Conclusion

Disappearance of MTBE, consumption of O_2 and production of CO_2 were observed from all the microcosms, including the control. Most of the produced CO_2 must be formed from organic matter in the soil and part of the O_2 consumed might be incorporated into biomass or other products. In order to evaluate the kinetics of MTBE degradation, more work needs to be done to quantify the impact of soil organic carbon, and to monitor the characteristic degradation products of MTBE including tert-butyl alcohol, tert-butyl formate, tert-amyl alcohol, and carbon dioxide.

Acknowledgements

This article has been funded in part by the U.S. Environmental Protection Agency under assistance agreements R-819563, R-825549 and R-825550 through the Great Plains/Rocky Mountain Hazardous Substance Research Center for regions 7 and 8 under project 94-27. It has not been subjected to the EPA for peer and administrative review and, therefore, may not necessarily reflect views of the agency and no official endorsement should be inferred. The Center for Hazardous Substance Research also provided partial funding.

References

- American Petroleum Institute, 1994. Transport and fate of dissolved methanol, methyl-tertiary-butyl-ether, and monoaromatic hydrocarbons in a shallow sand aquifer, *API Publication 4601*.
- Damera, R., M.R. Hill and D. Murali, 1997. Rapid clean-up of a multiple fuel spill. in *In Situ and On-Site Bioremediation*, Alleman, B.C. and A. Leeson (Eds.), Battelle Press, Columbus, Ohio. **1**, p. 199.
- Daniel, R.A. and R.C. Borden, 1997. Spatial variability in intrinsic bioremediation rates: Effect on contaminant transport. in *In Situ and On-Site Bioremediation*, Alleman, B.C. and A. Leeson, (Eds.), Battelle Press, Columbus, Ohio; **1**, p. 29.
- EPA 510-F-97-015, 1998. Remediation of MTBE contaminated soil and groundwater. *MTBE Fact Sheet #2*. Jan. 1998, p. 1-5.
- Mo, K., C.O. Lora, A.E. Wanken and M. Javanmardian, 1997. Biodegradation of methyl t-butyl ether by pure bacterial cultures. *Appl. Microbiol. Biotechnol.* **47**, p. 68-72.
- Mo, K., C. Lora, A. Wanken and C.F. Kulpa, 1995. Biodegradation of methyl-t-butyl ether by pure bacterial cultures. Presented at American Society for Microbiology meeting, 1995, Washington, D.C.: <http://www.nd.edu/~cbpc/kulpa3.html>.
- Mo, K. C. Lora, M. Javanmardian, X. Yang and C.F. Kulpa, 1996. Biodegradation of gasoline oxygenate, methyl-t-butyl by mixed and pure cultures. Presented at American Society for Microbiology meeting, 1996, New Orleans, LA: <http://www.nd.edu/~cbpc/kulpa3.html>.
- Newman L. A., S. L. Doty, K. L. Gery, P. E. Heilman, I. Muiznieks, T. Q. Shang, S. T. Siemieniec, S. E. Strand, X. Wang, A. M. Wilson, and M. P. Gordon, 1998. Phytoremediation of organic contaminants: A review of phytoremediation research at the University of Washington. *Journal of Soil Contamination*, **7**(4), p. 531-542.
- Squillace, P.J., J.S. Zogorski, W.G. Wilber, and C.V. Price, 1996. Preliminary assessment of the occurrence and possible sources of MTBE in groundwater in the United States, 1993-1994. *Environ. Sci. Technol.*, **30**(5), p. 1721-1730.
- Suflita, J.M. and M.R. Mormile, 1993. Anaerobic biodegradation of known and potential gasoline oxygenates in the terrestrial subsurface, *Environ. Sci. & Technol.*, **23**(5), p. 976-978.
- Yeh, C.K., and J.T. Novak, 1994. Anaerobic biodegradation of gasoline oxygenates in soils. *Water Environment Research*, **66**(5), p. 744-752.
- Zhang, Q., L. C. Davis and L. E. Erickson, 1998. Biodegradation and remediation of methyl tert-butyl ether. *Proceedings of the 28th Annual Biochemical Engineering Conference*, Iowa State University, Ames, Iowa, p. 23-32.
- Zhang, Q., L. C. Davis and L. E. Erickson, 1999. An experimental study of phytoremediation of methyl tert-butyl ether (MTBE) in groundwater. *Proceedings of the 14th Annual Conference on Hazardous Waste Research*, St. Louis, MO, in press.

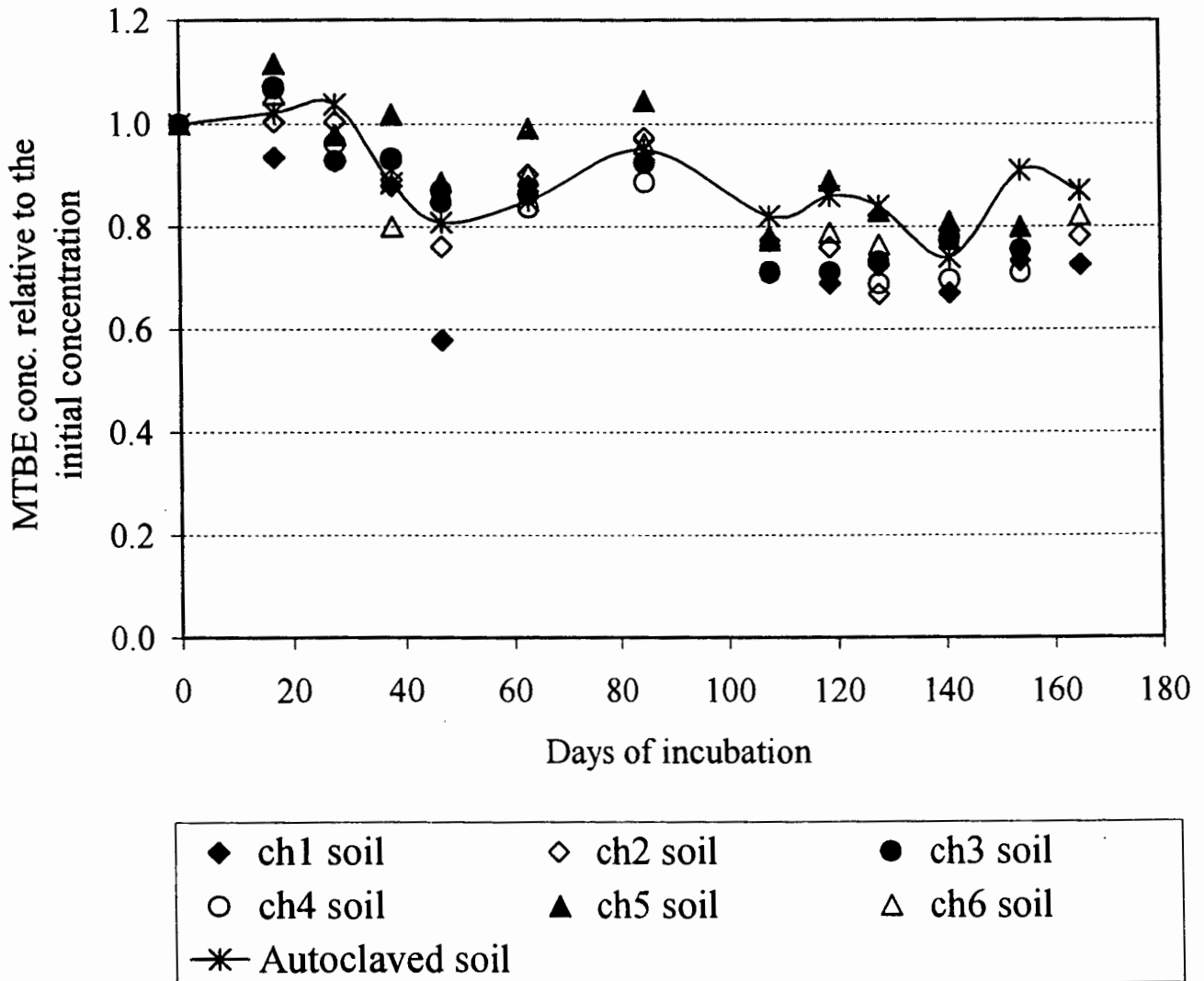


Figure 1. MTBE headspace concentration profile of microcosms with soils from each of the six channels.

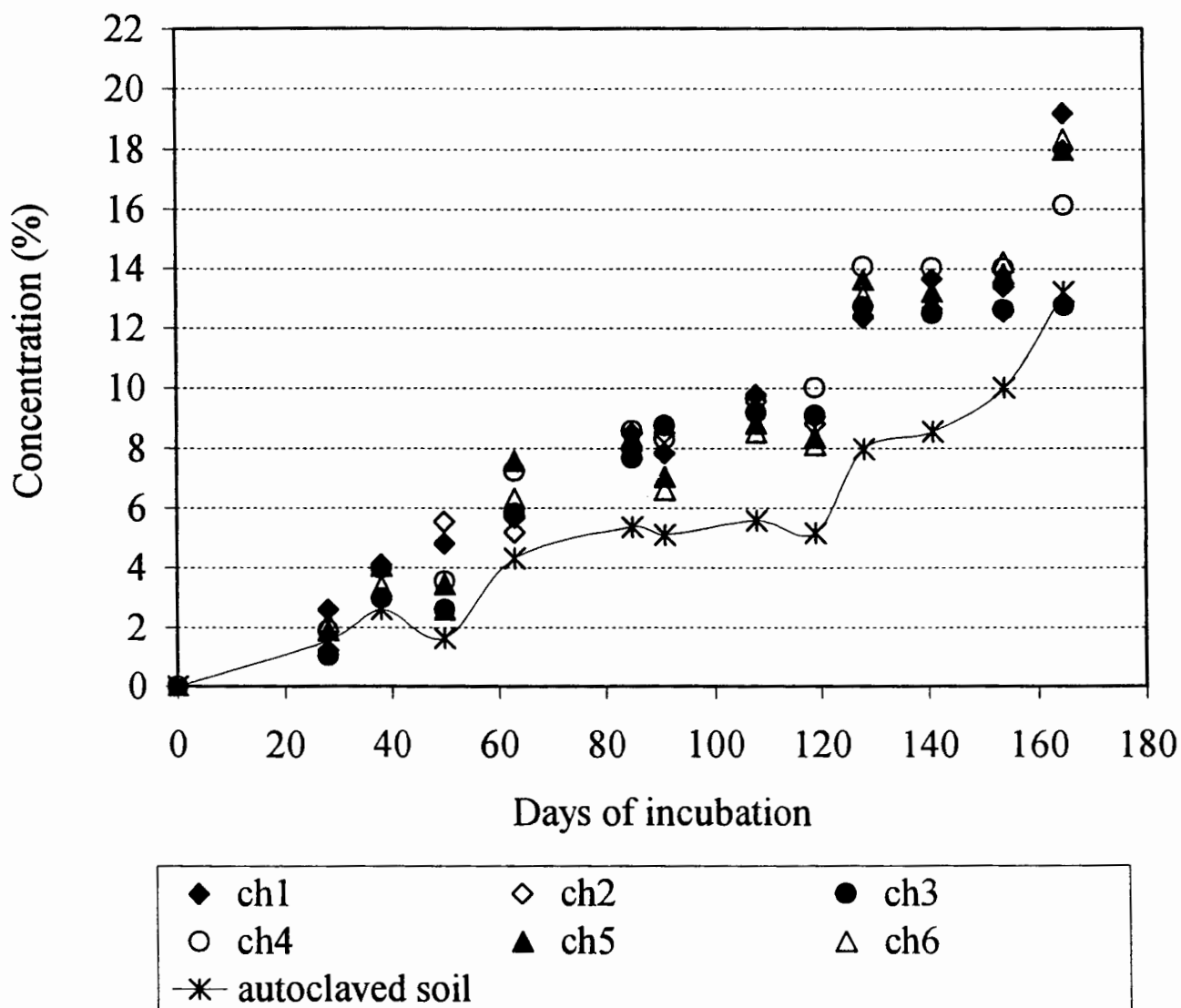


Figure 2. Concentration of CO₂ in the headspace of the microcosms.

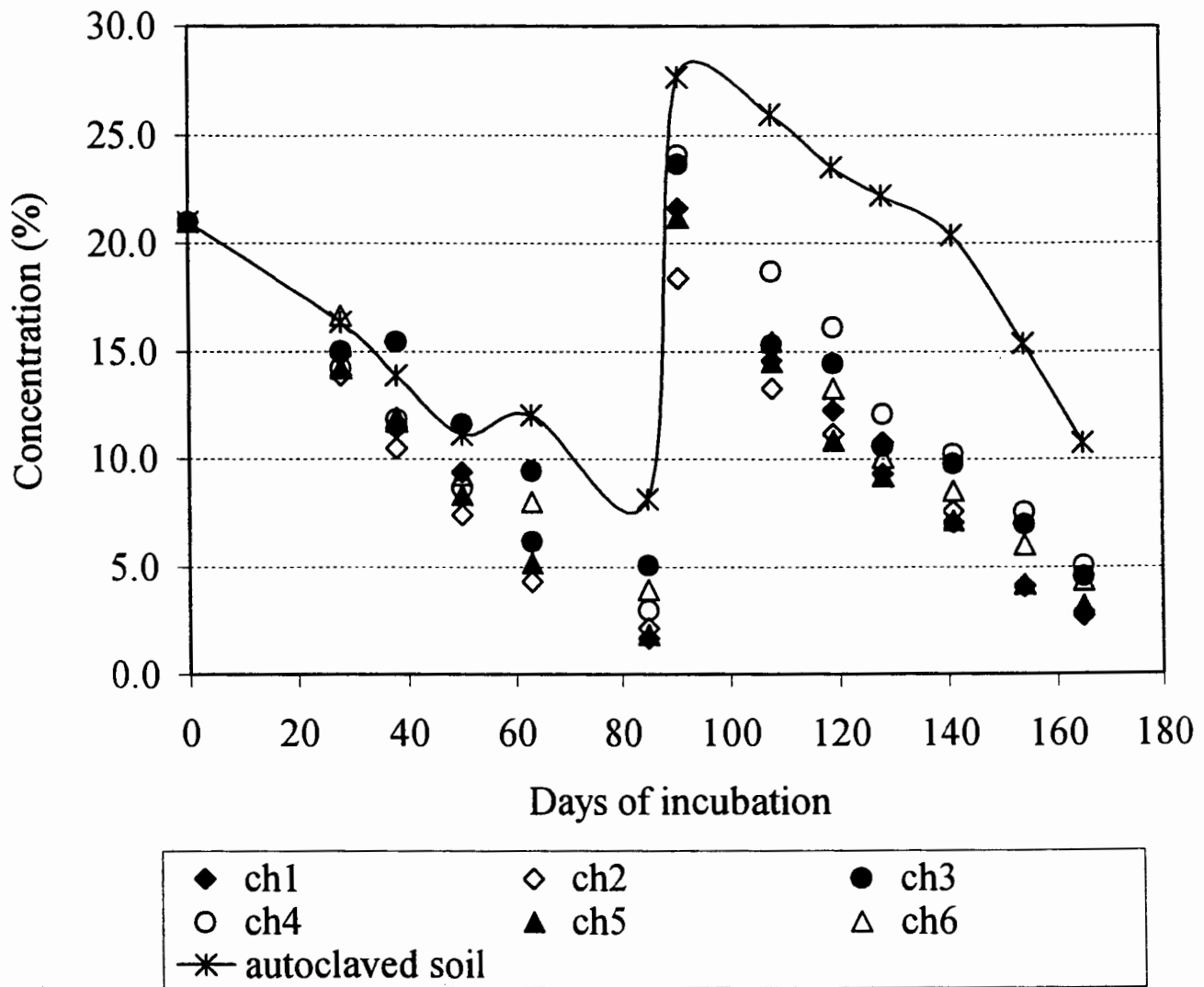


Figure 3. Concentration of O₂ in the headspace of the microcosms from all six channels, compared with that of the autoclaved soil. Pure oxygen was added after 92 days.

TRANSPORT OF ORGANIC CHEMICALS THROUGH LIVING PLANT TISSUES

¹L.C. Davis, ²D. Lupher, ²Q. Zhang ²J. Hu and ²L.E. Erickson

¹*Department of Biochemistry, Willard Hall, Kansas State University, Manhattan, KS 66506; Phone: (785) 532-6124; Fax: (785) 532-7278.* ²*Department of Chemical Engineering, Durland Hall, Kansas State University, Manhattan, KS 66506; Phone: (785) 532-4313; Fax: (785) 532-7372.*

INTRODUCTION

There is much interest in the possible intermedia transfer of contaminants from water/soil to air via plants. Burken and Schnoor (1997) showed that a predictive relationship based on the octanol:water partition coefficient could account for transfer of a number of contaminants through small poplar trees. Recently Vroblesky et al (1999) measured chlorinated ethenes within the trunks of mature trees growing on contaminated soil at the Savannah River site. We have shown that transfer of chlorinated solvents which occurs with several species of plants including poplars, willows and sunflowers (Davis et al 1998), is generally in agreement with the work of Burken and Schnoor (1997). Recent studies by Hu in this laboratory (Hu, 1999) have extended this work to include measurement of sorption to plant tissues, and estimation of the radial diffusivity of contaminants while moving through the stem of a plant. More detailed measurements and analyses are presented here.

MATERIALS AND METHODS

Vigorously growing, hydroponically cultured poplar or corkscrew willow trees of about 50 g fresh weight with a water usage of 5 - 10 mL/hr were exposed to low concentrations ($\sim 10 \mu\text{M}$) of trichloroethylene (TCE). After 1-2 days exposure time, the plants were dissected from the top down, rapidly transferring 1-2 g pieces of stem to 65 mL bottles which were closed with mininert valves. At intervals, or after long-term equilibration, samples were analyzed by gas chromatography. Fresh and dry weights were determined for the plant segments. From these data, a profile of the TCE distribution within the plant could be derived.

Assuming steady state transport, knowing the water usage (mL/hr) and stem cross section (cm^2), one can calculate the linear superficial velocity (cm/hr) of water from the stem base to any point within the stem below the leaves. The transit time through a given segment distance, derived from the linear velocity, assumes that the entire aqueous content of a stem segment is in equilibrium. Actual water content varied from 55-75%; for convenience a value of 66% was used in calculations. The plants used for these experiments had multiple shoots arising from upper portions of the stem. So for estimating water fluxes within these shoots it had to be assumed that water transport was proportional to the relative cross-section of each shoot. When there were leaves on the shoot section being analyzed, it had to be assumed that the leaves on that segment and below it, used only a small portion of the total water. More than 3/4 of the leaves were located above the sections analyzed.

During the winter dormancy period, long stem segments were removed from hybrid poplar trees and either used immediately or stored for a few days under refrigeration. The stem segments were immersed in a large volume (13 L) of water

containing a low concentration of TCE (~13 μM). At intervals the stems were removed, blotted briefly, and snipped into pieces which were treated and analyzed as above. End segments concentrations were discarded from the analysis to avoid end effects. This provided a measure of the inward diffusion rate of TCE into the plant tissue.

To estimate the outward diffusivity of TCE, stem segments (25-30 cm long) were immersed in the same conditions for 3 days and then removed, blotted briefly and placed into a large (0.97 or 1.3 L) bottle. Short pieces of the stem ends were cut off for separate analysis in smaller bottles sealed with mininert valves. Gas samples were withdrawn at intervals up to 24 hr to measure the outward diffusive flux of TCE.

Results from the influx or efflux experiments were plotted as log functions to derive a slope for the 1st order transfer process, from which a half-time could be estimated. Knowing the dimensions of the stem segments it is possible to calculate a diffusivity assuming a uniform cylindrical shape and composition. This is derived from the relationship given by Rose (1981) where the characteristic of the half-time for the entire cylinder is $0.0631 = Dt_{1/2}/r^2$.

The same relationship given above can be used to estimate a diffusivity for the data acquired with actively transpiring plants if one assumes that the linear velocity of water flow is a function of cross sectional area and volume transported per unit time. As a simple approximation, assuming a steady state flow and sorption equilibrium, the concentration decrease, as the water moves up the stem, is due entirely to radial diffusive losses during that movement. Knowing the radial dimension of the stem and the transit time between two points one can use the observed concentration decrease to predict a diffusivity in the radial direction.

RESULTS AND DISCUSSION

Table 1 shows calculated diffusivities for stem segments taken from two intact, actively transpiring willow trees and two poplar trees. In each case, stems were cut into segments for analysis and the results were graphed as concentration of TCE in $\mu\text{g/g}$ dry weight of stem tissue. A best visual fit to the change of concentration as a function of distance along the stem was determined, to estimate the change in relative concentration along a portion of the stem represented by several segments. Details are given in the M.S. thesis of J. Hu (1998). Assuming that the radius of the stem does not change appreciably over the interval being analyzed, and knowing the water usage by the plant, it is possible to calculate the linear velocity of water within the plant stem and hence the mean residence time of a packet of water moving from the base toward the top. The diffusive loss outward was assumed to be equivalent to the diffusive loss which would occur if a stem segment of the same cylindrical cross section were exposed to uncontaminated air during a static incubation, as described by Rose (1981). If the radius decreases over a long interval of stem length, the estimated diffusivity will be somewhat misestimated by this procedure, depending on what is chosen as a best estimate of the average radius.

The experimental data of Vroblesky et al. (1999) was analyzed using the method of Rose (1981) and reasonable estimates of the linear velocity of water and the diameter of the tree. This exercise yielded estimates of diffusivity which are in agreement with those in Table 1.

The results of the inward diffusion and outward diffusion with stems immersed in

contaminated solution are presented in Davis et al. (1999). The values of diffusivity were smaller in this case; they ranged from 3×10^{-7} cm²/s to 9.5×10^{-7} cm²/s. The smaller values may be associated with soaking the stems and the reduction of gas void space in the stems.

Figure 1 shows a typical efflux experiment, using a stem segment from a mature, dormant tree, in this instance for a peeled stem. The line shown is from a 1st order regression based on a log plot of the data. In all experiments there was a very rapid release of 10-20% of the total amount contained in the stem; this was presumably the result of a thin layer of trapped solution on the surface of the stem. Because the stems used for these studies had matured in the autumn and dropped their leaves, they may not have a permeability comparable to that of actively growing shoots examined above, which generally were green, more succulent and presumably metabolically active.

TCE and DCE pass relatively quickly through stems in the radial direction (Davis et al., 1999). The loss can be measured in intact plants. This loss has important implications for any study of the intermedia transfer of TCE or other volatile organics from soil to atmosphere. One must monitor not only the transpiration of water by the plant but also the loss to the atmosphere surrounding the stems, particularly for the smaller stems near the newly growing, leafy portions of the tree or other plant. Since these compounds also diffuse through roots, contaminants which are transported up into the unsaturated soil by plants may also be lost to the soil gas and be released to the atmosphere at the soil surface (Hu, 1998).

ACKNOWLEDGMENTS

This article has been funded in part by the U.S. Environmental Protection Agency under assistance agreements R-819563, R-825549 and R-825550 through the Great Plains/Rocky Mountain Hazardous Substance Research Center for regions 7 and 8 under project 94-27. It has not been subjected to the EPA for peer and administrative review and, therefore, may not necessarily reflect views of the agency and no official endorsement should be inferred. The Center for Hazardous Substance Research also provided partial funding.

REFERENCES

- Bird, R.B., W.E. Stewart and E.N. Lightfoot, 1960. *Transport Phenomena*, John Wiley and Sons, New York. p 548
- Burken, J.G. and J.L. Schnoor, 1998. Predictive relationships for uptake of organic contaminants by hybrid poplar trees, *Environ. Sci. Technol.*, 32 pp 3379-3385
- Davis, L.C., S. Vanderhoof, J. Dana, K. Selk, K. Smith, B. Goplen and L.E. Erickson, 1998. Chlorinated solvent movement through plants monitored by Fourier transform infrared (FT-IR) spectrometry, *Journal of Hazardous Substance Research* Vol 1 # 4, pp 1-26
- Davis, L.C., D.A. Luper, J. Hu, and L.E. Erickson, 1999. Transport of trichloroethylene through living plant tissues, *Proceedings of the Fourteenth Annual Conference on Hazardous Waste Research*, In Press.

Hu, J., 1998. Study on fate and transport of contaminants in plants,
M.S. Thesis, Kansas State University, Dept. of Chemical Engg., Manhattan, KS

D.A. Rose, 1981. Gas exchange in leaves, in *Mathematics and Plant Physiology*, D.A.
Rose and D.A. Charles-Edwards eds. Academic Press pp 67-78

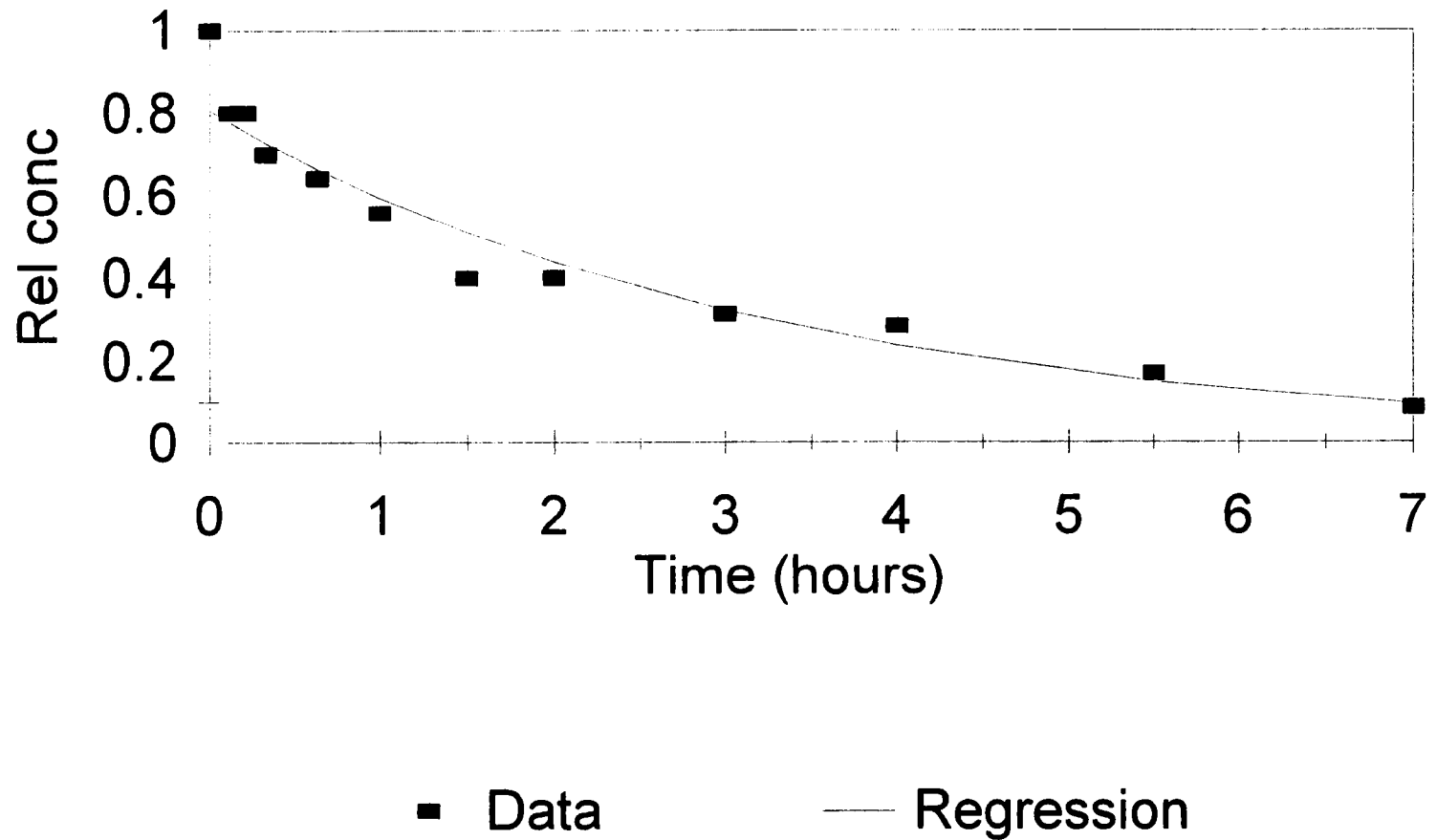
Vroblesky, D.A., C.T. Nietsch and J.T. Morris, 1999. Chlorinated ethenes from
groundwater in tree trunks, *Environ. Sci. Technol.* 33 pp 510-515

Table 1. Transfer and loss of TCE in intact poplar and willow trees

Plant part	Radius (cm)	Interval (cm)	Linear velocity (cm/hr)	Transit time (hr)	Loss (%)	Diffusivity ($\times 10^{-6}$ cm ² /sec)	Water use & time
Poplar #1 stem	0.34	9	45	0.2	35	>3	268 mL/25 hr
branch 1	0.19	25	68	0.37	50	2	
branch 2	0.16	26	68	0.38	62	1.5	
branch 3	0.12	15	68	0.22	85	3	
Poplar #2 stem	0.31	7	35	0.2	10	3	299 mL/42 hr
branch 3	0.2	15	30	0.49	34	1	
Willow #1 stem	0.5	22	8.5	2.59	62	3	211 mL/48 hr
branch	0.2	39	54	0.72	38	2	
Willow #2 stem	0.35	10	36	0.28	14	1.5	383 mL/42 hr
branch 1	0.2	14	55	0.25	52	3	
branch 2	0.2	19	55	0.35	56	2.5	

Poplar # 1, 40 g fresh wt, used 268 mL in 25 hr; poplar # 2, 55 g fresh wt, used 299 mL in 42 hr;
willow # 1, 60 g fresh wt, used 211 mL in 48 hr; willow # 4, 50 g fresh wt, used 383 mL in 42 hr.

Figure 1: Relative concentration of TCE in poplar stem w/o bark vs. time



Intracellular Calcium Response of Endothelial Cells Exposed to Flow in the Presence of Thrombin or Histamine

Laura M. Worthen, M.S. and Matthias U. Nollert, Ph.D.

**School of Chemical Engineering and Materials Science
University of Oklahoma
100 E. Boyd St., Energy Center
Norman OK 73019**

Abstract

We investigated the role of intracellular Ca^{2+} increases as a part of the shear stress signal transduction cascade. Primary human umbilical vein endothelial cells were exposed to fluid flow in a parallel plate flow chamber in the presence of the inflammatory mediator histamine or the proteolytic enzyme thrombin. The initiation of shear stress (in the range of 0.2 to 20 dyn/cm^2) in the absence of either agonist caused no increase in intracellular Ca^{2+} levels. Cells exposed to either histamine (10^{-9} – 10^{-7} M) or thrombin (0.02 – 0.2 units/ml) showed an intracellular calcium increase (20 – 150 nM) that was dependent on the magnitude of the shear stress and on the concentration of agonist. In cells exposed to histamine and shear stress, the magnitude of the intracellular calcium increase was not altered, except at 10^{-7} M histamine. The time course of the response was significantly faster for arterial versus venous levels of shear stress at histamine concentrations from 10^{-9} M to 10^{-7} M. The magnitude of the $[\text{Ca}^{2+}]_i$ response was dependent on both the magnitude of the shear stress and the concentration of thrombin. At a thrombin concentration of 0.2 units/ml, the increase in intracellular Ca^{2+} was significantly greater at arterial levels of shear stress (6-20 dynes/cm^2) than at venous levels of shear stress (0.2-1 dyne/cm^2). The alterations in the $[\text{Ca}^{2+}]_i$ response were not due to differences in mass transfer characteristics since we solved the governing mass balance equation to precisely determine the effect of flow on local agonist concentration. These results demonstrate that even in a system where the initiation of shear stress without agonist causes no detectable change in intracellular Ca^{2+} , the calcium response to agonists is changed suggesting that the signal transduction pathway for shear stress acts synergistically with the thrombin and histamine signal transduction pathways.

Introduction

Endothelial cells line blood vessel walls and form the interface between the flowing blood and the smooth muscle tissue of the vessel wall. These cells are exposed to shear stress and a number of signaling molecules in the blood. Endothelial cells are a source of vasoactive compounds and are vital in regulating many physiological processes. Endothelial cells act as a transducing surface for shear stress effects on the vessel wall. These cells sense changes in blood flow and signal the smooth muscle cells to respond accordingly by synthesizing platelet-derived growth factor, interleukins, endothelins, nitric oxide, and prostacyclin. They also modulate the contractile state and proliferation of the underlying smooth muscle cells, interact with leukocytes, and participate in the reactions involved in blood clot formation and thrombolysis.² On a time scale of several days, there are shear stress induced morphological

changes of endothelial cell of such as elongation and alignment of the cells and their cytoskeletal structural elements with the direction of the flow.⁴

The signal transduction pathway for shear stress activation of endothelial cells is not clear. Some studies have suggested a role for the mitogen activated protein kinase cascade.¹⁵ Several studies^{1; 3; 6; 8-10; 13} have suggested that the initiation of shear stress can cause a transient increase in intracellular calcium concentration. But, several other studies^{5; 11; 12; 14; 17} have reported seeing no such increase in the absence of specific chemical agonists. Since many of the endothelial cell functions that are altered in response to shear stress appear to depend on elevations of intracellular calcium, it seems reasonable to hypothesize that shear stress itself would increase intracellular calcium levels.

To clarify the role of intracellular calcium increases in shear stress signal transduction, we will determine the time course of the change in intracellular calcium concentration in endothelial cells exposed to shear stress and either histamine or thrombin by using cells loaded with the calcium sensitive fluorescent dye, fura-2, and fluorescence video microscopy. Our hypothesis is that shear stress amplifies the intracellular calcium response of endothelial cells to low concentrations of agonists, although by itself, shear stress has no measurable effect intracellular calcium concentrations.

Materials and Methods

Cell Culture

Human umbilical vein endothelial cells (HUVEC) were isolated from umbilical cords obtained from the Norman Regional Hospital, Norman, OK. Briefly, the veins were washed with HEPES-buffered saline to remove excess blood, and then incubated for 45 minutes, with type I collagenase at room temperature. The resulting cell suspension was centrifuged at 700g for 10 min. The cells were resuspended in 15 ml of complete tissue culture medium containing M199, 1.0 % L-glutamine, 20% fetal bovine serum, and 2.5 % penicillin-streptomycin. The cells were seeded onto glass slides and incubated for five days until the monolayer had become confluent.

Fluorescent Dye Loading

Confluent monolayers of primary human umbilical vein endothelial cells (HUVECs) on coverslips were loaded with the calcium sensitive fluorescent dye, fura-2. Fura-2 AM was added to 10 ml tissue culture media M-199, which was placed on the cells at a final concentration of 5 μ M Fura2-AM. After 30 minutes at 37°C the slides were washed three times with HEPES buffered saline and incubated with M-199 for an additional 30 minutes at 37°C. Cells were used for experiments within 2 hours of loading the fluorescent dye.

Flow Experiments

The glass slide with the endothelial cell monolayer was mounted onto the flow chamber. The flow chamber was made of polycarbonate and designed to give a parallel flat plate flow geometry.¹² The flow rate through the flow chamber was varied between 0.13 and 13.3 cm³/min by an infusion/withdrawal syringe pump (producing shear stresses in the range of 0.2 to 20 dyn/cm²). The flow chamber was mounted on the stage of an inverted Nikon microscope with a 150W Xenon light source and the cells were imaged with a 40X fluorite objective. The cells were alternately illuminated with light at wavelengths of 340 nm and 380 nm. The emission, at 510 nm was detected with an intensified ccd camera and saved to the computer. Pairs of images were obtained approximately every second. A ratio of the two images was calculated using digital image analysis software developed by Inovision.

Data Analysis

The area of analysis was a 120 μ m by 130 μ m rectangle in the center of the field of view. The resting intracellular calcium concentration was defined as the average concentration in the ten seconds before the initiation of flow. The maximum intracellular calcium concentration was defined as the average concentration within ten seconds of the peak value. The difference between the maximum and resting intracellular calcium concentrations was defined as the increase in $[Ca^{2+}]_i$. The lag time for the intracellular calcium response was defined as the difference in time from when the agonist concentration near the cells had reached 50% of its bulk value until the cells had reached 50% of their maximum intracellular calcium response. The concentration of agonist near the surface of the endothelial cell monolayer does not instantaneously go from zero to the bulk concentration. Mass transfer limitations cause the agonist concentration to vary as a function of the flow rate, time, and position within the flow chamber. In these studies, the position was fixed at a point 1 cm from the inlet to the flow channel at the cell surface. At this point, the concentration of agonist near the wall will be only a function of time. We solved the time dependent convection diffusion equations using a finite difference technique to determine the time course of agonist concentration near the endothelial cell surface, rather than measure the change in agonist concentration directly.

The governing mass balance equation in differential form is given by:

$$\frac{\partial c}{\partial t} + v(y) \frac{\partial c}{\partial x} = D \frac{\partial^2 c}{\partial y^2}$$

where c is the concentration of agonist and is a function of time and position in the flow chamber. The velocity field in the flow chamber is assumed to be parabolic and is given by $v(y) = v_{max}(1 - (y/h)^2)$, where v_{max} is the velocity at the center of the flow channel and h is the half height of the flow channel. The binary diffusion coefficient is given by D and was assumed to be equal to 6.73×10^{-4} cm²/s for histamine¹⁶ and 4.16×10^{-7} cm²/s for thrombin⁷. The boundary conditions are no flux of agonist at the cell surface ($y=1$), no flux at the centerline ($y=0$), an agonist concentration of zero at the inlet ($x=0$), and $dc/dx = 0$ at $x=L$, far downstream from the inlet. The governing equation and its associated boundary conditions were solved using the finite difference technique. The region was divided into approximately 5,000 small elements such that the concentration and velocity within each small element could be considered constant. The sizes of the small elements were chosen to be small enough that the computed concentrations did not change if the elements were made smaller. A FORTRAN program implementing the Crank-Nichleson method was developed. The resulting set of linear equations was solved iteratively at each time step, with Δt equal to 0.0002s. The order of magnitude difference in the diffusion coefficient between thrombin and histamine suggests that the concentration profile for thrombin will develop more slowly. The model predicts that at 0.2 dynes/cm² it will take 13 seconds for histamine to reach 50% of its bulk value at a point on the wall at the middle of the flow chamber, while it will take thrombin about 25 seconds to reach 50% of its bulk value.

Results

Primary human umbilical vein endothelial cells exposed to the initiation of shear stress with HBSS ranging from 0.2 up to 20 dyn/cm² did not display a measurable increase in intracellular calcium levels. In contrast, cells exposed to shear stress in the presence of a

chemical agonist, either thrombin or histamine showed an increase in intracellular calcium levels. Figure 1 shows typical tracings for the central portion of a 40X field of view (approximately 60 – 80 cells) responding to the initiation of flow at 0.2, 1.0, or 20 dyn/cm² for several concentrations of histamine. Intracellular calcium levels begin to increase within several seconds after the flow has started. The calcium levels reached a peak value and then slowly return to near basal values over a period of several minutes. The response of individual cells was similar to the response of the field of view. The standard deviation for the maximum increase in [Ca²⁺]_i in individual cells was about 10%. The first vertical bar in each panel shows the time that flow was initiated. The second vertical bar shows the time at which the histamine concentration at the cell surface has reached 50% of the bulk value at a point midway between the inlet and outlet of the flow chamber. This value was obtained from the finite difference solution to the convection/ diffusion equation. This shows that endothelial cell intracellular calcium response to histamine is faster at higher levels of shear stress. The lag times are summarized in Table 1. The lag time for the intracellular calcium response was defined as the difference between when the cells had reached 50% of their peak intracellular calcium concentration and the time required for the concentration of agonist at the cell surface to reach 50% of its maximum value (the second vertical line in each of the panels in Figure 1). There is a significant decrease (p<0.05) in the lag time at each histamine concentration between cells exposed to 0.2 dynes/cm² and cells exposed to 20 dynes/cm². Also, increasing the histamine concentration from 10⁻⁹M to 10⁻⁷M caused a significant (p<0.05) decrease in the lag time at each shear stress.

Table 1. The Lag Time for Increases in [Ca²⁺]_i as a Function of Shear Stress and Histamine Concentration

	Delay time (sec.) for intracellular calcium concentrations to reach 50% of their maximum value.				
Concentration of Histamine	Shear stress 0.2 dyn/cm ²	Shear stress 1 dyn/cm ²	Shear stress 6 dyn/cm ²	Shear stress 12 dyn/cm ²	Shear stress 20 dyn/cm ²
10 ⁻⁹ M	46.8 ± 6.0	42.4 ± 1.1	21.0 ± 1.4	22.6 ± 4.7	11.8 ± 1.3
10 ⁻⁸ M	30.2 ± 13.0	19.6 ± 1.3	10.9 ± 0.5	9.5 ± 1.5	8.1 ± 0.3
10 ⁻⁷ M	9.7 ± 3.0	11.0 ± 2.9	6.2 ± 0.8	6.9 ± 1.2	5.1 ± 0.9

The maximum increase in intracellular calcium concentration for the central portion of a field of view (Figure 2A) was a function of the histamine concentration, but not a function of the shear stress except at the highest concentration of histamine used (10⁻⁷M). Cells exposed to 10⁻¹⁰ M histamine did not exhibit any increase in intracellular calcium levels and responded similarly to cells exposed to HBSS alone. In contrast, cells exposed to thrombin in the presence of shear stress displayed an intracellular calcium response that depended on both the concentration of thrombin and the magnitude of the shear stress (Figure 2B). At low levels of thrombin and low shear stress, the increase in intracellular calcium concentration was small, about 0.01 μM. At high concentrations of thrombin (up to 0.2 units/ml (U/ml)) and arterial levels of shear stress (up to 20 dyn/cm²), the increase in intracellular calcium concentration was much larger, about 0.10

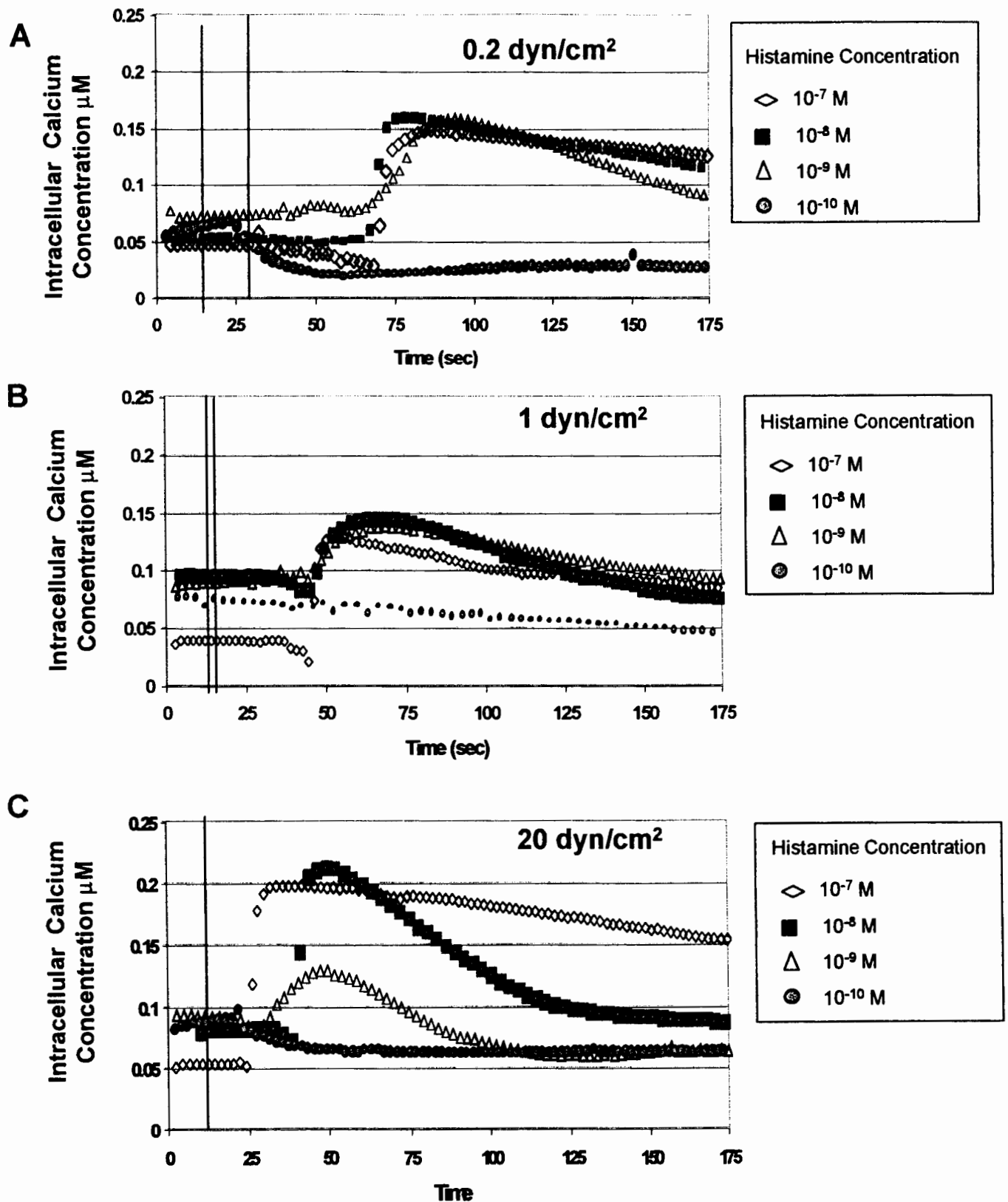
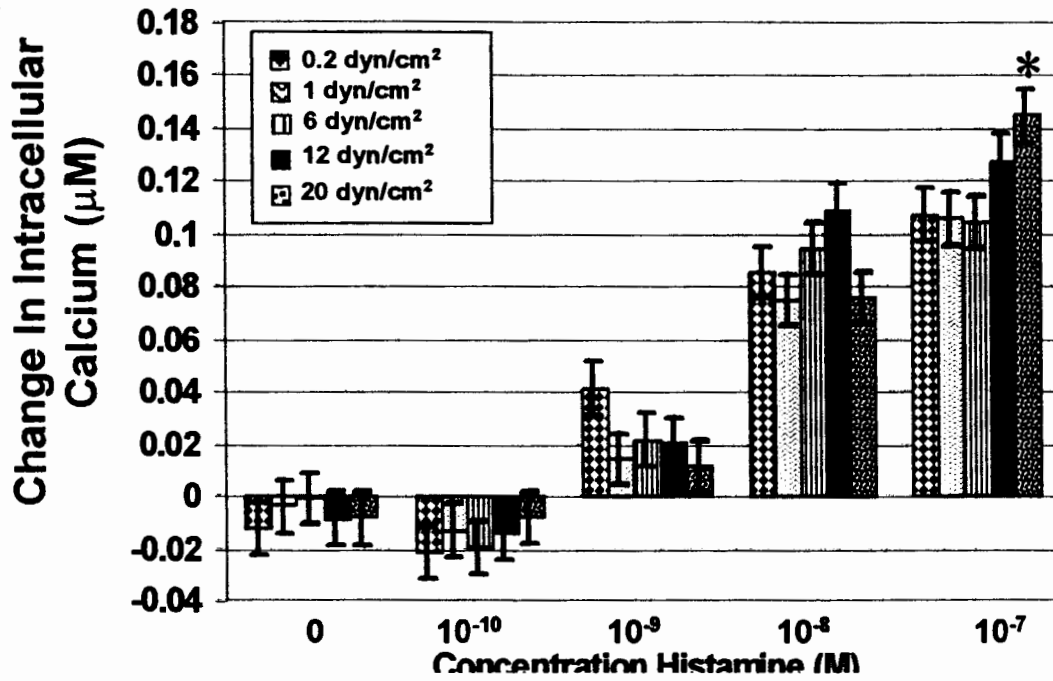
Figure 1

Figure 1: The intracellular calcium response of a single 40X field of view of HUVEC (about 80-100 cells) exposed to flow at several concentrations of histamine is shown. The calcium concentrations have been normalized so that 1.0 is the resting level. The first vertical bar on the graphs represents the time flow was started and the second bar represents the time at which the convection/diffusion model predicts that the histamine concentration at the wall reaches 50% of the bulk concentration. For 0.2 dynes/cm² the time to reach 50% of maximum is 13 seconds, for 1 dyne/cm² it is 3.4 seconds and for 20 dynes/cm² it is 0.4 seconds.

Figure 2

A



B

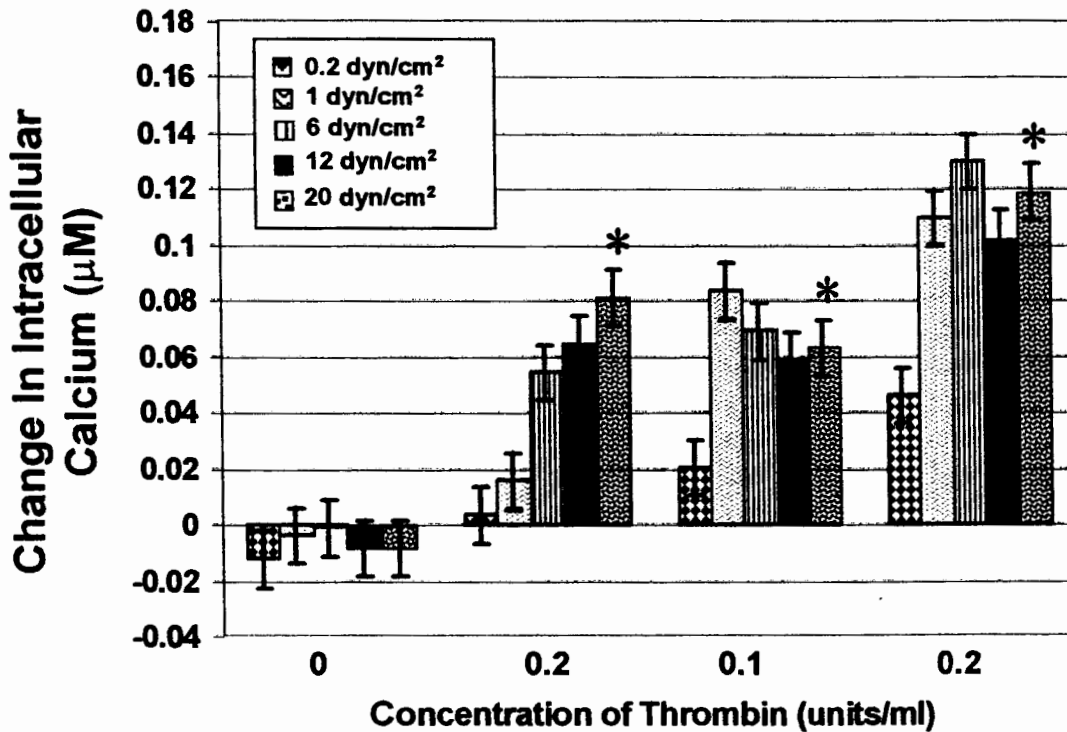


Figure 2: The maximum increase in intracellular calcium concentration for endothelial cells exposed to shear stress and either histamine or thrombin. Results from 6 to 8 different cord pools were averaged for each data point. The error bars represent the standard error of the mean. Figure 2A shows cells exposed to histamine. Figure 2B shows cells exposed to thrombin.

μM . The change in intracellular calcium concentration was significantly greater in cells exposed to 20 dynes/cm^2 than to cells exposed to 0.2 dynes/cm^2 at all thrombin concentrations examined.

Figure 3A-C shows the response of single cells exposed to thrombin over a range of shear stresses. This figure highlights our result that increasing the magnitude of the shear stress can increase the intracellular calcium response. Also evident in this figure is that there is a delay in the response of cells to the initiation of the flow in the presence of agonist, particularly at the lower levels of shear stress. The time course of the response of individual cells to thrombin was quite heterogeneous, but there was not much variation in the maximum intracellular calcium concentration. The standard deviation of the response of single cells was about 10% of the change in intracellular calcium concentration. This heterogeneity in response is illustrated in Figure 4 where we show the percentage of cells in the field of view that have begun to respond as a function of time for cells exposed thrombin over a range of shear stresses. A cell is deemed to have responded when its intracellular calcium concentration has increased by at least 20 nM. We find that for all but the lowest shear stress used (0.2 dyn/cm^2) essentially all of the cells in the field of view will eventually respond. The time required for the cells to respond increases as the shear stress is decreased. In some cases, individual cells exposed to thrombin and shear responded before the model predicts that the concentration reaches 50% of the bulk value. These cells are responding to the thrombin concentration as it builds up to the bulk value. Interestingly, the time course of the response of single cells exposed to histamine and flow was much more homogeneous. All of the cells in a field of view responded within two seconds regardless of the magnitude of the shear stress for histamine concentrations greater than or equal to 10^{-9}M (data not shown).

Discussion

The initiation of shear stress has been shown to cause increased synthesis of prostacyclin, NO, release of von Willebrand Factor, and morphological changes. These events have been associated with an increase in intracellular calcium levels. Although several studies have demonstrated an increase in $[\text{Ca}^{2+}]_i$ in response to the initiation of shear stress, there have also been several that fail to demonstrate any increase. In this study, we showed that although shear stress by itself causes no measurable change in intracellular calcium levels, the magnitude of the shear stress does change the response of endothelial cells to histamine and thrombin stimulation. This change in the intracellular calcium response is manifested in two distinct ways, a change in the time course of the response, or a change in the magnitude of the intracellular calcium response.

First, for both histamine and thrombin stimulated cells, there is a lag time after the cells are exposed to the agonist before the intracellular calcium concentration begins to increase. The duration of the lag time depends on mass transfer limitations as well as on intracellular processes. To determine the contribution of intracellular processes on the duration of the lag time we solved the governing differential equation for the concentration of agonist (either histamine or thrombin) in the flow chamber as a function of position and time. The results clearly show that the duration of the lag time decreases as the shear stress is increased at any concentration of histamine used (see Table 1). Secondly, for thrombin, but not histamine stimulated cells, the magnitude of the maximum increase in the intracellular calcium concentration depends on the magnitude of the shear stress. These two findings suggest that the signal transduction pathway for shear stress stimulated endothelial cells involves modulations in intracellular calcium signaling.

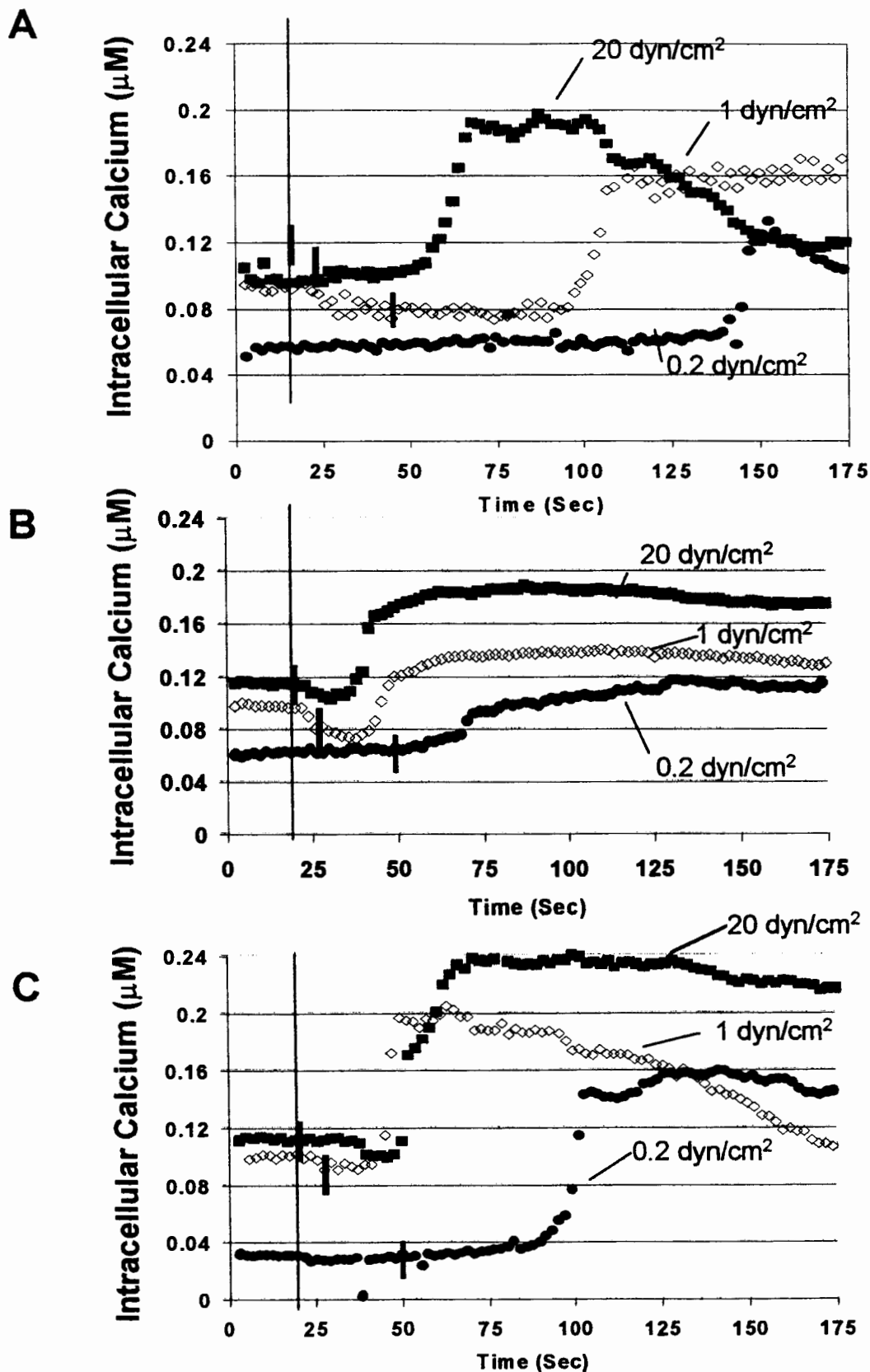


Figure 3: The response of single cells in a monolayer of primary human endothelial cells that was exposed to thrombin and shear stress rates of either 0.2, 1.0, or 20 dynes/cm². The black vertical bar at about 20 seconds indicates the time flow was started. The small vertical bars on each single cell tracing illustrate the time required for the concentration of thrombin near the cell surface to reach 50% of its bulk value as determined by the solution to the convection/diffusion equations. This time is 25.3 seconds for 0.2 dynes/cm², 7.7 seconds for 1 dyne/cm² and 0.6 seconds for 20 dynes/cm². Figure 3A shows the response to 0.02 U/ml of thrombin. Figure 3B shows 0.1 U/ml of thrombin. Figure 3C shows 0.2 U/ml of thrombin.

Figure 4

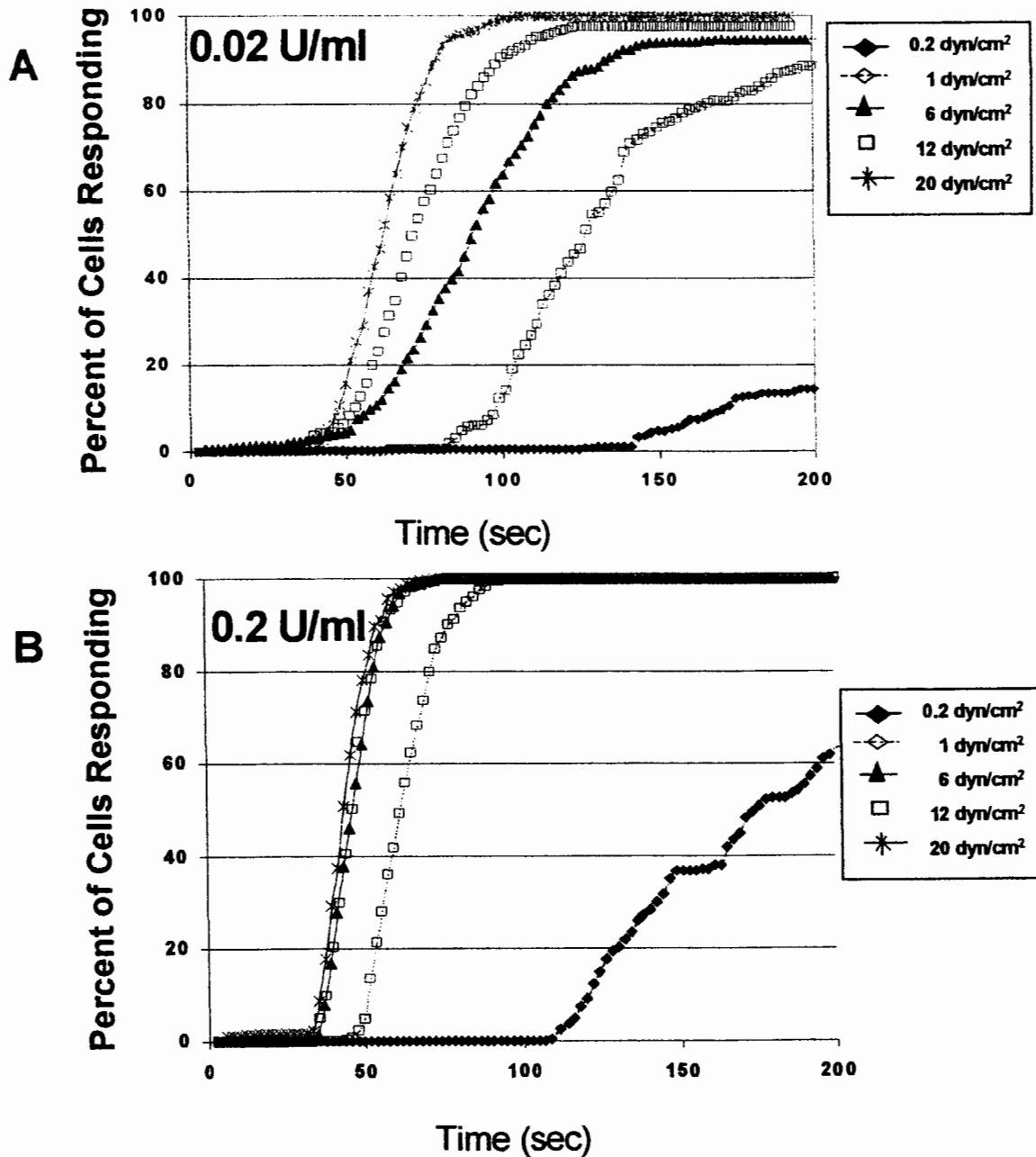


Figure 4: Confluent monolayers of endothelial cells were exposed to shear stress and thrombin. The percent of cells that showed an increase of at least 20nM in intracellular calcium was determined for each field of view. There were 2 to 5 experiments used for each shear stress and concentration of thrombin. Figure 4A is for 0.02 U/ml thrombin and B is for 0.2 U/ml thrombin.

There are two important differences in the way endothelial cells respond to either histamine or thrombin. First, histamine is a small molecule and consequently it diffuses quickly relative to the large protein thrombin. Therefore, the histamine concentration near the cell surface in the flow chamber increases more rapidly than the thrombin concentration. For example, as illustrated in Figures 1 and 3, at 1 dyn/cm² it takes histamine about 3.4 seconds to reach 50% of its bulk value while it takes thrombin about 7.7 seconds. Secondly, the thrombin receptor is proteolytically cleaved by thrombin in order to be activated. Consequently, cells that are exposed to thrombin will lose thrombin receptor from their surface. These two phenomena suggest that at low shear stresses the cell monolayer is exposed to a slowly increasing concentration of thrombin. This helps to explain the results presented in Figure 2 where the maximum increase in intracellular calcium concentrations is reduced at lower shear stress. At the low shear rates, the cells are in effect being exposed to a low thrombin concentration for some period of time before they are exposed to the bulk thrombin concentration. This can result in a desensitization of the cells to thrombin due to cleavage of the thrombin receptor on the cell surface. This may also explain why the response of cells to thrombin is so much more heterogeneous than the response to histamine.

What is clear from our study is that shear stress can directly alter calcium signaling in histamine or thrombin stimulated endothelial cells. The cells can thereby determine information about the shear stress environment.

References

- 1) Ando, J., Ohtsuka, A., Katayama, Y., Korenaga, R., Ishikawa, C. and Kamiya, A. Intracellular calcium response to directly applied mechanical shearing force in cultured vascular endothelial cells. *Biorheology* **31**, 57-68, 1994.
- 2) Cines, D. B., Pollak, E. S., Buck, C. A., Loscalzo, J., Zimmerman, G. A., McEver, R. P., Poer, J. S., Wick, T. M., Konkle, B. A., Schwartz, B. S., Barnathan, E. S., McCrae, K. R., Hug, B. A., Schmidt, A. M. and Stern, D. M. Endothelial cells in physiology and in the pathophysiology of vascular disorders. *Blood* **91**, 3527-61, 1998.
- 3) Corson, M. A., James, N. L., Latta, S. E., Nerem, R. M., Berk, B. C. and Harrison, D. G. Phosphorylation of endothelial nitric oxide synthase in response to fluid shear stress. *Circ Res* **79**, 984-91, 1996.
- 4) Davies, P. Overview: Temporal and Spatial Relationships in Shear Stress-Mediated Endothelial Signaling. *Journal Vascular Research* **34**, 208-211, 1997.
- 5) Dull, R. O. and Davies, P. F. Flow modulation of agonist (ATP)-response (Ca²⁺) coupling in vascular endothelial cells. *Am J Physiol* **261**, H149-54, 1991.
- 6) Fleming, I., Bauersachs, J. and Busse, R. Calcium-dependent and calcium-independent activation of the endothelial NO synthase. *J Vasc Res* **34**, 165-74, 1997.
- 7) Folie, B. J. and McIntire, L. V. Mathematical analysis of mural thrombogenesis. Concentration profiles of platelet-activating agents and effects of viscous shear flow. *Biophys J* **56**, 1121-41, 1989.
- 8) Geiger, R. V., Berk, B. C., Alexander, R. W. and Nerem, R. M. Flow-induced calcium transients in single endothelial cells: spatial and temporal analysis. *Am J Physiol* **262**, C1411-7, 1992.
- 9) Helmlinger, G., Berk, B. C. and Nerem, R. M. Pulsatile and steady flow-induced calcium oscillations in single cultured endothelial cells. *J Vasc Res* **33**, 360-9, 1996.

- 10) James, N. L., Harrison, D. G. and Nerem, R. M. Effects of shear on endothelial cell calcium in the presence and absence of ATP. *Faseb J* **9**, 968-73, 1995.
- 11) Mo, M., Eskin, S. and Schilling, W. Flow-Induced Changes in Ca²⁺ Signaling of Vascular Endothelial Cells: Effect of Shear Stress and ATP. *American Journal of Physiology* **260**, H1698-H1707, 1991.
- 12) Nollert, M. U. and McIntire, L. V. Convective mass transfer effects on the intracellular calcium response of endothelial cells [published erratum appears in *J Biomech Eng* 1992 Nov;114(4):496]. *J Biomech Eng* **114**, 321-6, 1992.
- 13) Rosales, O. R., Isales, C. M., Barrett, P. Q., Brophy, C. and Sumpio, B. E. Exposure of endothelial cells to cyclic strain induces elevations of cytosolic Ca²⁺ concentration through mobilization of intracellular and extracellular pools. *Biochem J* **326**, 385-92, 1997.
- 14) Shen, J., Lusinskas, F., Connolly, A., Dewey, C. F. J. and Gimbrone, M. J. Fluid Shear Stress Modulates Cytosolic Free Calcium in Vascular Endothelial Cells. *American Journal of Physiology* **262**, C384-C390, 1992.
- 15) Tseng, H., Peterson, T. E. and Berk, B. C. Fluid shear stress stimulates mitogen-activated protein kinase in endothelial cells. *Circ Res* **77**, 869-78, 1995.
- 16) Weast, R. (1976) Handbook of Chemistry and Physics. In *CRC*, pp. F-62, CRC Press, Cleveland, OH.
- 17) Yoshikawa, N., Ariyoshi, H., Ikeda, M., Sakon, M., Kawasaki, T. and Monden, M. Shear-stress causes polarized change in cytoplasmic calcium concentration in human umbilical vein endothelial cells (HUVECs). *Cell Calcium* **22**, 189-94, 1997.